

LARGE SCALE BROADBAND ANTENNA ARRAY SYSTEMS

A thesis submitted to The University of Manchester for the degree
of Doctorate of Philosophy
in the Faculty of Engineering and Physical Sciences

2011

AHMED EL-MAKADEMA

School of Electrical and Electronic Engineering
Microwave and Communication Systems Research Group

TABLE OF CONTENTS

Acknowledgement	6
List of Abbreviations	8
List of Notations	11
List of Figures	12
Abstract	20

Chapter 1: Introduction

1.1	Motivation	23
1.2	Overview	25
	1.2.1 Array Geometry	29
	1.2.2 Broadband Antenna Element	33
	1.2.3 Mutual Coupling	34
	1.2.4 Beamforming	37
1.3	Contribution	38
1.4	Chapter Summary	39

Chapter 2: Approach

2.1	Introduction	41
2.2	Geometry Optimization	42
2.3	Broadband Antenna Element Design	47
2.4	Mutual Coupling Consideration	52
2.5	Experimental Model	55
2.6	Application	55
2.7	Chapter Summary	56

Chapter 3: Periodic Arrays

3.1	Introduction	57
3.2	Square and Triangular Arrays	57
3.3	Concentric Rings Arrays	66
3.4	Chapter Summary	75

Chapter 4: Aperiodic Arrays

4.1	Introduction	77
4.2	Random Arrays	77
	4.2.1 Minimum separation constraint	
	Random Arrays	77
	4.2.2 Tapered Random Arrays	86
4.3	Spiral Arrays	89
	4.3.1 Exponential Taper	90
	4.3.2 Power Density Taper	99
4.4	Other Arrays	105
4.5	Chapter Summary	109

Chapter 5: Scalability and Mutual Coupling

5.1	Introduction	110
5.2	Scaled Models	111
5.3	Full Wave Scalability	114
5.4	Full wave geometry comparison	118
5.5	Chapter Summary	122

Chapter 6: Beamforming

6.1	Introduction	123
6.2	Mutual Coupling Compensation	124
6.3	Scanning	133
6.4	Amplitude Tapering	138
6.5	Chapter Summary	142

Chapter 7: Experimental Model

7.1	Introduction	143
7.2	Element Design	144
7.3	Array Design	146
7.4	Model Construction	148
7.5	Measurements	151
7.6	Chapter Summary	155

Chapter 8: On Large Scale Broadband Array Optimization

8.1	Introduction	156
8.2	Square Kilometre Array low frequency aperture array SKA-AAlow	157
8.3	Antenna Array noise temperature	159
8.4	Chapter Summary	162

Chapter 9: Conclusion and Future work

9.1	Conclusion	163
9.2	Future Work	166
PUBLICATIONS		168
REFERENCES		169
BIBLIOGRAPY		179

Acknowledgements

I would like to express my sincere gratitude and appreciation to my supervisor Professor A.K Brown. Without his invaluable guidance and support this thesis would not have been accomplished.

I am very grateful to my advisor Dr R. Sloan for his kind help throughout the course of the PhD. I would also like to thank Mr. Keith Williams for his help in the measurement of the experimental model, in addition to his help with computational resources.

I owe special thanks to Dr. Georgina Harris and Mr. Tim Ikin for their help and advice with the mechanical design of the experimental model.

I am immensely grateful to my parents whose support, encouragement and guidance were always present despite the long distance.

I am also grateful to all my colleagues at the school of Electrical Engineering and Electronics. I would also like to particularly thank my colleagues Dr Chris Masouros, Dr David Zhang, Dr Laith Rashid and Dr Ming Yang.

I have had the fortune to be part of the SKA project working with highly skilled people from a wide range of disciplines. This has greatly increased my knowledge and experience and I am very thankful to everyone on the SKA teams.

I would like to express my thanks to Dr Nima Ghods and Dr Eloy De Lera from the Cavendish laboratory at the University of Cambridge for their contribution to this work, particularly to their help with the antenna array temperature calculations in chapter 8.

I would also like to greatly acknowledge the funding and support of the Science and Technology Facilities Council (STFC) in undertaking this work as part of the UK Square Kilometre Array Design Study (SKADS) project.

List of Abbreviations

AA: Aperture Array

AT: Amplitude Taper

CEM: Computational Electro-Magnetics

CST: Computer Simulation Technology

E plane: Plane containing the electric field vector

FEM: Finite Element Method

FIT: Finite Integration Technique

GA: Genetic Algorithms

HFSS: High Frequency Structure Simulator

H plane: Plane containing the magnetic field vector

LCMV: Linear Constraints Mean Variance

LNA: Low Noise Amplifier

MoM: Method of Moments

MS: Mean Square

MSL: Mean Side Lobe

NS: Null Steering

PSL: Peak Side Lobe

PTFE: polytetrafluoroethylene

SKA: Square Kilometre Array

SMA: SubMiniature version A

List of Notations

A : Antenna Element Radiation Pattern

A_{eff} : Array Effective Area

D : Directivity

D_{max} : Maximum Achievable Array Directivity

D_{ap} : Aperture Array Diameter

d : Antenna Element Separation

d_{min} : Minimum Element Separation

d_{max} : Maximum Element Separation

d_{av} : Average Separation

e : Base of Natural Logarithm

exp : Exponential

F : Array Factor

f : Frequency

f_{max} : Frequency of Maximum Directivity

f_L : Lowest Frequency

f_H : Highest Frequency

G : Array Gain

\bar{I} : Matrix of N Currents

j : Imaginary Unit

k : Wave Number

$\bar{\bar{M}}$: Mutual Coupling Matrix

N_r : Number of Rings

N : Total Number of Antenna Elements in an array

n : Antenna Element Index

r_n : Radial Displacement of the n^{th} antenna element in polar Coordinates

S : Sensitivity

T_A : Antenna Noise Temperature

T_{amb} : Ambient Temperature

T_{LNA} : Low Noise Amplifier Temperature

T_{sky} : Sky Brightness Temperature

T_{sys} : System Noise Temperature

V_{in} : Input Voltage

\bar{V} : Matrix of Voltages

W : Amplitude Weights

x_n : X Axis Coordinate of n^{th} antenna element

y_n : Y Axis Coordinate of n^{th} antenna element

Z_s : Internal Impedance

Z : Input Impedance

Z_m : Mutual Impedance

η_{total} : Total Efficiency

η_{rad} : Radiation Efficiency

η_{rad} : Radiation Efficiency

η_{loss} : Mismatch loss

θ : Elevation Angle

ϕ : Azimuth Angle

θ_{scan} : Elevation Angle Scan

ϕ_{scan} : Azimuth Angle Scan

φ_n : Angular Displacement of n^{th} Antenna Element

λ : Wavelength

λ_{max} : Wavelength at Maximum Achievable Directivity

λ_H : Wavelength at Highest Frequency

λ_L : Wavelength at Lowest Frequency

Φ : Golden Number

List of Figures

Figure 1.1: Relative sensitivity for different existing radio telescopes [1]	23
Figure 1.2: Artist impression of an SKA station [1]	24
Figure 1.3 Linear uniform array	28
Figure 1.4 Radiation pattern of 16 element half wavelength separated linear array	29
Figure 1.5 Radiation pattern of 16 element separated by a distance of 1.5 wavelength	29
Figure 1.6 Radiation pattern of 16 element array with main beam scanning	30
Figure 1.7: Typical receive antenna array system architecture	31
Figure 1.8: Sensitivity vs. Total Efficiency for different antenna noise temperatures	33
Figure 2.1: Array coordinate systems	47
Figure 2.2: Fork tapered slot broadband antenna	55
Figure 2.3: Fork tapered slot antenna return loss	55
Figure 2.4: Isolated fork tapered slot antenna E plane radiation pattern	56
Figure 2.5: Isolated fork tapered slot antenna H plane radiation pattern	57
Figure 3.1: (a) Square Array, (b) Tapered Square Array, (c) Triangular Array, (d) Tapered Triangular Array.	64
Figure 3.2: Directivity performance for periodic and tapered periodic arrays.	66
Figure 3.3: Peak side lobe performance for periodic and tapered periodic arrays.	67

Figure 3.4: Mean side lobe performance for periodic and tapered periodic arrays.	68
Figure 3.5: Radiation patterns at frequencies of maximum achievable directivity for (a) Square, (b) Tapered Square, (c) Triangular and (d) Tapered Triangular arrays	70
Figure 3.6: Radiation pattern at highest frequency for (a) Square, (b) Tapered Square, (c) Triangular and (d) Tapered Triangular arrays	71
Figure 3.7: (a) Uniform Concentric Rings, (b) Tapered Concentric Rings, (c) Randomized Concentric Rings array.	74
Figure 3.8: Directivity performance for uniform, randomized and tapered concentric rings array.	75
Figure 3.9: Peak side lobe performance for uniform, randomized and tapered concentric rings array.	76
Figure 3.10: Mean side lobe performance for uniform, randomized and tapered concentric rings array.	77
Figure 3.11: Radiation patterns at frequencies of maximum achievable directivity for (a) Uniform, (b) Randomized, and (c) Tapered Concentric Rings arrays	78
Figure 3.12: Radiation Pattern at the highest frequency for (a) Uniform, (b) Randomized, and (c) Tapered Concentric Rings arrays	80
Figure 4.1: Random arrays with different minimum separation (a) $d_{min} = 0.3\lambda_H$, (b) $d_{min} = 0.8\lambda_H$, (c) $d_{min} = 1.7\lambda_H$, (d) $d_{min} = 2.3\lambda_H$	84
Figure 4.2: Directivity performances for random arrays with different minimum separations.	85
Figure 4.3: Peak side lobe performance for random arrays with different	86

minimum separations.	
Figure 4.4: Mean side lobe performance for random arrays with different minimum separations.	87
Figure 4.5: Radiation patterns at frequencies of maximum achievable directivity random arrays, (a) $d_{min} = 0.3\lambda_H$, (b) $d_{min} = 0.8\lambda_H$, (c) $d_{min} = 1.7\lambda_H$, (d) $d_{min} =$	89
Figure 4.6: Radiation Patterns at the highest frequency for random arrays, (a) $d_{min} = 0.3\lambda_H$, (b) $d_{min} = 0.8\lambda_H$, (c) $d_{min} = 1.7\lambda_H$, (d) $d_{min} = 2.3\lambda_H$	91
Figure: 4.7 Tapered random array	92
Figure 4.8: Directivity performance of tapered and un-tapered random arrays	93
Figure 4.9: Peak side lobe performance of tapered and un-tapered random arrays	94
Figure 4.10: Mean side lobe performance of tapered and un-tapered random arrays	94
Figure 4.11: Radiation patterns of tapered random array (a) Frequency of maximum achievable directivity (b) Highest frequency	95
Figure 4.12: Exponential tapered golden ratio spiral (a) $exp = 1$, (b) $exp = 0.7$, (c) $exp = \Phi^{-1} = 0.6180$, (d) $exp = 0.5$	97
Figure 4.13: Directivity performance for exponential tapered golden angle spiral arrays	98
Figure 4.14: Peak sidelobe performance for exponential tapered golden angle spiral arrays	99
Figure 4.15: Mean sidelobe performance for exponential tapered golden angle spiral arrays	100
Figure 4.16: Radiation patterns of exponential tapered golden ratio spiral	102

arrays at frequencies of the maximum achievable directivity (a) $exp = 1$, (b) $exp = 0.7$, (c) $exp = \Phi^{-1} = 0.6180$, (d) $exp = 0.5$	
Figure 4.17: Radiation patterns of exponential tapered golden ratio spiral arrays at the highest frequency (a) $exp = 1$, (b) $exp = 0.7$, (c) $exp = \Phi^{-1} = 0.6180$, (d) $exp = 0.5$	104
Figure 4.18: Power density tapered arrays (a) Gaussian, (b) Dolph Chebyshev	106
Figure 4.19 Directivity performance for power density tapered golden angle spiral arrays	107
Figure 4.20 Peak side lobe performance for power density tapered golden angle spiral arrays	108
Figure 4.21 Mean sidelobe performance for power density tapered golden angle spiral arrays	108
Figure 4.22 Radiation patterns of power density tapered golden ratio spiral arrays at frequencies of the maximum achievable directivity for (a) Gaussian taper (b) Chebyshev taper	109
Figure 4.23 Radiation patterns of power density tapered golden ratio spiral arrays at frequencies highest frequency (a) Gaussian taper (b) Chebyshev taper	110
Figure: 4.24 Perturbed Danzer arrays [24]	112
Figure 4.25: Directivity performance for Perturbed Danzer arrays	113
Figure 4.26: Peak side lobe performance for Perturbed Danzer Arrays	114
Figure 4.27: Mean side lobe performance for Perturbed Danzer Arrays	114
Figure 4.28: Directivity performance for periodic and aperiodic arrays	115

Figure 4.29: Peak side lobe performance for periodic and aperiodic arrays	116
Figure 4.30: Mean side lobe performance for periodic and aperiodic arrays	116
Figure 5.1: Directivity performance for scaled random and spiral arrays.	119
Figure 5.2: Mean side lobe performance for scaled random and spiral arrays	120
Figure 5.3: Peak side lobe performance for scaled random and spiral arrays.	121
Figure 5.4 Scaled arrays for full wave Simulation performance for tapered spiral arrays, (a) 32 elements (b) 64 elements.	122
Figure 5.5: Directivity performance for scaled tapered spiral arrays.	123
Figure 5.6: Mean side lobe performance for scaled Tapered spiral arrays.	124
Figure 5.7: Mean side lobe performance for scaled Tapered spiral arrays.	124
Figure 5.8: Total Efficiency for Isolated element, Tapered Spiral and scaled Tapered spiral arrays.	125
Figure 5.9: Scaled arrays for full wave simulation performance for: (a) 32 elements Tapered Spiral Array (b) 32 elements Random Array.	127
Figure 5.10: Directivity performance for scaled tapered spiral and random arrays	127
Figure 5.11: Peak side lobe performance for scaled Tapered spiral and Random arrays	128
Figure 5.12: Mean side lobe performance for scaled Tapered spiral and Random arrays	128
Figure 5.13: Total Efficiency for Isolated element, Tapered spiral and Random arrays.	129
Figure 6.1: Radiation patterns for ideal, uncompensated and compensated tapered spiral at 300 MHz (a) E plane, (b) H plane	134

Figure 6.2: Radiation patterns for ideal, uncompensated and compensated tapered spiral at 400 MHz (a) E plane, (b) H plane	134
Figure 6.3: Radiation patterns for ideal, uncompensated and compensated tapered spiral at 500 MHz (a) E plane, (b) H plane	135
Figure 6.4: Radiation patterns for ideal, uncompensated and compensated random array at 300 MHz (a) E plane, (b) H plane	135
Figure 6.5: Radiation patterns for ideal, uncompensated and compensated random array at 400 MHz (a) E plane, (b) H plane	136
Figure 6.6: Radiation patterns for ideal, uncompensated and compensated random array at 500 MHz (a) E plane, (b) H plane	136
Figure 6.7: Antenna element 300 MHz surface current for different mutual coupling environments (a) high coupling, (b) low coupling, (c) no coupling	138
Figure 6.8: Antenna element 500 MHz surface current for different mutual coupling environments (a) high coupling, (b) low coupling, (c) no coupling	139
Figure 6.9: Antenna element 900 MHz surface current for different mutual coupling environments (a) high coupling, (b) low coupling, (c) no coupling	140
Figure 6.10: Directivity performance for random and spiral arrays with 30 degrees scan angle (1000 hemispheric elements)	143
Figure 6.11: Peak side lobe performance for random and spiral arrays with 30 degrees scan angle (1000 hemispheric elements)	143
Figure 6.12: Mean side lobe performance for random and spiral arrays with 30 degrees scan angle (1000 hemispheric elements)	144
Figure 6.13: Directivity performance for random and spiral arrays with 30 degrees scan angle (full wave simulation)	145
Figure 6.14: Peak side lobe performance for random and spiral arrays with	145

30 degrees scan angle (full wave simulation)	
Figure 6.15: Mean side lobe performance for random and spiral arrays with 30 degrees scan angle (full wave simulation)	146
Figure 6.18: Directivity performance for scaled random and spiral arrays with amplitude taper	147
Figure 6.19: Mean side lobe performance for scaled random and spiral arrays with amplitude taper	148
Figure 6.20: Mean side lobe performance for scaled random and spiral arrays with amplitude taper	148
Figure 6.21: Total Efficiency for random array with uniform and tapered weights	149
Figure 6.22: Total Efficiency for tapered spiral array with uniform and tapered weights	149
Figure 7.1: Printed dipole with integrated balun	153
Figure 7.2: Simulated dipole element return loss	154
Figure 7.3: Array geometry	155
Figure 7.4: Simulated return loss for 32 element golden angle array, CST	156
Figure 7.5: Dipole element mechanical structure	157
Figure 7.6: Elements on ground plane	157
Figure 7.7: Array mechanical support structure	158
Figure 7.8: Simulated Vs measured return loss	159
Figure 7.9: Simulated Vs measured H plane element Co-polar radiation pattern	160
Figure 7.10: Simulated Vs measured E plane element Co-polar radiation	160

pattern

Figure 7.11: connected array in the anechoic chamber 161

Figure 7.12: Simulated Vs measured H plane array Co-polar radiation 162

patterns

Figure 7.13: Simulated Vs measured array E Plane Co-polar radiation 163

patterns

Figure 8.1: Brightness temperature profile for different scan angles [3] 165

Figure 8.2: Overall SKA sensitivity for 250 stations of tapered spiral and 167
random array configurations, showing the number of elements per station

Figure 8.3 sky brightness at 408 MHz [58] 169

Figure 8.4 Antenna Array Temperature for Tapered Spiral and Random 169
arrays for 24 hour observation at 408 MHz.

Abstract

Broadband antenna arrays have become increasingly popular for various imaging applications, such as radio telescopes and radar, where high sensitivity and resolution are required. High sensitivity requires the development of large scale broadband arrays capable of imaging distant sources at many different wavelengths, in addition to overcoming noise and jamming signals. The design of large scale broadband antenna arrays requires large number antennas, increasing the cost and complexity of the overall system. Moreover, noise sources often vary, depending on their wavelengths and angular locations. This increases the overall design complexity particularly for broadband applications where the performance depends not only on the required bandwidth, but also on the frequency band.

This thesis provides a study of broadband antenna array systems for large scale applications. The study investigates different tradeoffs associated with designing such systems and drives a novel design approach to optimize both their cost and performance for a wide range of applications. In addition, the thesis includes measurements of a suitable array to validate the computational predictions. Moreover, the thesis also demonstrates how this study can be utilized to optimize a broadband antenna array system suitable for a low frequency radio telescope.

DECLARATION

No portion of the work referred to in the thesis has been submitted in support of an application for another degree or qualification of this or any other university or other institute of learning;

Copyright Statement

I. The author of this thesis (including any appendices and/or schedules to this thesis) owns certain copyright or related rights in it (the “Copyright”) and s/he has given The University of Manchester certain rights to use such Copyright, including for administrative purposes.

II. Copies of this thesis, either in full or in extracts and whether in hard or electronic copy, may be made **only** in accordance with the Copyright, Designs and Patents Act 1988 (as amended) and regulations issued under it or, where appropriate, in accordance with licensing agreements which the University has from time to time. This page must form part of any such copies made.

III. The ownership of certain Copyright, patents, designs, trademarks and other intellectual property (the “Intellectual Property”) and any reproductions of copyright works in the thesis, for example graphs and tables (“Reproductions”), which may be described in this thesis, may not be owned by the author and may be owned by third parties. Such Intellectual Property and Reproductions cannot and must not be made available for use without the prior written permission of the owner(s) of the relevant Intellectual Property and/or Reproductions.

IV. Further information on the conditions under which disclosure, publication and commercialisation of this thesis, the Copyright and any Intellectual Property and/or Reproductions described in it may take place is available in the University IP Policy (see <http://www.campus.manchester.ac.uk/medialibrary/policies/intellectual-property.pdf>), in any relevant Thesis restriction declarations deposited in the University Library, The University Library’s regulations (see <http://www.manchester.ac.uk/library/aboutus/regulations>) and in The University’s policy on presentation of Thesis.

Chapter1: Introduction

1.1 Motivation

In this thesis large scale broadband antenna arrays refer to arrays of thousands of antennas operating over a bandwidth of several octaves. The main reason for building such arrays is their ability to provide a highly sensitive multiband instrument. Such large arrays have been difficult to achieve in the past due to their high cost and large processing required for their operation. However, the recent advance in computing power facilitates the achievement of such large radio systems.

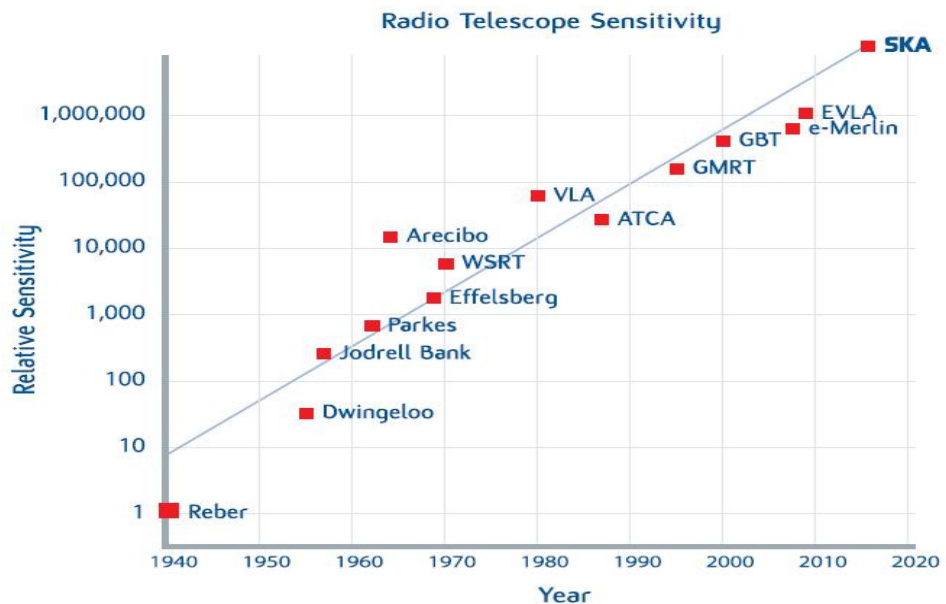


Figure 1.1: Relative sensitivity for different existing radio telescopes [1]

One major application is a radio telescope, where high sensitivity is required in order to image distant sources at many different wavelengths. Many radio telescopes have been built over the last few decades, revolutionizing astronomy and changing our understanding of the universe. However, the increasing demand for sensitivity requires developing the next generation of radio telescopes, such as the Square Kilometre Array (SKA), which will have a million square meters of collecting area, making it at least 50 times more sensitive, and able to survey the sky 10,000 times faster than any imaging radio telescope array ever built [1]. With such an instrument scientists believe they will be able to make many new discoveries as well as solving many mysteries in science and verifying existing theories. Figure 1.1 shows the evolution of radio telescopes over the past eight decades.

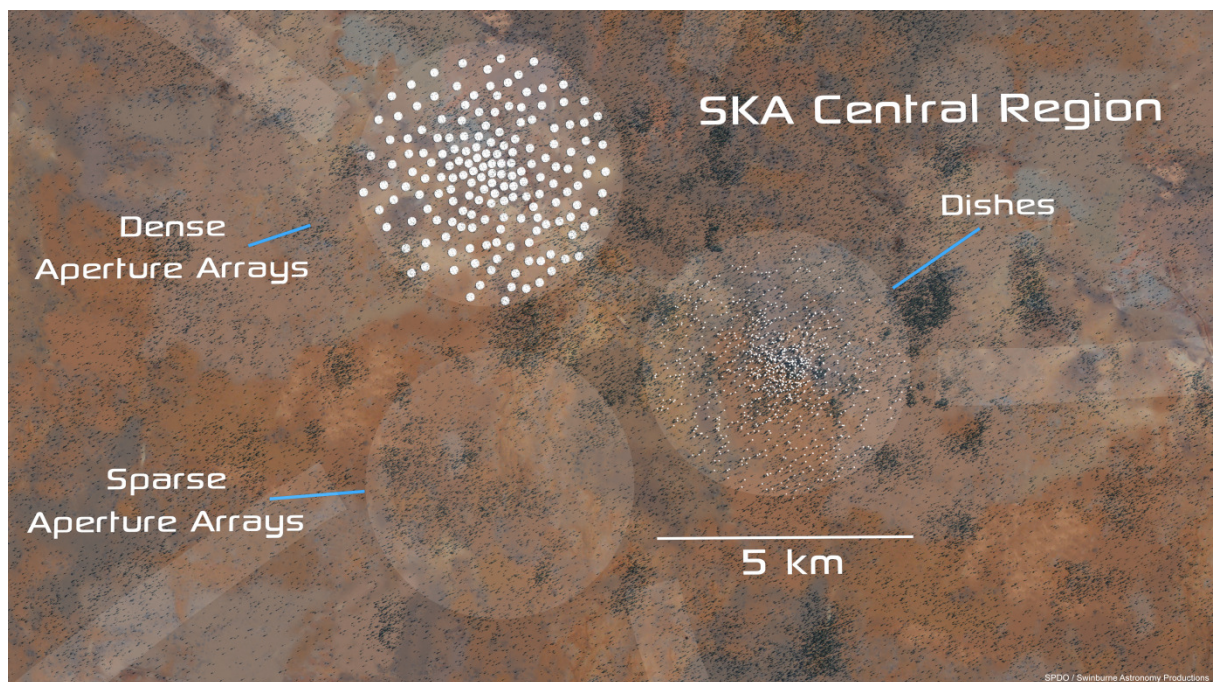


Figure 1.2: Artist impression of an SKA station [1]

Figure 1.2 shows an artist impression of a typical SKA station consisting of low frequency sparse aperture array, a middle frequency dense aperture array and a high frequency array of dishes.

Other applications of large scale broadband arrays include high sensitivity high resolution multiband military radars. Such systems are required for long range detection and to overcome enemy jamming signals.

Due to their recent demands, such large broadband antenna array systems have not been widely considered. This requires the development of computational models capable of modelling such large structure in order to predict and improve both the cost and the performance of the system.

1.2 Overview

An antenna can be defined as a transducer between and electromagnetic waves radiated through space and electromagnetic waves contained by a transmission line [Hansen]. An antenna array consists of more than one antenna, often called element, where the signals received/ transmitted by each antenna element are combined to form a single output. Each antenna element can be weighted prior to combination and hence control the overall radiation performance. If active components are used to apply the weights, then the antenna performance can be controlled electronically. This scheme has been shown to offer an enhancement in performance and flexibility over a single antenna [haupt]. The development of antenna arrays began over 100 years ago and their theory has been widely covered in the literature. References [40-43] provide a good review. However, this section introduces the basics of antenna arrays in order to familiarise the reader with the main concept and tradeoffs in antenna array design.

Definitions:

Radiation Pattern: A function describing the spatial distribution of field strength produced by the antenna.

Radiation Efficiency: The ratio of the radiated power to the total power delivered to the antenna.

Total Efficiency: The ratio of the total radiated power to the total power input to the antenna.

Effective area: The area of a perfect antenna which absorbs the same amount of power from an incident plane wave as the actual antenna

Directivity: The ratio of power per solid unit angle in the direction of the maximum to the average radiated power per unit solid angle.

Gain: The ratio of power per solid unit angle in the direction of the maximum to the average radiated power per unit solid angle delivered to the antenna.

Mutual Coupling: The change of an antenna element performance due to the presence of other antenna element in its environment.

Main Beam: The beam that contains the maximum radiation intensity

Side Lobes: are lobes in direction/s other than the main beam.

Grating Lobes: Additional main beams produced by the periodic-structure

Field Regions: The field surrounding the antenna and can in principle be divided into three regions:

1. *Far field*: The field region far away from the antenna where the radiation pattern does not change shape with distance.

2. *Reactive near field*: The field region in the immediate vicinity of the antenna. Here the electric and magnetic fields are 90 degrees out of phase

3. *Radiating near field*: The field region between the far field and the reactive near field. In this region, the radiation field can vary considerably with distance.

Antenna noise temperature: The noise temperature due to the antenna environment

System noise temperature: The sum of all noise sources in the system including the antennas, receivers and nearby electronics.

Sensitivity: The ratio between the total effective area and the overall system noise temperature.

Figure 1.3 shows an array of n isotropic elements separated by equal distance d along a single line. Assuming each element has equal amplitude and a progressive phase lead of β to the preceding one, the total field at a large distance in the direction of θ and referenced to source 1 can be written as

$$F = 1 + e^{j\psi} + e^{j2\psi} + e^{j3\psi} + \dots e^{j(n-1)\psi} \dots \dots \dots (1.1)$$

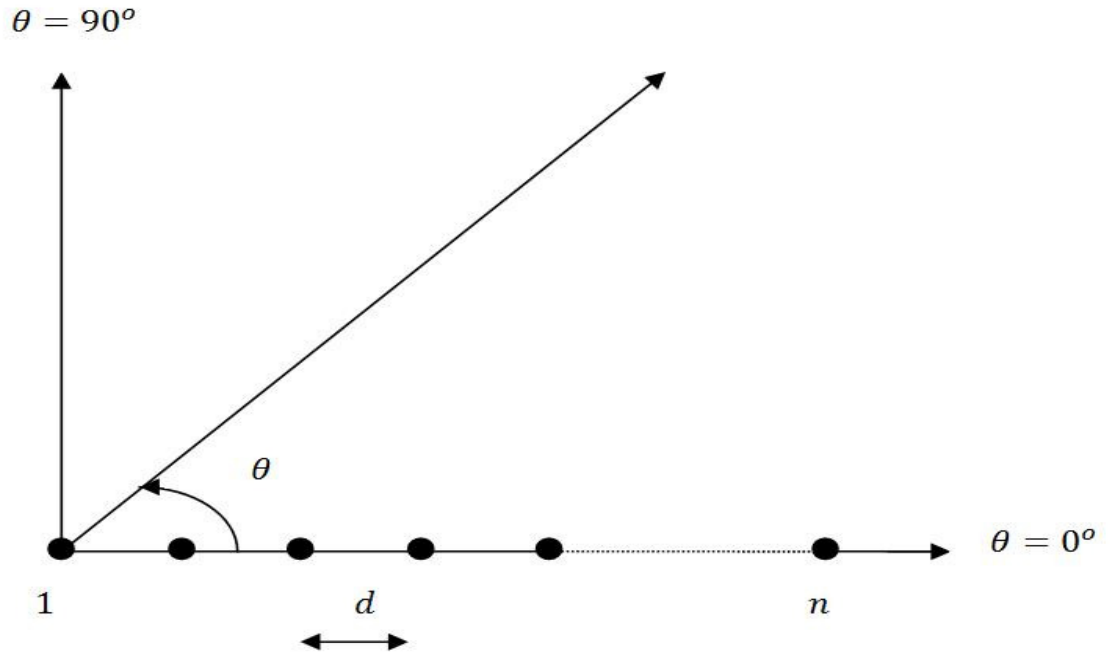


Figure 1.3 Linear uniform array

Equation (1.1) can be compacted as:

$$F = \sum_{m=1}^n e^{j(m-1)\psi} \dots \dots \dots (1.2)$$

Where F indicates the array factor, ψ is the total phase difference of field from adjacent elements and is expressed as:

$$\psi = k d \cos \theta + \beta \dots \dots \dots (1.3)$$

Where k is the wave number, written as:

$$k = \frac{2\pi}{\lambda} \dots \dots \dots (1.4)$$

Such an array is known as uniform array. The array factor of 16 elements array separated by an equal distance of half wavelength is shown in figure 1.4. The directivity of such array can be computed from the array factor as:

$$D = \frac{4\pi \max(F)^2}{\int_0^{2\pi} F^2 \sin\theta d\theta} \dots \dots \dots (1.5)$$

If the distance between elements exceeds one wavelength, the array is said to be under-sampled resulting in grating lobes appearing in real space as depicted in figure 1.5

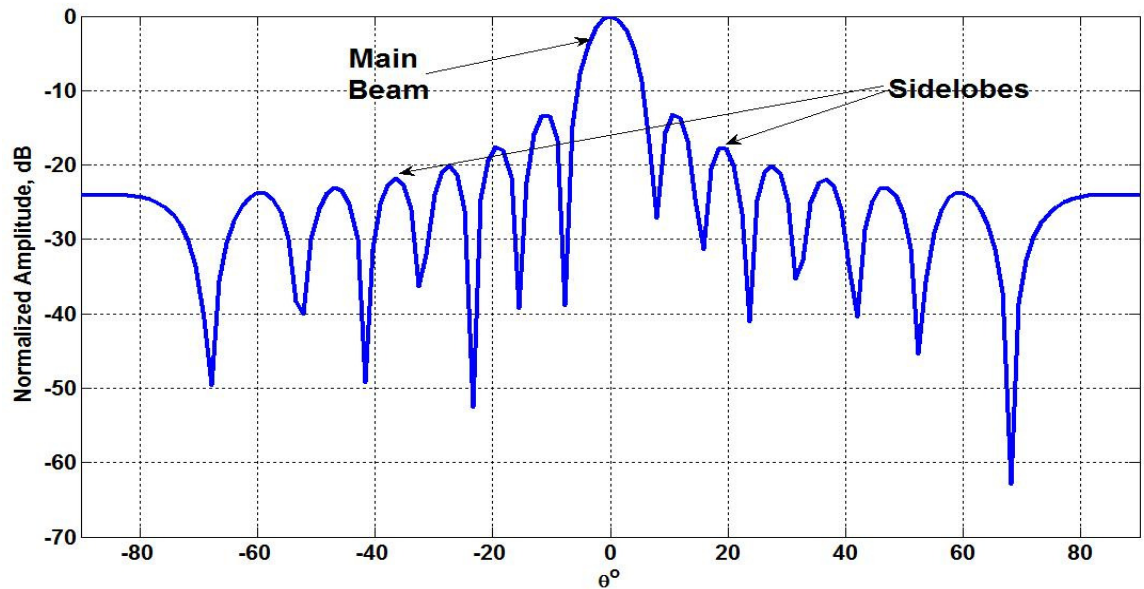


Figure 1.4 Radiation pattern of 16 element half wavelength separated linear array

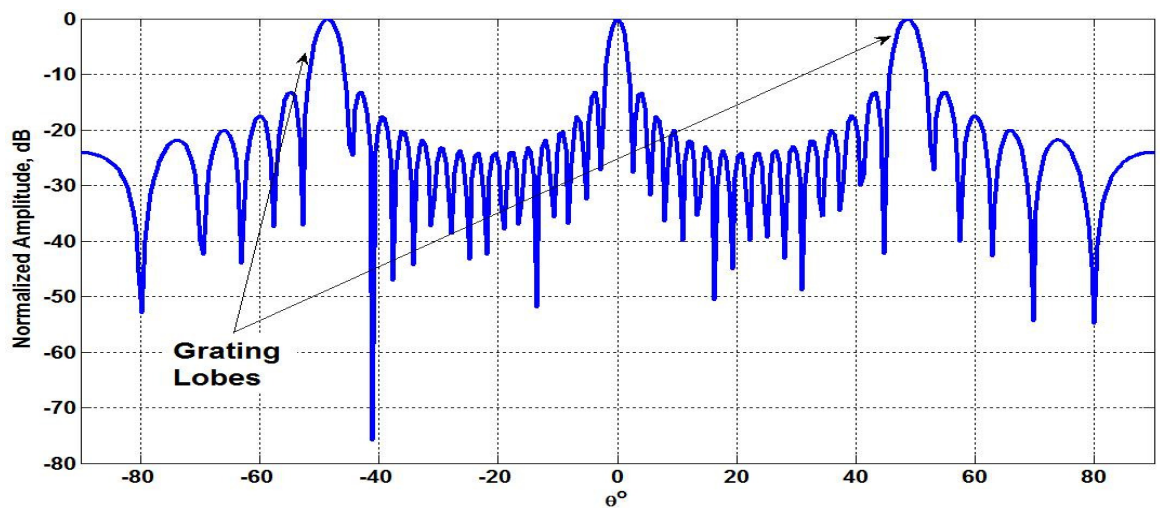


Figure 1.5 Radiation pattern of 16 element separated by a distance of 1.5 wavelength

It is possible to control the behaviour of the array by applying different relative phase shift at each element excitation to obtain different performance such as steering the main beam to a desired angle in space as shown in figure 1.6. The different excitations are known as weights W_n and equation 1.2 becomes

$$F = \sum_{m=1}^n W_n e^{j(m-1)\psi} \dots \dots \dots (1.6)$$

The above equations are valid for uniform linear arrays. However, as shown in section 2 of this thesis, the formulas are generalized for arrays of any number of elements and geometrical distributions

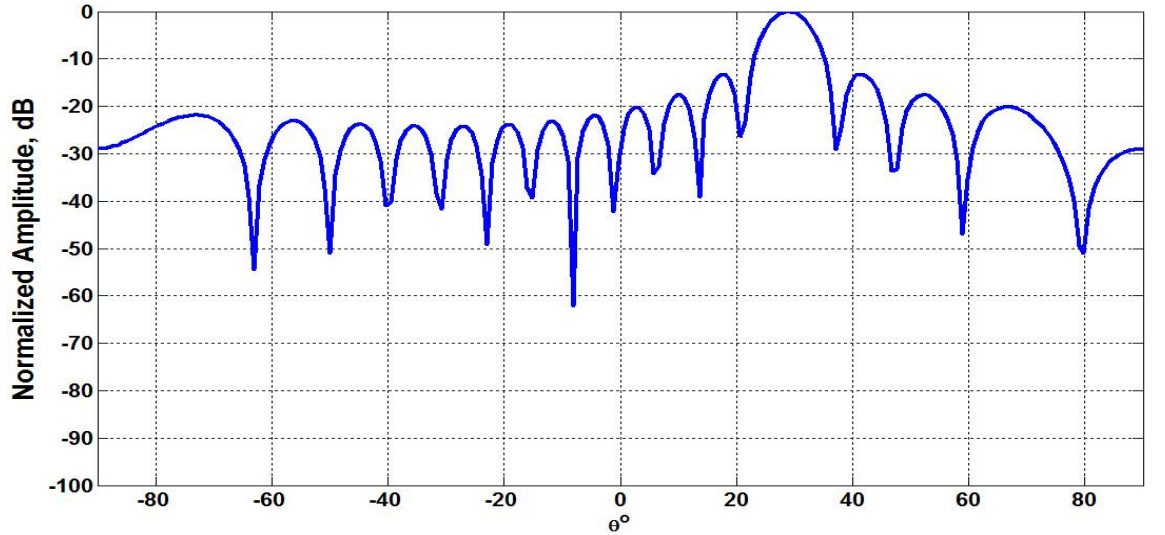


Figure 1.6 Radiation pattern of 16 element array with main beam scanning

A typical antenna array receive architecture is shown in Figure 1.7, where the signal received by each antenna element is amplified, shown here as Low Noise Amplifiers (LNA), and then passed through receiver chains¹. The signals from each element are then weighted and combined by a beamforming network to yield

¹ In this thesis, receive arrays are considered. However, from the theory of reciprocity, the basic approach applies to both receive and transmit arrays [52].

a single array output. An increasingly common approach, particularly in receive only arrays, is to implement the weighting and combination digitally to increase flexibility [66].

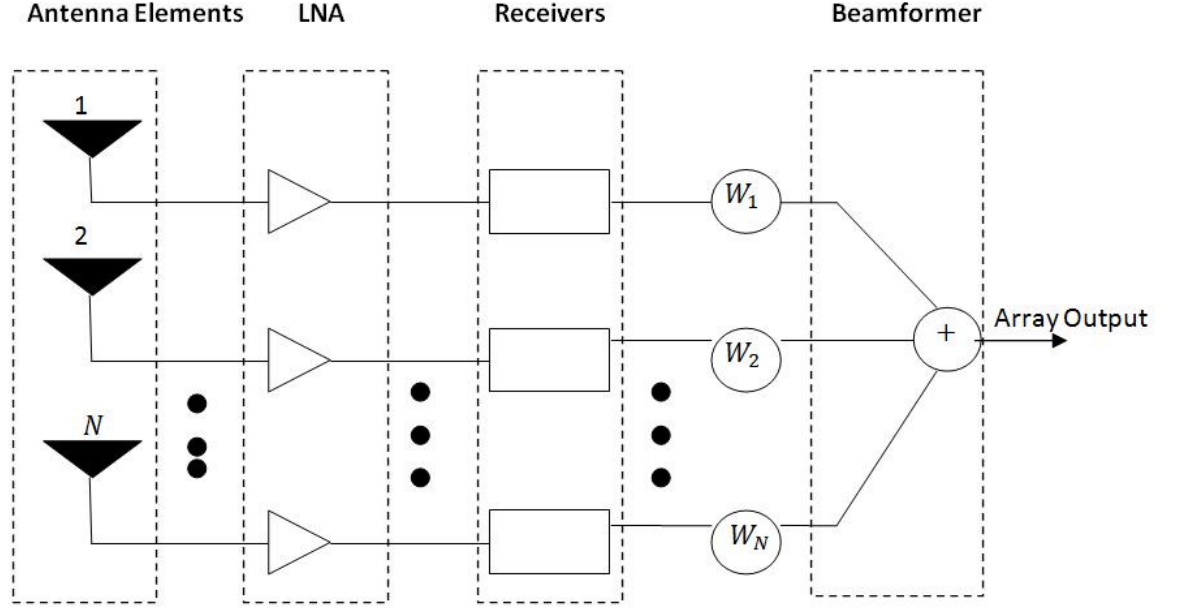


Figure 1.7: Typical receive antenna array system architecture

The main figure of merit of such array can be defined in terms of the overall effective area A_{eff} and the overall system noise temperature T_{sys} . This is known as the array sensitivity S [2] and is defined as:

$$S = \frac{A_{eff}}{T_{sys}} \dots \dots \dots (1.7)$$

The array effective area A_{eff} can be written as:

$$A_{eff} = \frac{\lambda^2}{4\pi} \eta_{total} D \dots \dots \dots (1.8)$$

Where λ is the wavelength, η_{total} is the overall array efficiency, and D is the directivity of the array [3]. See section 2.2 for more details.

The system noise temperature can be written as:

$$T_{sys} = \eta_{total}T_A + (1 - \eta_{total})T_{amb} + T_{LNA} \dots \dots \dots (1.9)$$

Where T_A is the antenna noise temperature, T_{amb} is the physical temperature with a typical value of 290 [Kelvin] and T_{LNA} is the low noise amplifier noise temperature [4].

The antenna noise temperature is the noise temperature due to the antenna array environment. The antenna noise temperature is due to various atmospheric, ground and cosmic sources [4]. The antenna temperature due to the sky brightness temperature at a particular frequency can be written as:

$$T_A = \frac{\iint |F(\theta, \phi)|^2 \cdot T_{sky}(\theta, \phi) \cdot \sin\theta \cdot d\theta \cdot d\phi}{\iint |F(\theta, \phi)|^2 \cdot \sin\theta \cdot d\theta \cdot d\phi} \dots \dots \dots (1.10)$$

Where F is the array radiation pattern, T_{sky} is the sky brightness temperature, θ and ϕ are the elevation and azimuth angles respectively [4].

The sensitivity can now be rewritten as:

$$S = \frac{\lambda^2 \eta_{total} D}{4\pi(\eta_{total}T_A + (1 - \eta_{total})T_{amb} + T_{LNA})} \dots \dots \dots (1.11)$$

The above equation shows that higher sensitivity can be achieved by increasing the array directivity D . The consequence is a large array containing many elements, increasing the complexity and the cost of the system. Higher sensitivity can also be achieved by reducing the system noise temperature, particularly reducing the antenna noise temperature. This can be achieved by reducing the array receiving power at angles of high noise sources, equation (1.10). Moreover, for broadband arrays, the angular location and magnitude of different noise

sources often vary across the band. In addition, the array directivity is also frequency dependant. Therefore, in order to reduce the complexity of the system, it is essential to be able to optimize the array directivity and radiation pattern over a broadband in order to meet certain sensitivity requirements with the minimum number of elements.

Inspection of equation (1.11) shows the relationship between sensitivity and the array total efficiency η_{total} , where its effect on sensitivity reduces when the antenna noise temperature is significantly larger than the ambient temperature (provided a reasonable LNA noise temperature is achieved). This is illustrated in figure 1.8 where the change in sensitivity due to the total efficiency is plotted for increasing antenna noise temperature. The figure shows the little impact of total efficiency on sensitivity for high antenna noise temperature.

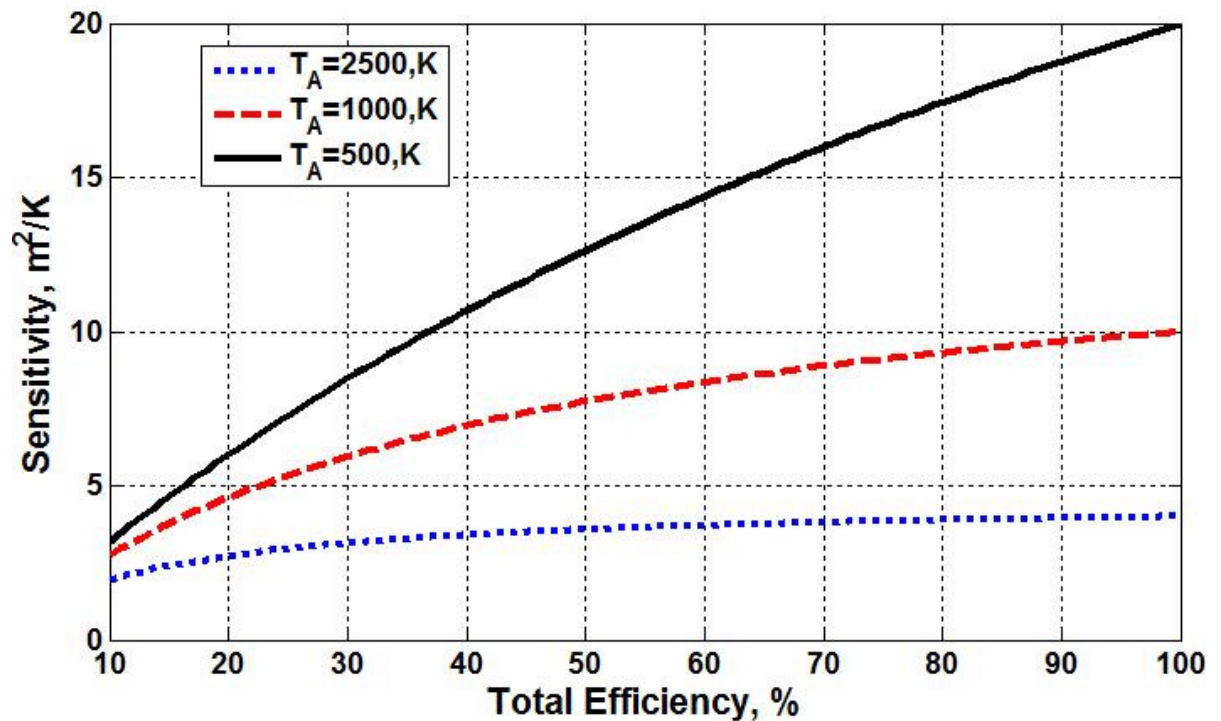


Figure 1.8: Sensitivity vs. Total Efficiency for different antenna noise temperatures

It is also possible to increase sensitivity by reducing the LNA noise temperature. However, LNAs and receivers are not considered in this thesis.

One way of optimizing broadband arrays is via element distribution². However, the element distribution affects other parts of the system such as beamforming capability and mutual coupling. This thesis studies the effect of element distribution on the broadband performance of antenna array outlining how it can be utilized to optimize the performance and reduce the complexity of the overall system.

The concept and design of antenna array systems are widely covered in the literature; references [40-43] provide a good back ground. The following subsections provide a literature review highlighting the main issues associated with designing large scale broadband antenna arrays. Section 1.4 lists a number of novel elements of the thesis

1.2.1 Array Geometry

Array geometry is defined in this thesis as the relative distribution of antenna elements within a certain defined aperture. The types of array aperture can be classified as Linear, planar, or conformal. A linear aperture has all elements arranged on a single straight line, whereas a planar aperture has elements distributed on a single plane³. In the case of conformal apertures, the elements are distributed over a three dimensional space.

The choice of geometry effects many aspects of the array performance including directivity, side lobes, and radiation pattern and hence, the optimum choice of

² In this thesis, the element distribution refers to the spatial locations of antenna elements. It is also referred to as array geometry or array configuration.

³ This thesis considers planar array geometry with circular outline.

geometry it is application dependant. For periodic arrays, a half wavelength regular separation is often used to satisfy the Nyquist sampling theorem [5]. Such an array is also referred to as fully filled, regular, or dense array. As the array is fully sampled, the directivity is proportional to the array aperture area for a given side lobe requirement. A large area is required in order to achieve high directivity, this leads to increase in the number of elements and therefore increasing the cost of the overall system. However, it has been shown that it is possible to maintain overall performance requirement tradeoffs with fewer elements than a dense array [6]. This however means that some elements are now separated by a distance larger than half the wavelength. This array is referred to as sparse, thinned, or under-sampled array⁴. The under-sampling often results in an increase in side lobe level reducing the directivity. However, in many antenna array applications low side lobes is essential to minimize interference from unwanted signals. Nevertheless, the antenna positions in a sparse array can be manipulated to reduce the effect of the under-sampling improving the side lobes and/or increasing the directivity.

Sparse array geometries are widely discussed in the literature. Early work in [6] demonstrates how an arbitrary distributed array has more degrees of freedom than a regularly distributed array and can therefore in general achieve the same performance with fewer elements. It is shown in [7] how the element position can be computed to satisfy a desired low side lobe radiation pattern. In [8] a controlled cosine method is used to generate a sparse broadband array with wide scan capability and side lobes less than -5 dB. However, such a side lobe level might be too high for some applications. In [9] a method is developed whereby the radiation

⁴ These terms are ill defined in the literature. However, they are used interchangeably in this thesis to refer to arrays containing element separation more than half wavelength.

pattern is converted into a series of integrals which can then be used with a function that determines the positions of a sparse array. A dynamic programming technique is developed in [10], which uses trial and error to iteratively determine the position of each element to achieve certain sidelobe performance criteria. Random sparse array is discussed in [11] where it is shown how a narrower beam can be achieved by distributing elements over a larger aperture without significantly increasing the side lobes or reducing directivity. Statistically thinned arrays are discussed in [12] where the number of elements can be reduced significantly, while maintaining good control on side lobes. A critical study in [13] shows that while the above techniques do provide lower side lobes in some cases, their resultant sidelobe level are however not truly optimum.

A comparison between randomly thinned arrays and algorithmically designed aperiodic arrays in [14] shows that algorithmically designed aperiodic arrays can in general be superior to random arrays in terms of side lobe performance. It concludes that such algorithms can avoid element locations that could cause unexpectedly high side lobes.

The concept of genetic algorithms (GA) was applied to linear arrays in [15] and [16] and compared with other optimization techniques. The studies show that even though they are slow, (GA) have been successfully applied to the design and optimization of thinned arrays. The concept of difference set is applied in [17] in order to largely thin phased arrays while controlling side lobe level. The method shows better sidelobe performance achieved over genetic algorithms and dynamic programming algorithms mentioned above. The study also concludes that the technique is useful when simultaneous beams are required. The work in [18] is a detail study on fractal antenna design and its potential application to both

antennas and array thinning. Further work is followed by the same authors in [19] combining the concept of fractal array with GA to devise array geometries with low side lobes over wide frequencies. Logarithmic spiral geometry is proposed in [20] and shown to have no grating lobes even with element separation of several wavelengths. Similar geometry is optimized in [21] for the purpose of multiple beams application in satellite coverage. A (GA) is used in [22] to reduce the number of elements in a concentric ring arrays to obtain side lobes as low as -27 dB are achieved. An array thinning method using pattern search is proposed in [23] where it is compared to previous (GA) thinning techniques. It's shown that pattern search is a faster approach to (GA) and leads to more optimum thinning provided that an appropriate starting condition is selected. Broadband array geometry based on optimization of aperiodic tiling is demonstrated in [24]. Such geometries are shown to widely extend the bandwidth of antenna arrays for many octaves while maintaining reasonable control on side lobes. The implementation of the proposed technique requires less computation than other search algorithms. Design aspect and tradeoffs between dense and sparse arrays for large radio telescope design are considered in [25]. The study shows the cost effectiveness of sparse designs for frequencies between 70-700MHz.

The techniques and algorithms to optimize array geometry in the literature can be classified as deterministic or non-deterministic or a combination of the two. A deterministic approach relies on computing the optimum element position according to a known analytical function such as in [17-20]. Whereas, a non-deterministic technique follows a certain search algorithm to determine the element location such as (GA) techniques in [15] & [16], or uses statistically based methods such as trial and error to determine element locations. The two

techniques can also be combined for more optimization such as in [24]. Non-deterministic approaches can in general require more computation than deterministic approaches since they involve some form of iteration. In the case of large scale broadband arrays, it is not only difficult to define an optimization function to account for array performance over the entire frequency band, but it would require large computational resources to carry out the iterations with no guarantee of convergence. Section 2.2 addresses this subject further and outlines the geometry optimization approach undertaken in this thesis.

1.2.2 Broadband Antenna Element

A frequency independent antenna can be defined as an antenna whose input impedance and radiation characteristics do not change with frequency. Since the radiation characteristics of an antenna depend on the ratio of its physical length to the wavelength, an antenna that has its entire geometry defined by angle and is infinite in length is frequency independent [26]. However, the antenna dimension is finite in reality, and so will be its bandwidth. Nevertheless, bandwidths as wide as 20:1 have been achieved [27].

The choice of broadband element type for an array depends highly on the array geometry and the overall application. One major trade off is directivity vs. array scanning performance. While high directivity is usually required to provide better signal to noise ratio, a high directivity means low power is radiating at far angles therefore limiting the scanning performance. In addition, high directivity requires in general, larger physical structures forcing larger element separations and hence limiting the scanning performance further and increase side lobes.

The design of an antenna as a broadband array element depends on the geometry and can be classified as infinite or finite array design. In the case of large periodic arrays, most antennas experience similar effects from neighbouring antennas due to the symmetry except for edge elements, and therefore best optimized in the array environment. In aperiodic arrays, and small periodic arrays, the effect on each element varies across the array, and therefore best optimized in isolation. While it is not the main focus of this research to study the detailed design of different broadband antennas for large array systems, a tapered slot broadband antenna is designed in order to study the effect of the geometry and verify the concept. This is discussed further in section 2.3

1.2.3 Mutual Coupling

The impedance and radiation characteristics of an antenna element in an antenna array can change due to radiation from neighbouring elements. This is known as mutual coupling. In periodic arrays, this effect can be utilized to optimize the impedance matching of antenna elements for broadband performance. This is made possible by the symmetry of periodic arrays where each element is in similar coupling environment. However, for aperiodic arrays the coupling effect can vary significantly for each element resulting in different impedances and embedded radiation patterns for each element. This can cause impedance mismatch across the array reducing efficiency, in addition to resulting in an undesired array radiation patterns such as increase of side lobe level and hence a drop of directivity. However, the effect of mutual coupling might be reasonably represented in the mutual coupling matrix which can in certain circumstances be solved for voltage weights that can be applied in order to compensate for the effect of mutual coupling and rectify performance. Nonetheless, under severe coupling conditions,

higher order currents might be present expanding the mutual coupling matrix making a solution for compensation more difficult to achieve. See section 2.4 for more details.

Computing the mutual coupling effect is therefore important, in order to accurately model antenna array systems, and many techniques have been developed and optimized. These techniques can in general be classified as:

1. **Analytical solution:** This technique relies on calculating the impedance change on one antenna in the presence of another radiating antenna as a function of distance. This can then be repeated for all antenna elements in the array forming the mutual coupling matrix. In [28] the mutual impedance as a function of distance for infinitely thin wire dipoles is presented. It shows that the mutual impedance reduces significantly when the dipoles are more than one wavelength apart where it becomes negligible at wider separations. Other analytical solutions are discussed in [29] for finite arrays. Analytical solutions are very useful since it directly fills the entries of the mutual coupling matrix and can be optimized for the analysis of sparse arrays where the computational complexity can be reduced [30]. However, this is true only when the geometrical structure of the antenna element under consideration is relatively simple. An analytic closed form solution is not normally available for complex elements, making it necessary to use numerical techniques for more accurate modelling. This greatly increases the computational complexity of the problem.

2. Full-wave solution: A full-wave solution refers to various numerical methods that aim to solve Maxwell's equations for electromagnetic modelling. This process is also known as Computational Electromagnetic Modelling (CEM). The choice of method for modelling depends on the nature of the problem since each method has its own advantageous and disadvantageous. Finite Element method (FEM) and Finite Integration Technique (FIT) have been widely implemented in many commercial software such as HFSSTM and CST for three dimensional full wave simulations. In this type of modelling the problem space is defined around the antenna and the whole of its interior which has to be meshed normally in cubic cells, including free space. While providing good modelling accuracy including complex geometries and materials, they demand large computational resources when the size of the problem increases. A more computationally efficient technique is the Method of Moment (MoM) which calculates currents flowing on surfaces from which it calculates radiation properties. As it is only meshing surfaces, it is more efficient in terms of computational resources but its only limited to problems involving good conductor. Once the full wave solution is obtained the impedances and radiation characteristic at any point in the array can be determined including the mutual coupling. Reference [31] provides a good background on the various CEM techniques.

1.2.4 Beamforming

Beamforming is a widely used signal processing technique in antenna array applications. The aim is to maximize or minimize the radiating power in certain direction/s in order to increase the signal to noise ratio. This is particularly useful in

applications where the direction of the desired signals and noise are known. This can be achieved by forming a desired radiation pattern shape, and calculating the appropriate weights to be applied. Many beamforming algorithms are covered in the literature for narrowband and wideband applications [27] and [32]. This includes Amplitude Tapered (AT), Mean Square (MS), Linear Constraints Mean Variance (LCMV), null steering (NS), Sample Matrix Inversion (SMI) etc. These methods are also applicable to sparse arrays, however, the under-sampling and irregularities due to the large and arbitrary element separations imposes a limitation on achieving an optimum desired radiation pattern [36]. Moreover, the presence of varying mutual coupling between the elements exerts extra constraints on the ability of the beamformer to achieve desired performance. Therefore many beamforming techniques rely on numerical solution and iteration to achieve an optimum solution such as (GA) in [37]. A general broadband beamforming algorithm is proposed in [38] where the optimum weights can be computed for any array geometry. A method is proposed in [39] based on re-sampling the optimal Dolph Chebyshev window computed for a uniform line or planar array of equivalent aperture at the element position of the irregular array. A beamforming algorithm for arbitrary array in the presence of mutual coupling is presented in [40]. The algorithm relies on the embedded element pattern and the coupling matrix to compute the weights that minimize radiations in certain directions while maintain maximum radiation in the desired direction. A review of various mutual coupling compensation methods in antenna arrays can be found from [42]. The paper also comments on the advantages and disadvantages of different compensation algorithms. In this thesis, the effect of array geometry on different beamforming schemes is compared. This is presented in chapter 6.

1.3 Large scale broadband array design tradeoffs

The previous sections illustrate the main principles of broadband antenna array systems. For large scale arrays, the main complexity is due to the large number of antenna elements required to fill such large array apertures in a uniform distribution. Reducing the number of element in a uniform distribution in order to reduce complexity, results in under-sampled or thinned array increasing the side lobe level and reducing the directivity. However, the element distribution can be manipulated to reduce the effect of thinning. Therefore, one tradeoff is directivity and side lobes versus the number of elements. In addition, due to broadband requirements, the distribution of the elements must tradeoff directivity and side lobe that can be obtained at a narrow band to improve directivity and side lobes over wider bandwidths. Moreover, the above tradeoffs often affect the performance of the antenna element, the mutual coupling, in addition to beam forming operations. Therefore, further tradeoffs have also to be considered such as the antenna element size, radiation pattern, and the minimum separation between the antenna elements in the array. Chapter 2 illustrates these tradeoffs further.

1.4 Contribution

The vast majority of array thinning studies aim to reduce the number of elements in relatively small antenna arrays for narrow band applications. While some of these techniques are applicable to broadband applications and larger arrays, the majority rely on search techniques such as (GA) and pattern search. Even though other studies optimized many of those techniques for speed, they suffer from computational complexity when applied to large broadband arrays with many

thousands of elements. This is due to the increasing size of optimization parameters, since thousands of positions need to be optimized over many frequency bands, while providing no guarantee to the geometry being optimum. Moreover, most studies consider idealized element radiation patterns with mutual coupling effect being ignored which can reduce the practical evaluation of array performance. In addition, most of the array thinning studies focused on the optimization of the side lobe level with little attention to directivity particularly over a broadband.

This thesis considers the different performance and cost tradeoffs associated with large scale broadband arrays including the effect of the antenna element and their mutual coupling. Novel elements of the thesis include:

- *Provide a new approach to designing large scale broadband array geometries. The technique can be rapidly applied giving a greater insight to the main tradeoffs making it suitable for optimizing wide range of applications.*
- *Study the performance of different geometries by integrating a broadband antenna as an array element.*
- *Study the mutual coupling effect for different geometries*
- *Investigate the beamforming limitations for different geometries.*
- *Demonstrate how this study can be utilized to optimize the cost and performance of a large scale broadband array as a radio telescope for astronomical applications.*

The study also includes the construction of hardware model for optimized geometry pattern measurements.

1.5 Chapter Summary

Large scale broadband antenna arrays are becoming increasingly popular for highly sensitive radio imaging and detecting instruments. The large size and bandwidth increases the cost and complexity of the system making them difficult to achieve in practice. However, previous work shows that through antenna element distribution, many tradeoffs and optimizations can be achieved, which can reduce the number of antenna elements for a certain requirement/s, thus reducing the cost and complexity of the overall system. Nonetheless, the existing techniques consider small size broadband arrays or narrowband arrays with little attention to the effect of mutual coupling between neighbouring antenna elements.

This thesis investigates the effect of the array geometry on the broadband performance of large scale antenna arrays. It illustrates the advantageous and limitations of the geometry and its impact on the design of the overall system including mutual coupling and beamforming capabilities. The study provides a useful design tool for cost and performance optimization of large scale broadband antenna arrays. This is achieved through the new design approach adopted in this thesis taking into account the effect of various system parts on the overall performance.

Chapter 2: Approach

2.1 Introduction

From chapter 1, the design complexity of antenna array systems is due to the complex interaction between different parts of the system such as array geometry, antenna element and their mutual coupling. The complexity is increased in further in broadband systems due to the size of the problem where many parameters have to be optimized for many frequencies.

The thesis adopts an approach where the effects of each part of the system on the overall performance are considered progressively. Initially, the broadband effect of the antenna element distribution on the array directivity and the sidelobes is studied for a wide range of geometries. This is achieved through a self built code in Matlab. The code is written to efficiently handle large arrays. The study then shows how these arrays can be scaled to any frequency band and aperture size. The scaling concept is then verified by including a broadband antenna element and comparing the full wave solution of smaller scaled arrays which includes the mutual coupling effect. The full wave solution is also used to verify the effect of the geometry on the array performance and its impact on mutual coupling and beamforming.

The thesis then presents a hardware design for radiation pattern measurements of a 32 element sparse array with low mutual coupling and low sidelobes. The aim of

the hardware design is to verify the benefit of the element distribution on the array performance. The study concludes by proposing optimized array geometries suitable as a broadband radio telescope for low frequency radio astronomy.

2.2 Geometry Optimization

The distribution of antenna elements in an antenna array plays a major role in the performance of the overall antenna array system.

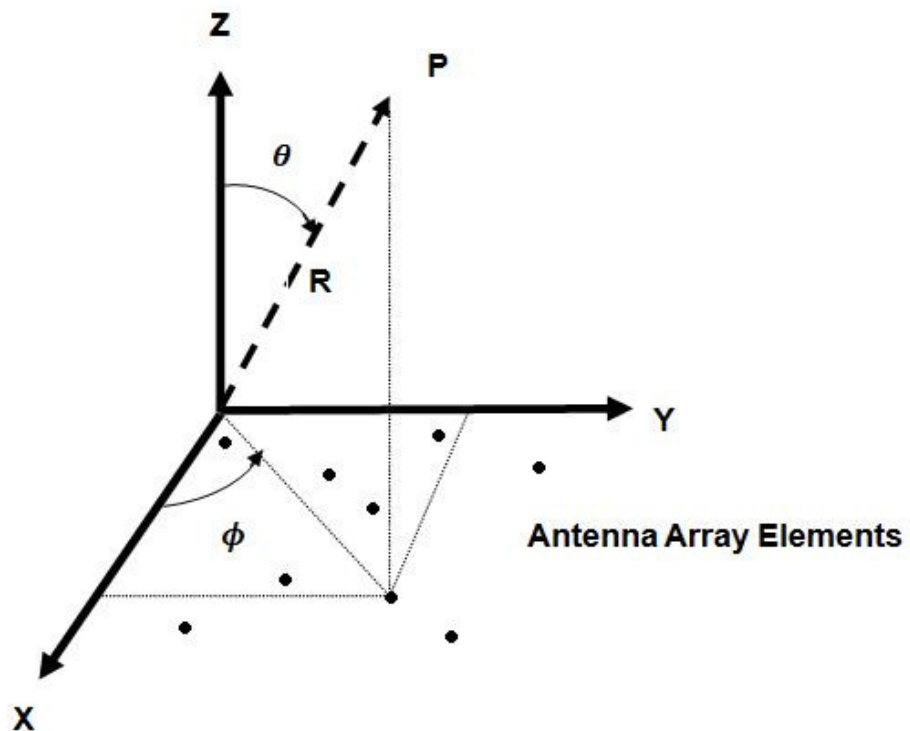


Figure 2.1: Array coordinate systems

Consider the coordinate system shown in figure 2.1 where the antenna elements are distributed on the $X - Y$ plane. Assuming each element has an equal amplitude and phase and is radiating in the positive z direction, the total field at the observation point P at a distance R from the origin is equivalent to the sum of all the antenna fields contribution at the specified angles θ and ϕ . This can be calculated for all angular space to yield the array factor which can be written as:

$$F(\theta, \phi) = \sum_{n=1}^N e^{[jk(x_n \sin \theta \cos \phi + y_n \sin \theta \sin \phi)]} \dots \dots \dots (2.1)$$

Where N is the number of elements in the array, k is the free space wave number, θ and ϕ are the elevation and azimuth angles respectively, and (x_n, y_n) are the coordinates of the n^{th} element in the $X - Y$ plane, figure 2.1

The array directivity at a particular angle can be defined as the ratio of the power radiated by the array at that angle in space (θ_0, ϕ_0) to the power radiated from an isotropic radiator.

$$D = \frac{4\pi F^2(\theta_0, \phi_0)}{\int_0^{2\pi} \int_0^\pi F^2(\theta, \phi) \cdot \sin(\theta) d\theta d\phi} \dots \dots \dots (2.2)$$

If the direction (θ_0, ϕ_0) is the direction of the maximum radiating power, then the directivity is also a maximum (Peak Directivity). The direction of the maximum radiating power is often contained in the main beam whereas radiating power in other directions is referred to as side lobes. The gain is equal to the directivity minus all the losses in the array system which can be written as:

$$G = \eta_{total} D \dots \dots \dots (2.3)$$

where η_{total} is the total efficiency

From equation 2.2, the directivity D of a single hemispherical element radiating in the positive z direction in figure 1.1 is equal to 2 or 3dB. It is clear from equations 2.1 and 2.2 that the array factor, and subsequently the array directivity depend on the number of antenna elements N and their relative positions in wavelength. It is often desired to maximize the array directivity from a certain number of elements.

For a rectangular periodic array at boresight with the main beam along the z axis in figure 2.1, the maximum possible directivity D_{max} is achieved at frequency f_{max} corresponding to element separation of approximately $0.9\lambda_{max}$. Since the total array directivity is related to the total radiation pattern from all the elements, which is the summation of the total voltages received from each element, and not the linear summation of individual antenna directivities, the achieved directivity can be larger than $N \times D$ ⁵. However, the achieved array directivity compared to $N \times D$ is considered in this thesis as a fair cost efficiency assessment figure over the band. In the case of broadband arrays, for frequencies less than f_{max} the array directivity drops due to the decrease of aperture size in wavelength broadening the main beam. At lower frequencies the array directivity can be less than $N \times D$ due to many elements becoming too close together in terms of wavelength reducing their contribution to the array directivity. The effect of directivity drop at low frequencies can be referred to as oversampling. This oversampling means that the array is redundant in terms of number of elements and is therefore inefficient from a cost point of view. On the other hand, for frequencies above f_{max} , the array directivity also drops, this time due under-sampling caused by element separations larger than one wavelength. The under-sampling results in an increase in side lobe levels thus reducing the array directivity which can be less than $N \times D$ at higher frequencies. However, the effect of the under-sampling can be reduced by manipulating the element positions to decrease side lobes and maintain high directivity over the band. This must come at the expense of reducing the peak D_{max} achieved over a narrow band to obtain better directivity and sidelobe performance over a broad frequency band. In other words, the optimization of

⁵ For a hemispherical element radiation in the positive z direction $N \times D = \log_{10}(2N)$

broadband array geometry trades off maximum possible directivity achieved from N elements at narrow band for directivity and side lobes over a wide bandwidth. In many broadband antenna array applications contribution from various noise sources might vary across the band making it necessary to maintain high directivity at those frequencies as mentioned in section 1.2.

As discussed in section 1.2.1, various methods of designing sparse array geometries aim to reduce the number of elements in a dense array while maintaining certain predefined performance criteria (hence the term thinning). Other methods intend to determine the minimum number of elements to satisfy a desired performance. In this thesis, a method is proposed whereby a constant aperture size is defined that is allowed to contain a constant number of elements. The positions of elements can now be changed and optimized using different non iterative techniques yielding different geometries where the performance of directivity, mean and peak side lobes as well as radiation patterns can be compared over a wide band. The constant aperture size and number of idealized elements allows comparison of different arrays from a pure geometrical point of view. This enables the designer to closely understand different performance tradeoffs for a wide range of geometries in order to select the best choice suitable for the application. Since this research deals with large scale arrays containing many thousands of elements, the method avoids iterative search techniques, which often require computing the array performance at each iteration. Instead, simple space tapering⁶ and randomization techniques are used. In other words,

⁶ In this thesis, the term tapering, unless explained otherwise, refers to the physical displacement of antenna elements in the array according to certain tapering function. It should not be confused with amplitude tapering where each element is giving a certain relative weight. The latter is discussed in section 7.4

the method aims to optimize the array performance bandwidth of N elements through their distribution.

The geometry optimization method proposed in this thesis consists of two stages. The first stage starts by initially assuming a relatively large (1000) number of elements operating at a very wide bandwidth of (20:1) that can be distributed anywhere within a constant $100\lambda_H$ diameter circular aperture, where λ_H is the wavelength of the highest frequency. Initially, a hemispherical element is assumed over the band. The directivity, side lobe and radiation patterns performance over the band for different geometries are then compared for tradeoffs. The radiation patterns for each frequency point over the considered band can be calculated from equation 2.1. Subsequently, the directivity is calculated using equation 2.2 for the corresponding frequency point. The side lobe level locations can be obtained by applying the prebuilt (image regional maxima) function in MATLAB to the radiation pattern data obtained from equation 2.1. The function identifies the locations of all peaks in the data and by eliminating the peak of the main beam the average and maximum side lobe levels are obtained. This process is repeated for each frequency point to obtain the peak and mean side lobe level over the band.

Since the minimum element separation in the array distribution imposes a limitation on the maximum element size, different geometries are also compared according to their minimum separation d_{min} in addition to the maximum and average separations d_{max} and d_{av} in order to give more insight into the geometry. Inspection of equation 2.1 and 2.2 reveals the computational complexity in obtaining the radiation pattern particularly when the array size is large in terms of wavelength. Therefore the self built MATLAB antenna array computational tool has

been built using matrix multiplications and avoids using loops to increase the speed. The simulation then would require a large memory machine to handle the corresponding large matrices. The code also allows for an antenna element radiation pattern to be included as the element pattern in addition to amplitude weights for comparison with full wave simulations in chapters 5 and 6.

This first stage is applied to various periodic and aperiodic arrays in chapters 3 and 4 respectively. The second stage of the method is discussed in chapter 5 where it is shown how the arrays can be scaled to any desired size and frequency band.

2.3 Broadband Antenna Element Design

The geometry analysis outlined in the previous section and later applied in chapter 3 and 4 assume infinitely small size elements with (20:1) bandwidth. However, the array bandwidth is ultimately limited by the finite bandwidth of the antenna elements. Moreover, the element physical size forces a constraint on the minimum separation allowed in the array distribution. The antenna element must be optimized to meet the low frequency requirements with the minimum physical size in order to allow for more geometry flexibility. As mentioned in section 1.2.2 the type of broadband element design depends on the geometry and can be categorized as:

1. **Infinite arrays:** For large periodic arrays, the effect of symmetry is utilized where the antenna element is optimized in the array environment where the radiation from neighbouring antenna elements increase the effective aperture of the antenna improving its matching at low frequencies. The

performance of the remaining antenna elements will be approximately the same due to the symmetry except for edge elements which can be ignored for large arrays [43]

2. Finite arrays: For irregular arrays, the asymmetry can cause significant variations on the performance of each element due to the variation of the electromagnetic environment seen by each element. These variations increase when neighbouring antennas are closely separated in terms of wavelength. Details of infinite vs. finite array modelling can be reviewed from [44]

There exist many types of broadband antennas such as log periodic antenna [45], Horn antenna [45], bowtie antenna [46] and tapered slot antenna [47].

For an element that has a radiation pattern $A(\theta, \phi)$, equation 1 can be extended as:

$$F(\theta, \varphi) = \sum_{n=1}^N A(\theta, \phi) e^{[jk(x_n \sin\theta \cos\phi + y_n \sin\theta \sin\phi)]} \dots \dots \dots (2.4)$$

Equation 2.4 shows the importance of the element radiation pattern on the overall array radiation pattern where the elements receive field at a particular angle is multiplied by the array factor. To first order, the isolated element⁷ radiation pattern can be assumed as the element radiation pattern A , in equation 2.4. The resultant array radiation pattern does not account for the mutual coupling effect. The mutual coupling effect can be included by using the active element radiations patterns [48]. The active element pattern for a particular element in the array can be

⁷ The Isolated element radiation pattern refers to the radiation pattern of a single element.

calculated by exciting that element while all other elements in the array are terminated in a match load.

A broadband antenna is generally more complex in shape than a narrow band antenna [44], and the choice of an antenna as an array element depends highly on the application. The main tradeoffs include directivity, scanning performance, bandwidth and size. Since the main aim of the thesis is array geometry optimization, many broadband element types can be chosen as the array element.

- Fork Tapered Slot Broadband Antenna

A linearly polarized fork tapered antenna has been designed in this thesis to be used with the geometry optimization. The antenna is shown in figure 2.2 with a maximum length of one wavelength and a maximum width of half wavelength at 300 MHz.

Introducing slots in the antenna front, as can be seen from figure 2.2, extends the effective length of the aperture extending the antenna low frequency operation while maintain a relatively smaller antenna. This technique is useful since it allows for more flexibility on the element spacing in the array. A smaller antenna might also reduce its cost.

$$\lambda/2$$

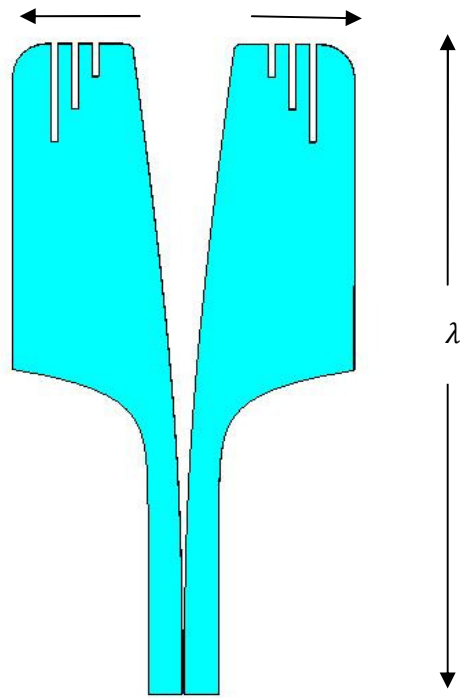


Figure 2.2: Fork tapered slot broadband antenna

The antenna is optimized to operate between 400-1300 MHz with a relaxed matching at around 300 MHz.

The return loss is shown in figure 2.3

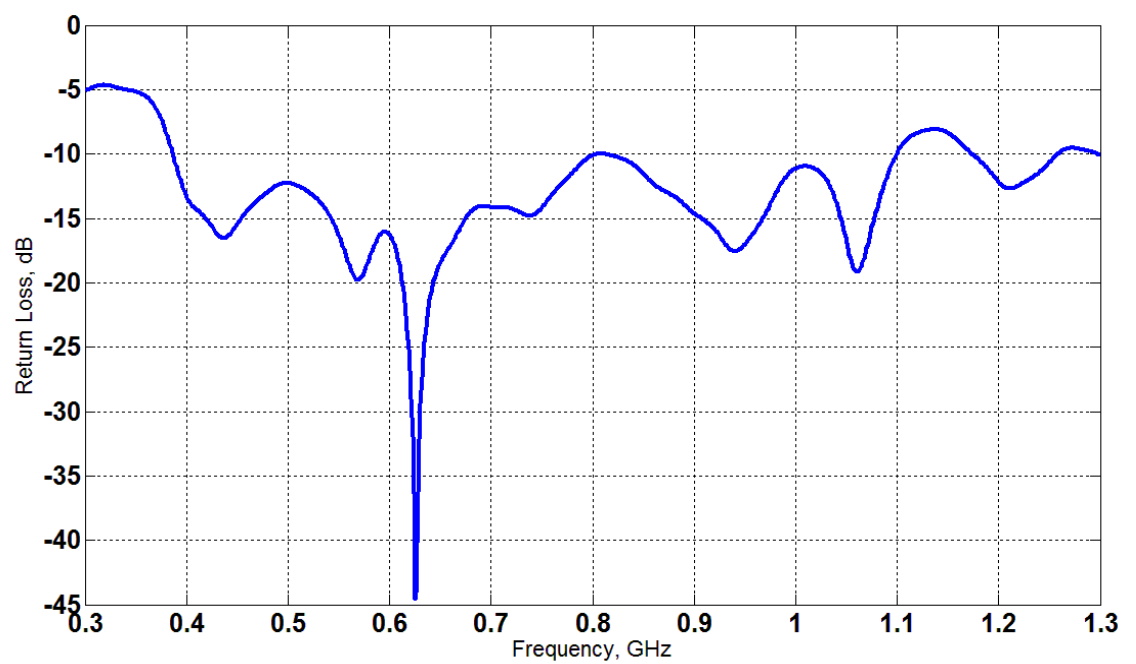


Figure 2.3: Fork tapered slot antenna return loss

The antenna was also designed to have a reasonably constant directivity and radiation patterns over the band in order minimize its effect on the overall radiation pattern. The E and H plane radiation patterns at various frequencies are shown in figures 2.4 and 2.5 respectively.

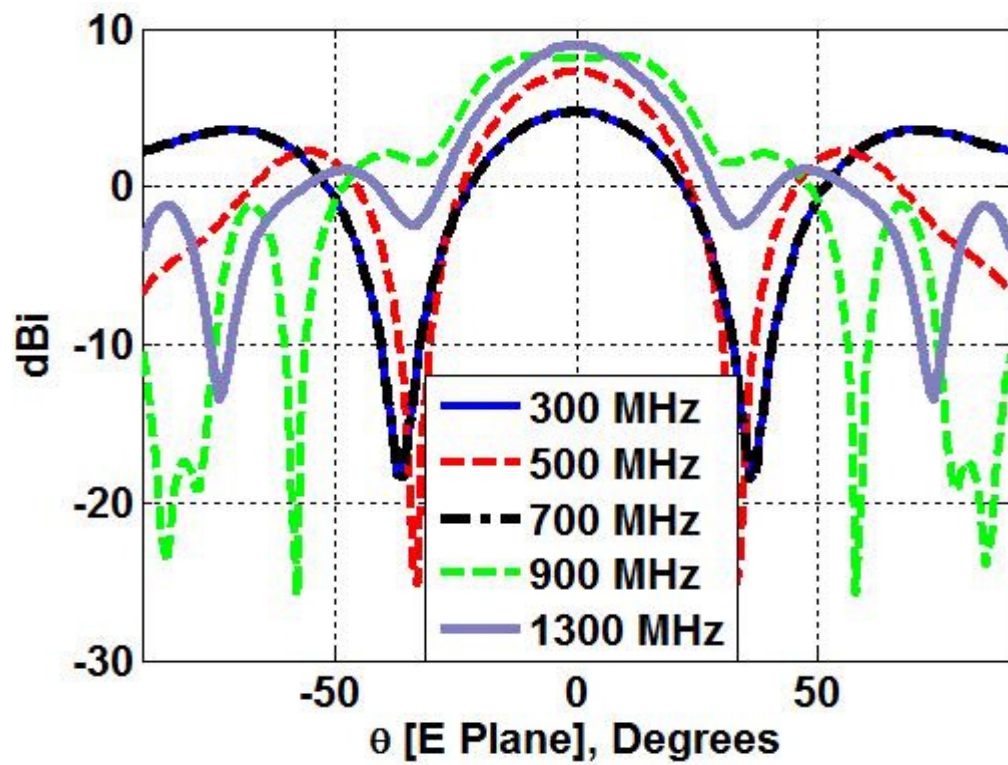


Figure 2.4: Isolated fork tapered slot antenna E plane radiation pattern

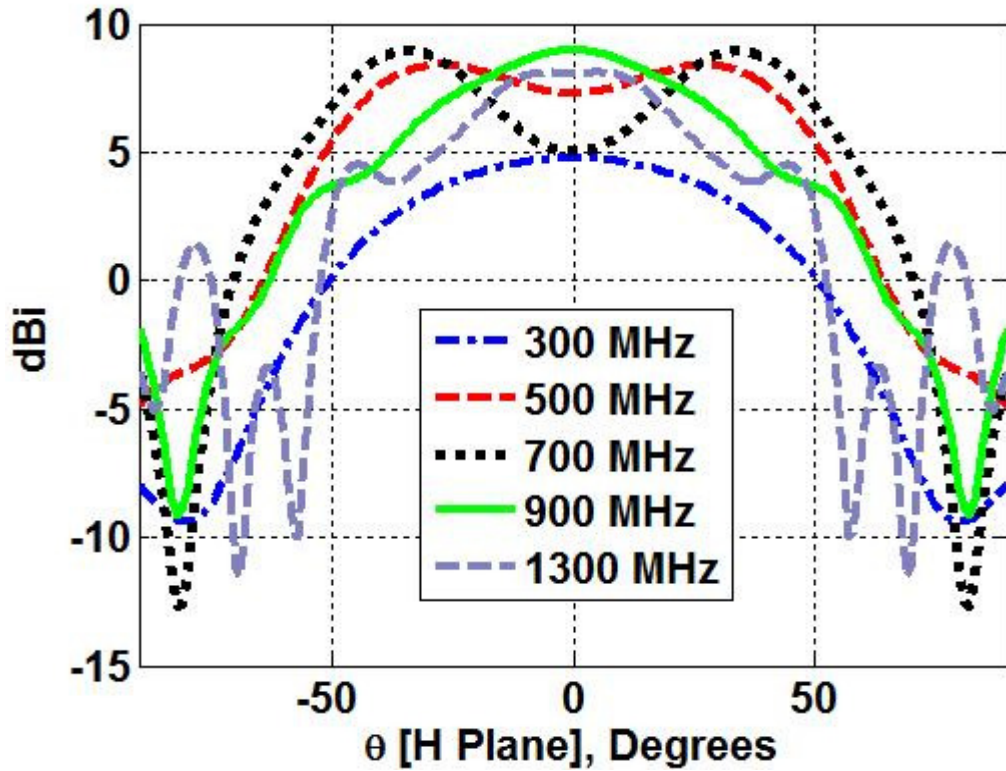


Figure 2.5: Isolated fork tapered slot antenna H plane radiation pattern

2.4 Mutual Coupling Consideration

In many antenna array analyses, it is common to assume that the elements are independent and the geometry study in chapters 3 and 4 are based on this assumption. In practice, the elements interact together for each antenna element, radiation from other neighbouring antenna elements are received, disturbing its current flow and hence its radiation pattern and impedance. This effect is known as mutual coupling. It is possible to derive an element pattern which includes the effect of mutual coupling in the array this is known as the embedded element pattern or the active element pattern [47].

In general, the effect of mutual coupling on an antenna element depends on the antenna element structure and the distance to adjacent elements. At large separations, the power received by an antenna element from its neighbours is

small compared to the power driving that antenna element and hence the mutual coupling effect can be ignored. However, as the separation is decreased, the power received by the antenna element from its neighbouring elements becomes larger. This however might not significantly alter the shape of the main current flow on the antenna element but can change the amplitude and phase of its feed point. Mutual coupling can therefore be viewed as changing the input impedance of the element and subsequently changing the matching between the antenna feed point and the feeding transmission line. This mismatch results in power being reflected by the antenna reducing its efficiency and ultimately changes the performance of the overall array. In such a case, the effect of mutual coupling can be compensated by changing the amplitude and phase of the antenna element drive voltage in order to cancel the effect of the mutual coupling. At very small separations, the power received from neighbouring antennas becomes significantly high and can alter the main current flow on the antenna element. In this case the effect of mutual coupling is no longer directly related just to the feed point amplitude and phase and a complete correction cannot be to achieve. The distance at which this occurs depends on the antenna element structure. However, for low directivity elements it can be shown that close separations can be realized without significant errors [49].

From the above we can see that as long as the effect of mutual coupling does not significantly alter the main current flow on the antenna element, the mutual coupling effect can be represented by the impedance change of the antenna element feed point due to all other elements.

Consider a simple antenna element of input impedance Z and driven by a source voltage V_{in} with internal impedance Z_s . Then, the current delivered to the antenna is given by:

$$V_{in} = (Z_s + Z)I \dots \dots \dots (2.5)$$

The voltage change dv on the antenna element due to the radiation from a neighbouring element can be written as

$$dv = Z_m I \dots \dots \dots (2.6)$$

Where, Z_m is the mutual impedance

For an N identical element coupled array the total voltage on the n th element is the sum of the drive voltage and all the voltage changes due to all other antenna elements. This can be generalized as:

$$V_N = \begin{bmatrix} Z_{11} + Z_s & \cdots & Z_{1N} \\ \vdots & \ddots & \vdots \\ Z_{N1} & \cdots & Z_{NN} + Z_s \end{bmatrix} I_N \dots \dots \dots (2.7)$$

Or in matrix notation

$$\bar{V} = \bar{\bar{M}} \cdot \bar{I} \dots \dots \dots (2.8)$$

Where \bar{V} is a N column matrix of elements drive voltages, \bar{I} is a column matrix of elements current and $\bar{\bar{M}}$ is a generalized mutual coupling matrix of order $N \times N$ with its diagonal representing the elements free space input impedance. In the case of no mutual coupling, the matrix $\bar{\bar{M}}$ is a diagonal matrix with all the mutual impedances being zero. Providing that the assumption of an insignificant current

alteration on the coupled antenna elements holds, the above equation can be solved for the correction voltages to be applied at each element to compensate for the mutual coupling effect. This is considered in section 6.2.

From section 1.3, an analytical solution for a generalized antenna element to include the mutual coupling effect is difficult to achieve due to the complexity of the problem and the variations of each array design. However, numerical full wave solution algorithms have been developed which can accurately compute the performance of array antennas. As mentioned in section 1.3, these numerical solutions become computationally intensive as large structures are considered. This requires the development of a special full wave numerical solution computational tool such as in [65]. Unfortunately, such computational tools for reliable calculations of complex array geometry are not fully matured. This thesis shows how the full wave solution of relatively smaller scaled arrays can provide reasonable assessments and predictions of the overall effect of mutual coupling on the array performance due to the array geometry. This is discussed further in chapter 5. In chapter 6, selected geometries are compared for mutual coupling cancellation in addition to scanning and amplitude taper.

2.5 Experimental model

An experimental array model of 32 dipoles is designed for a narrowband measurement. The aim of the model is to verify the radiation pattern characteristics achieved by the array due to the element distribution and the negligible effect of mutual coupling for such a sparse design. This is considered in chapter 7

2.6 Application

Preliminary specifications for the Square Kilometre array (SKA) radio telescope can be reviewed from [57]. One requirement includes the low frequency Aperture Array (AA) operating between around 70MHz and 450 MHz. Due to the relatively bright sky at these frequencies, a large effective area (and subsequently a large array) is required to meet the minimum overall sensitivity of the SKA of $4000 \text{ m}^2/\text{K}$. This requires a large number of elements increasing the cost and the complexity.

Chapter 8 shows how the studies undertaken in this thesis can be utilized to minimize the number of elements required to meet the minimum sensitivity requirement over the band.

2.7 Chapter Summary

The design of broadband antenna array systems suffers from high complexity due to the complex interaction of many subsystem parts. An approach is devised in this thesis where each part of the system is considered progressively. Initially, the effect of the geometry is considered by optimizing the locations of a constant number of elements distributed over a constant aperture size. This facilitates a better understanding of the effect of element distribution on the broadband performance.

Next, a broadband antenna element is designed to allow for a more accurate full wave solution of small scaled optimized geometries where the effect of mutual coupling and beamforming can be assessed. The effect of the geometry is verified further by the measurement of a small hardware model. Finally, a number of

optimized geometries are proposed as a potential design for the square kilometre array low frequency, showing the cost and performance improvement.

Chapter3: Periodic Arrays

3.1 Introduction

A periodic array can be defined as an array whose elements arrangement repeats across the aperture. This chapter studies the performance of various periodic arrays highlighting their broadband limitations. It also shows how these geometries can be optimized in order to achieve a better broadband performance.

3.2 Square and Triangular Arrays

The arrays considered are shown in figure 3.1. Initially, an aperture diameter $D_{ap} = 100\lambda_H$ is defined. Then, a square grid is designed with an inter-element spacing that fills that aperture with 1000 elements shown in figure 3.1(a). This corresponds to inter-element spacing of $2.8\lambda_H$. Similarly, a grid of equilateral triangles is designed to fill the same aperture size with 1000 elements shown in figure 3.1(c). This corresponds to triangle side of $3\lambda_H$.

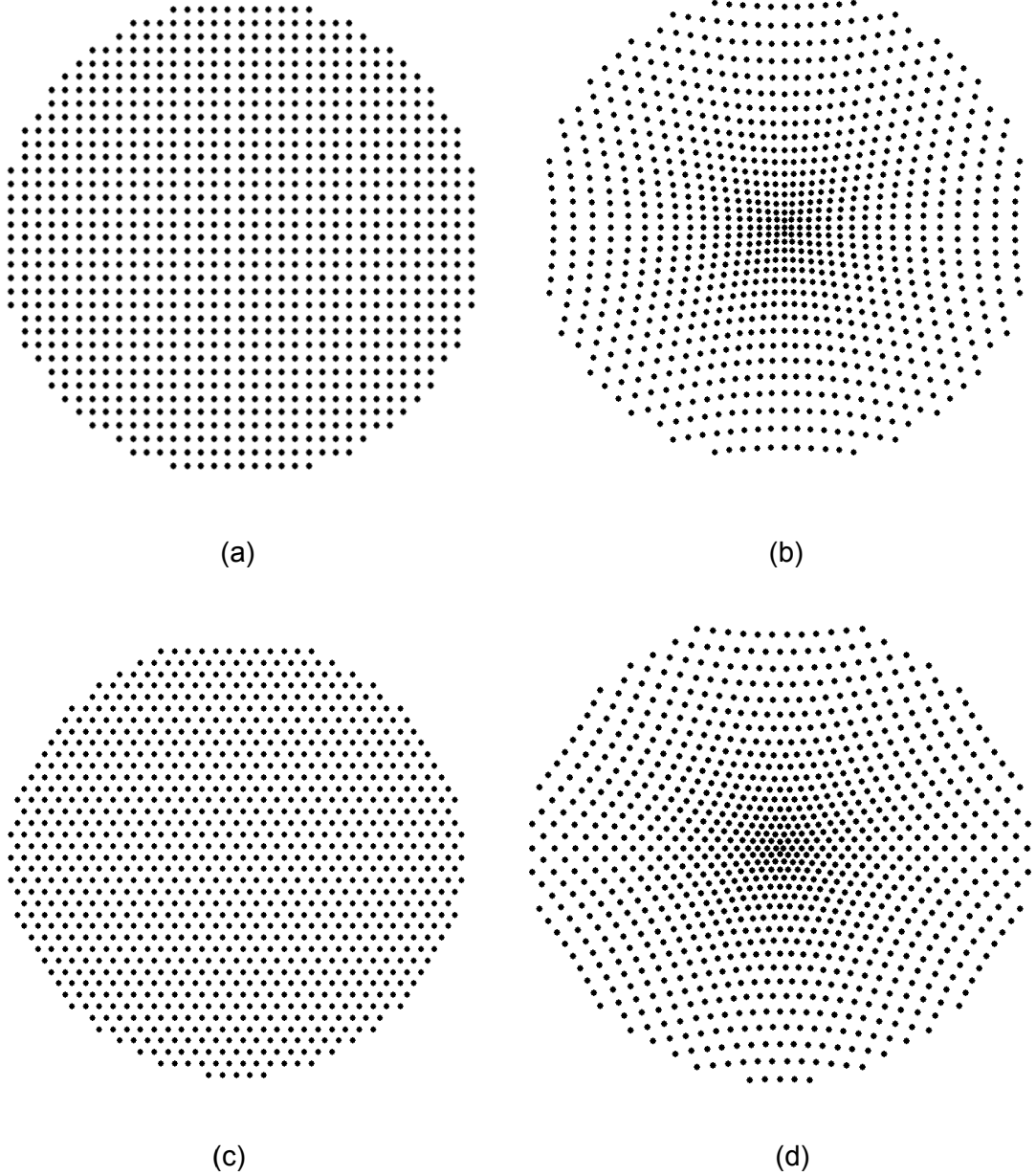


Figure 3.1: (a) Square Array, (b) Tapered Square Array, (c) Triangular Array, (d) Tapered Triangular Array.

Space tapering is applied on element positions in the square and triangular arrays to produce the arrays in figure 3.1(b) and 3.1(d) respectively. Various windows can be selected as the tapering function. The tapering function chosen for both arrays here as an example, is a Gaussian distribution with a standard deviation reciprocal . The value of the size window can be computed from

$$K[Q + 1] = e^{-\frac{1}{2} \left[\alpha \frac{Q - J/2}{J/2} \right]^2} \dots \dots \dots (3.1)$$

Where $0 \leq Q \leq J$ and $\alpha \geq 2$

The tapering is achieved by determining the distance of each element to the centre of the aperture and calculating the relative distance shift for that element. Therefore, elements closer to the centre will move more closely to the centre compared with elements at the edges. The array is then rescaled to the original aperture size. For the case studied here, the square tapered array now has a minimum separation $d_{min} = 1.6\lambda_H$ and a maximum separation $d_{max} = 3.8\lambda_H$. Following the same approach, the triangular tapered array has a minimum separation $d_{min} = 1.6\lambda_H$ and a maximum separation $d_{max} = 3.4\lambda_H$. It is important to note that all four arrays contain the same number of elements⁸ and have equivalent aperture sizes.

The array radiation patterns, directivity and side lobe performance is calculated over the specified band above. The details and formulas of how this is achieved is outlined in section 2.2

- **Directivity and side lobe performance**

The directivity and side lobe performance over a broadband are computed for the four arrays shown in the previous section. The operational bandwidth chosen is 20:1 where the frequency in the graphs is the ratio of any particular frequency to the start frequency f/f_L . The directivity performance is shown in figure 3.2 below.

⁸ Due to the periodicity and the nature of square and triangular grids, the equal diameter arrays do not contain exactly the same number of elements. In the above case, the square array contains 1005 elements whereas the triangular array contains 1001 elements. However, since the number of elements is large, this difference effect can be negligible.

For the square array of figure 3.1(a), the directivity rises to a maximum of 39 dB at frequency $f_{max} = 6.5f_L = 0.325f_H$. Since the inter-element spacing for the square array is $2.8\lambda_H$, this is equal to $2.8 * 0.325\lambda_{max} = 0.91\lambda_{max}$. The directivity then drops dramatically before oscillating around $N \times D$ at higher frequencies. Where, N is the number of elements and D is the directivity of the hemispherical element of 3dB. Similarly, for the triangular array in figure 3.1(c), a maximum directivity of 39.5 dB is achieved at frequency $f_{max} = 7f_L = 0.35f_H$ which corresponds to element spacing of $1.1\lambda_{max}$. The triangular array allows for slightly larger separation before the grating lobes appears in real space which then cause the directivity to drop. This larger separation results in a narrower main beam resulting in a slightly higher directivity. As the grating lobes appear, the directivity drops and oscillates around $N \times D$ at higher frequencies similar to the square array.

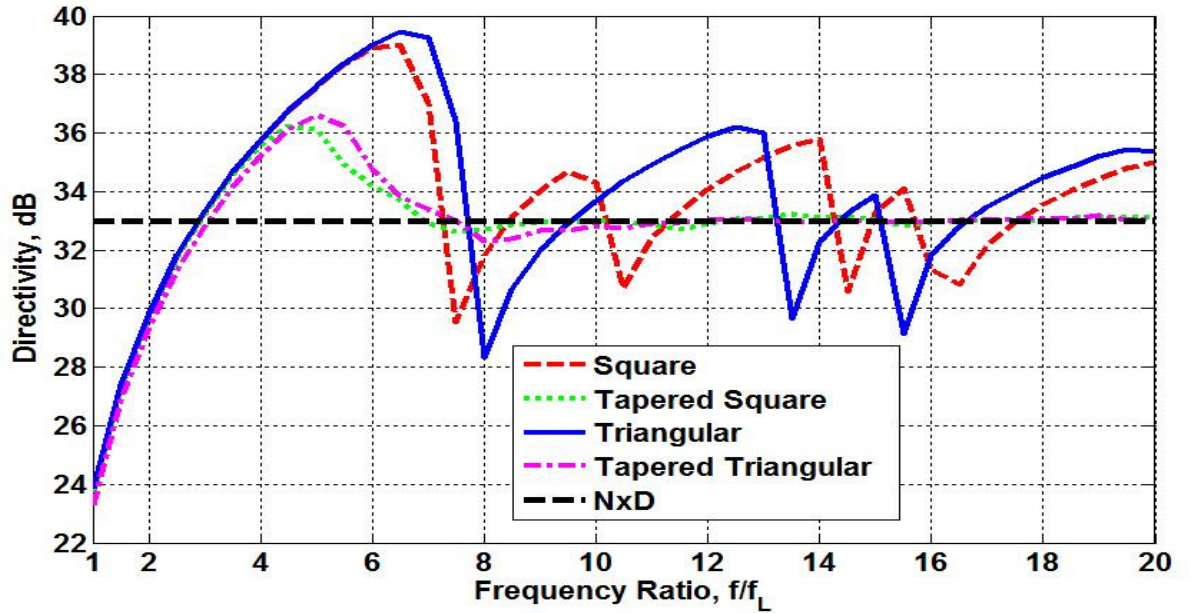


Figure 3.2: Directivity performance for periodic and tapered periodic arrays.

The effect of the periodicity is clearly seen from the directivity performance for the square and triangular arrays. While a high directivity is achieved over a narrow

band the directivity drops at regular intervals at higher frequencies. This is due to periodic formation of grating lobes sets appearing in the radiation pattern causing the directivity drop [3]. This can be understood further from the peak and mean side lobe comparisons in figure 3.3 and 3.4 respectively.

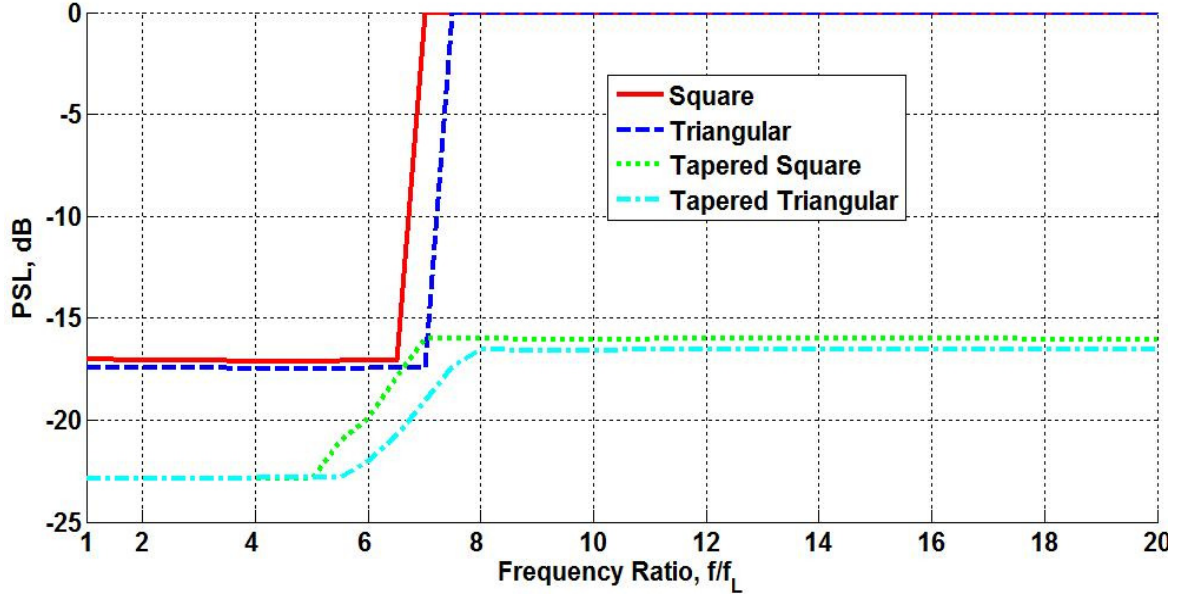


Figure 3.3: Peak side lobe performance for periodic and tapered periodic arrays.

For the square tapered array, the maximum achievable directivity has dropped to 36.2 dB compared to the un-tapered square array. In addition, the maximum achievable directivity occurs at slightly lower frequency and the corresponding minimum separation is now $0.4\lambda_{max}$. However, the directivity drops smoothly at higher frequencies converging towards $N \times D$. Similar performance is seen for the tapered triangular array where the maximum achievable directivity has dropped to 36.6 dB, corresponding to a minimum separation of $0.4\lambda_{max}$. The directivity also drops smoothly towards $N \times D$. The effect of steady directivity can be understood from the peak side lobe comparison in figure 3.3 where the peak side lobe is

maintained below -16 dB over the entire band for both tapered arrays. This indicates that no grating lobes have formed which would result in dramatic directivity drop, instead the grating lobes have been split into smaller side lobes over wider angular space. However, these side lobes continue to rise at higher frequencies causing the mean side lobe level increase in figure 3.4

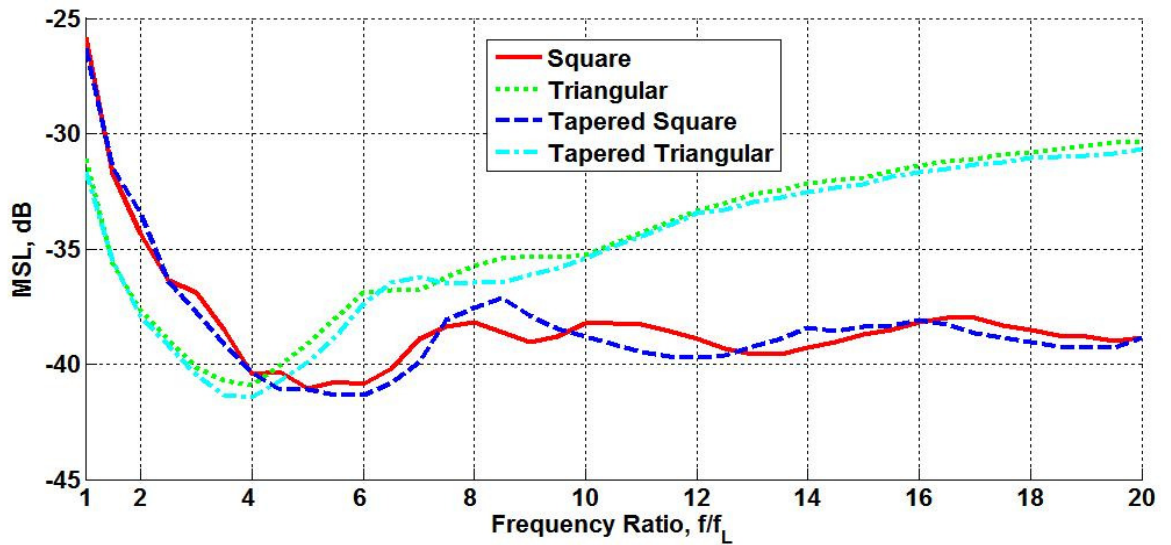


Figure 3.4: Mean side lobe performance for periodic and tapered periodic arrays.

- **Radiation Patterns**

It is useful to compare the resultant array radiation patterns in order to further understand the directivity and side lobe performance, in addition to comparing the pattern shapes. For all configurations discussed in this chapter and chapter 4, radiation patterns at two frequencies are shown. The first frequency is that at which the array achieves its maximum achievable directivity. The second frequency is the highest frequency in the band. The value of the maximum achievable directivity, peak and mean side lobe levels, in addition to the minimum, maximum and average separation are also shown on the relative figures for each array configurations.

Maximum Achievable Directivity

The radiation pattern of each array in figure 3.1(a, b, c & d) at the frequency of their maximum achievable directivity are shown in figure 3.5(a, b, c & d) respectively. A narrower main beam is observed in the case of square and triangular arrays than their tapered counterparts as expected. This explains the higher maximum directivity achieved by the square and triangular arrays. However, the tapered arrays show lower peak side lobes near the main beam. The effect of space tapering of element positions has in effect redirected power to produce a broader main beam and lower peak side lobes. Moreover, for all arrays, one can observe higher side lobes beginning to form at angles far from the main beam.

Highest frequency

As the frequency is increased higher side lobes appear in the radiation pattern which cause directivity drop. Figure 3.6 shows the radiation patterns of the different arrays at the highest frequency. At this frequency, the higher side lobes have fully formed and dominated the radiation patterns. In the case of rectangular and triangular arrays, these higher side lobes come in the form of repeating sets of grating lobes, causing the directivity to drop with the appearance of a new set, resulting in the oscillating directivity performance in figure 3.2. However, for the tapered arrays, the grating lobes have been fragmented into many relatively lower side lobes that increase gradually covering wider angular space as the frequency is increased.

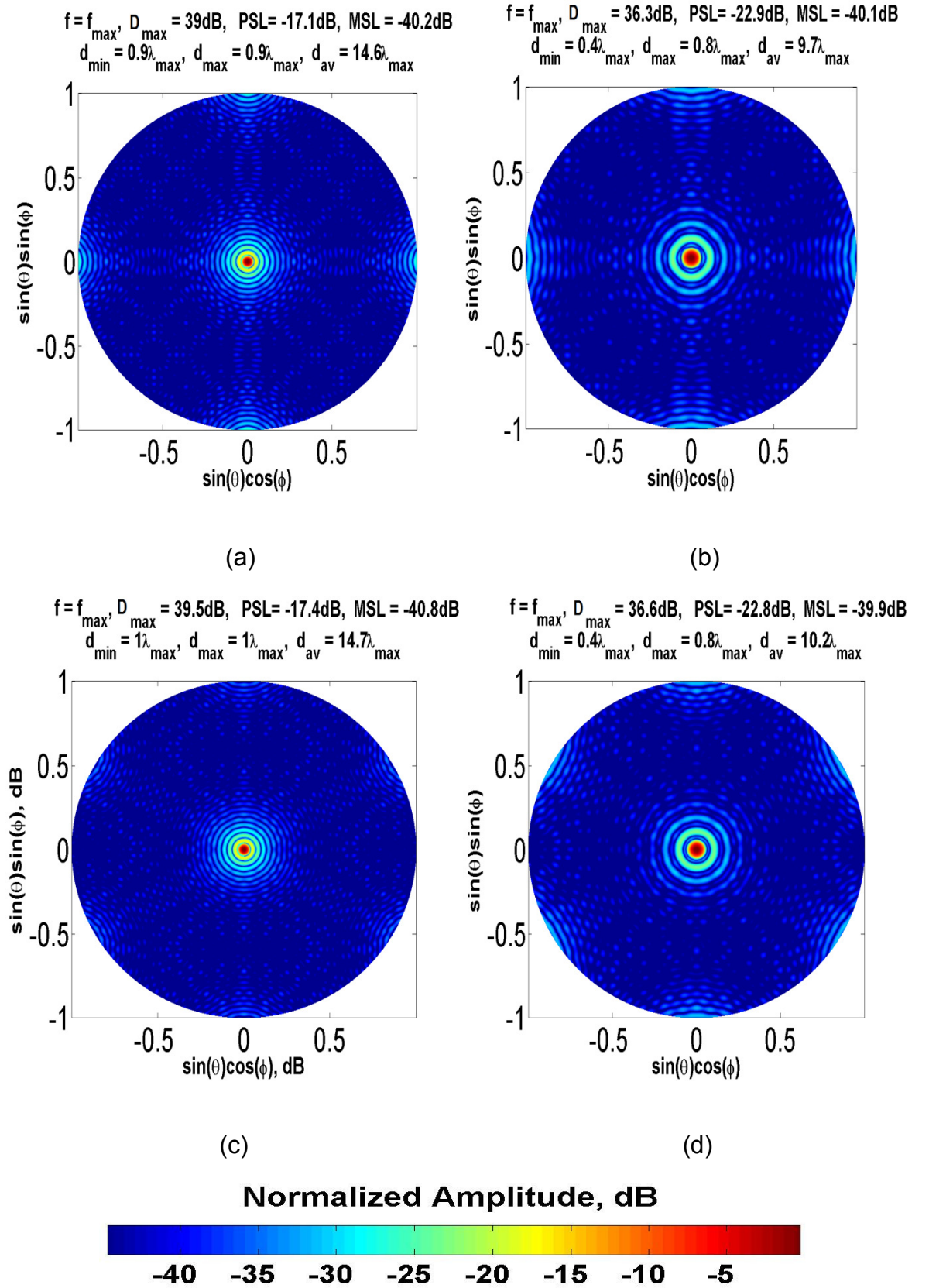


Figure 3.5: Radiation patterns at frequencies of maximum achievable directivity for (a) Square, (b) Tapered Square, (c) Triangular and (d) Tapered Triangular arrays

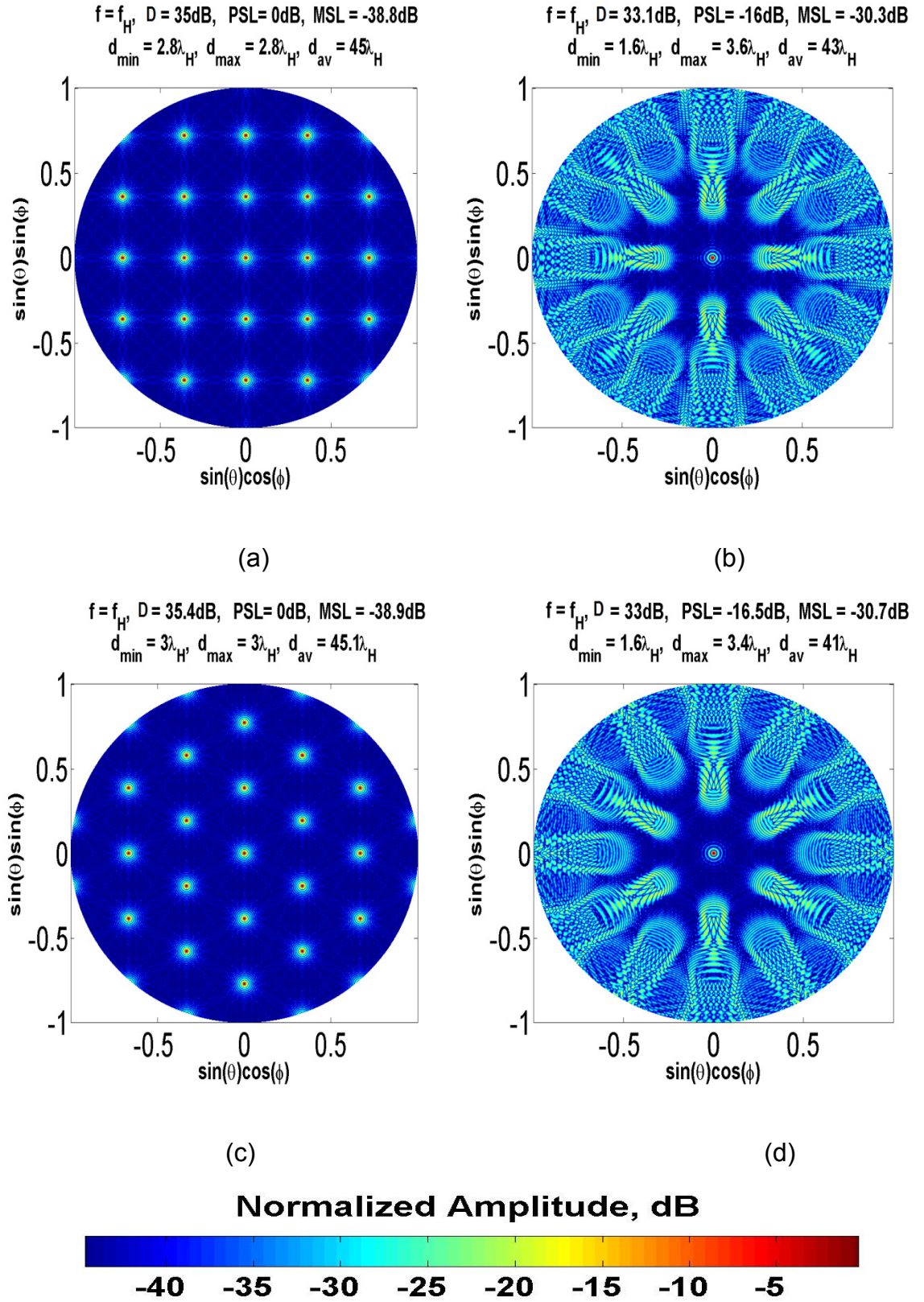


Figure 3.6: Radiation pattern at highest frequency for (a) Square, (b) Tapered Square, (c) Triangular and (d) Tapered Triangular arrays

3.3 Concentric Rings Array

A concentric rings array can be constructed by locating N_r elements on circular rings that have a common centre and varying radii R_r [67]. Where N_r and R_r indicate the number of elements and the radius of the r^{th} ring respectively. For a uniform concentric ring array the rings radii increase uniformly and the number of elements on each ring can be calculated from its radius from:

$$N_r = 2\pi R_r \dots \dots \dots (3.2)$$

If N_r is a fraction, it can be rounded down to the nearest integer. The Cartesian coordinates of elements on each ring can now be computed from

$$X_{N_r} = R_r \cos(\psi_{N_r}) \dots \dots \dots (3.3)$$

$$Y_{N_r} = R_r \sin(\psi_{N_r}) \dots \dots \dots (3.4)$$

Where ψ

$$\psi_{N_r} = \frac{2\pi R_r n}{N_r}, n = 0, 1, 2, \dots, N_r - 1 \dots \dots \dots (3.5)$$

A uniform concentric ring array of 18 rings and 1065 elements is shown in figure 3.7(a). The array is designed to have a diameter of $100\lambda_H$ and the corresponding minimum separation is $2.8\lambda_H$

In the previous section the effect of space tapering according to a Gaussian distribution was studied on square and triangular arrays. The same technique can be applied to uniform concentric rings arrays. In this section, a similar technique is chosen in addition to another technique based on randomization to improve the broadband performance of the concentric rings array.

The first technique is by letting the ring radii increase exponentially. This causes the rings to be relatively closer to each other in the middle and more spaced at the edges. The array in figure 3.7(b) shows a concentric ring array with exponential tapering of power 1.3. Since the array is denser in the middle, the minimum separation is now $2.8\lambda_H$

The second technique is randomization. The position randomization can be achieved by introducing a small random error in the element positions. The maximum range of the error can be limited as not to exceed a certain percentage of the minimum separation in the uniform concentric rings array. Figure 3.7(b) shows a randomized concentric rings array where the randomization error is less than 50% of the minimum separation of the uniform concentric rings. Similar to the previous section, all three arrays contain the same number of elements and have the same aperture diameter of $100\lambda_H$.

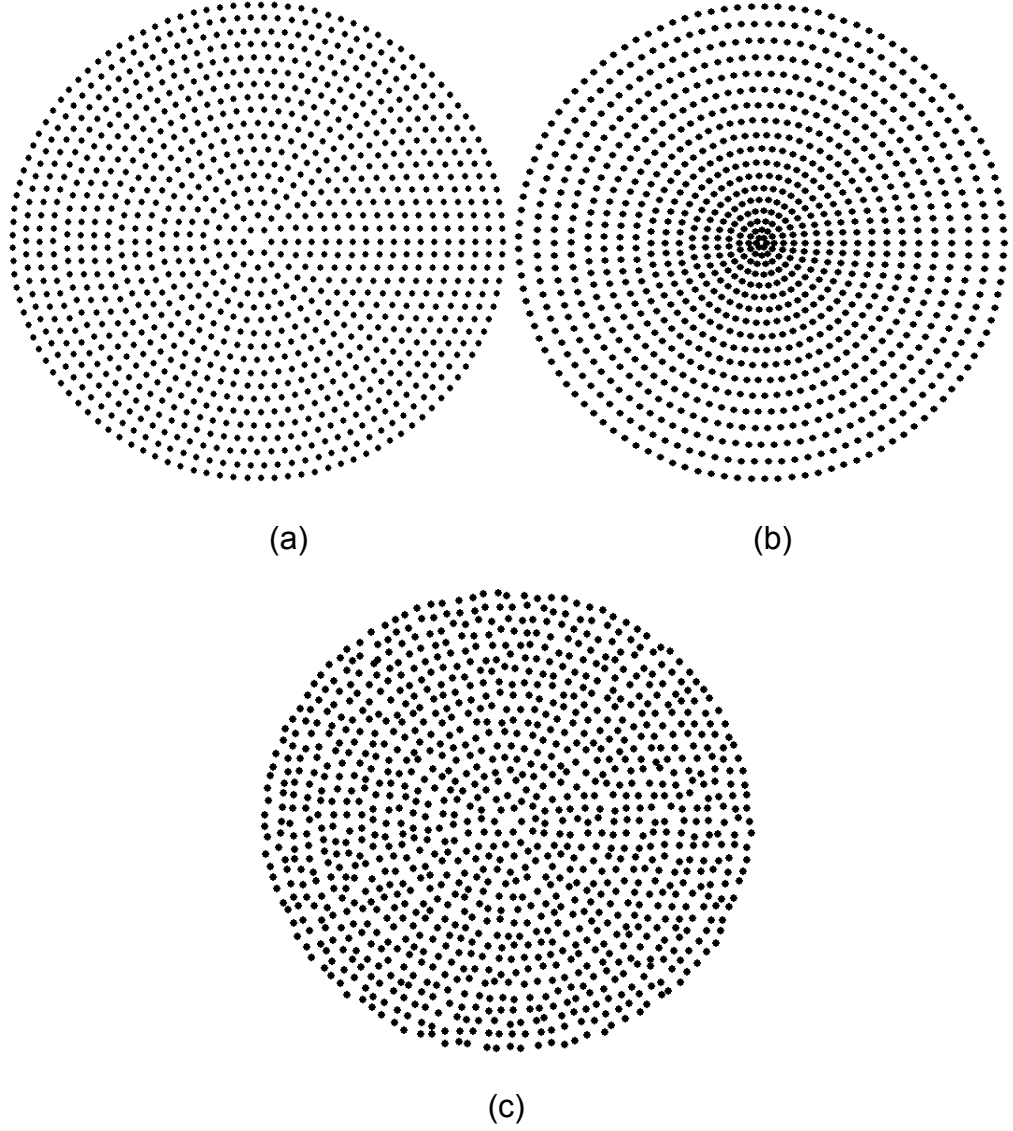


Figure 3.7: (a) Uniform Concentric Rings, (b) Tapered Concentric Rings, (c) Randomized Concentric Rings array.

- **Directivity and Side lobe Performance**

Similar to the periodic arrays in section 3.2 the directivity and side lobes for the three concentric rings arrays are calculated. The directivity performance of the concentric ring arrays in figure 3.7 are plotted in figure 3.9. For the uniform concentric rings array, the directivity rises to a maximum of 39.5 dB at frequency f_{max} that is when the minimum separation in the array is $0.9\lambda_{max}$. The directivity then drops sharply oscillating around $N \times D$. The directivity drop is due

to higher side lobes shown in figure 3.10. The directivity oscillation can be explained by the side lobe level rising as a staircase at higher frequencies where the directivity drops at each new rise. The directivity performance of a uniform concentric rings array is similar to that of the periodic square and triangular arrays studied in section 3.1 where a sharp increase in side lobe level occurs at the frequency where the array becomes under-sampled (that is the minimum separation is larger than one wavelength). However, the high side lobes formed are not full grating lobes. This is due to the geometry being periodic in terms of ring positions and not in terms of element distribution. That is the element distribution in any one plane is not periodic. Therefore, the grating lobes cannot fully form, and appear as side lobes that stay below the main beam level, even at higher frequencies.

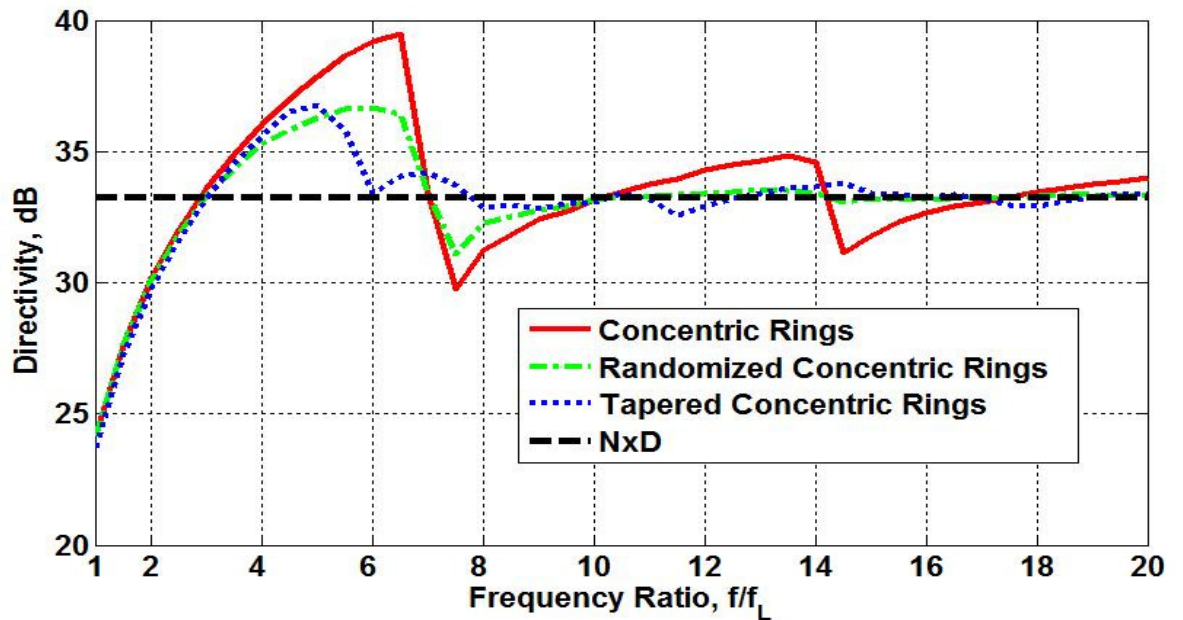


Figure 3.8: Directivity performance for uniform, randomized and tapered concentric rings array.

In the case of randomized concentric rings array, the maximum directivity has dropped to 36.7 dB at a minimum separation of $0.4\lambda_{max}$. However, as the frequency is increased the directivity drops slightly below $N \times D$ before converging towards $N \times D$ with no oscillation. The directivity drop is due to the rise of high side lobe levels that remain at a maximum of -13.7 dB at higher frequencies. The effect of the randomization eliminated the periodicity in the geometry as in the uniform concentric rings array. This reduced the peak side lobe level and stabilized the directivity performance of the higher frequencies. However, figure 3.11 shows the continuous rise in the randomized concentric rings array mean side lobe at higher frequencies compared to the uniform concentric rings array.

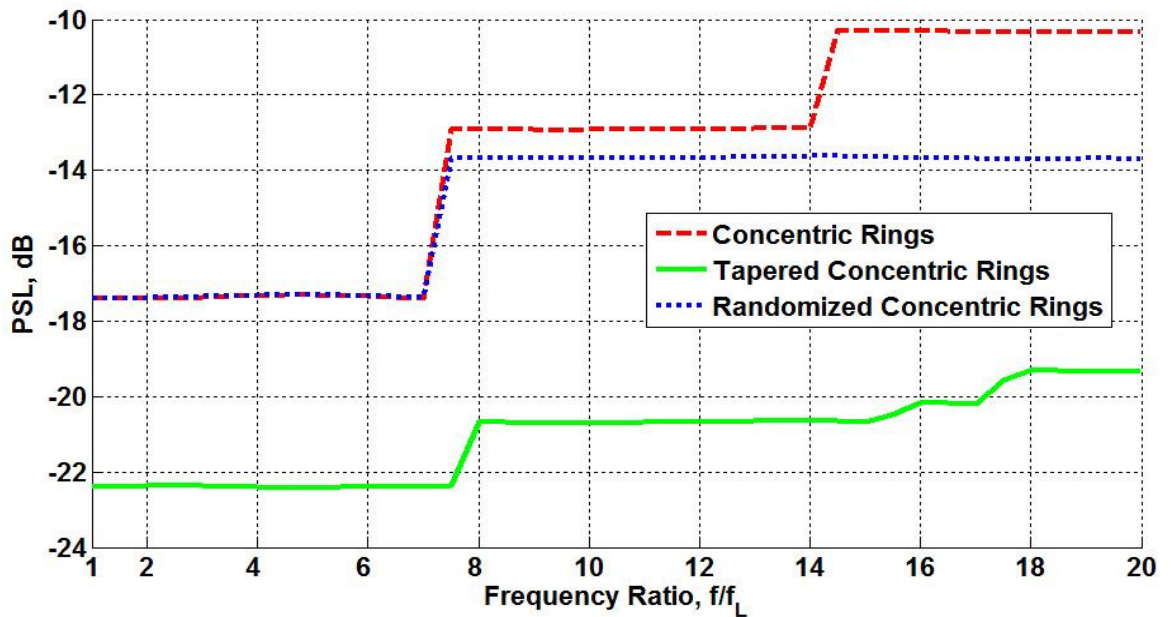


Figure 3.9: Peak side lobe performance for uniform, randomized and tapered concentric rings array.

For the tapered concentric rings array, the peak side lobe level is below -19.3 dB and a much lower mean side lobe is achieved in figure 3.9 and 3.10 respectively.

In addition, the maximum directivity is approximately the same value as the maximum directivity of the randomized concentric rings array.

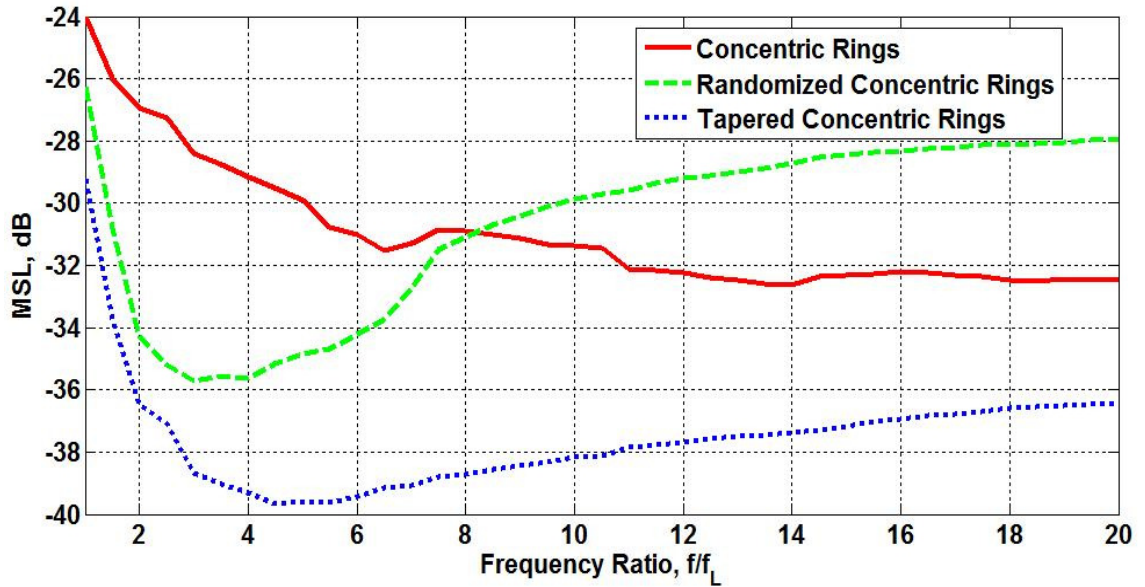


Figure 3.10: Mean side lobe performance for uniform, randomized and tapered concentric rings array.

- **Radiation Patterns**

Similar to the arrays in section 3.2 the radiation patterns of the uniform randomized and tapered concentric rings arrays are considered at the frequencies of maximum achievable directivity and the highest frequency in the band.

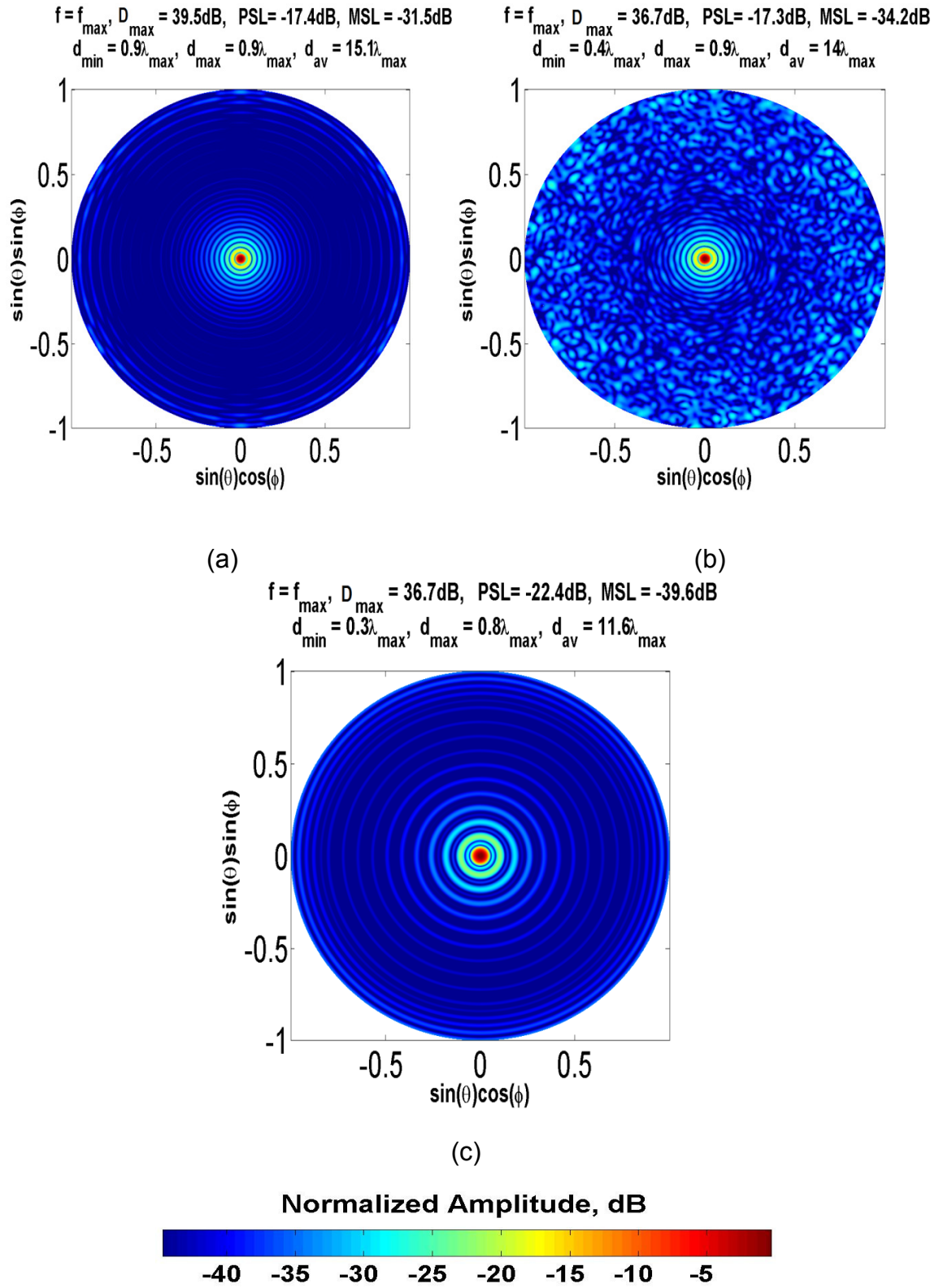


Figure 3.11: Radiation patterns at frequencies of maximum achievable directivity for (a) Uniform, (b) Randomized, and (c) Tapered Concentric Rings arrays

Maximum achievable Directivity

The radiation pattern in figure 3.11(a) for the uniform concentric rings array shows a narrow main beam and low side lobes far from the main beam which gives its high maximum achievable directivity. In the case of the randomized concentric rings array, the cause of the directivity drop can be understood from its radiation pattern in figure 3.11(b) where high side lobes appear over large angular space. For the tapered concentric rings array, the radiation pattern in figure 3.11(c) shows much lower peak and mean side lobes achieved at the expense of reducing the maximum achievable directivity.

Highest Frequency

The radiation patterns at the highest frequency f_H for different concentric rings array are shown in figure 3.13(a, b & c). For the uniform concentric rings, the side lobe region contains higher side lobes that are self replicating as the frequency is increased which explains the oscillating directivity behaviour at higher frequencies. In the randomized case, the side lobe region has been averaged over all space except for some peaks which caused the sharp directivity drop in figure 3.8. A smoother side lobe region is seen in the case of the tapered concentric rings array which is associated with its more stable directivity performance in figure 3.8.

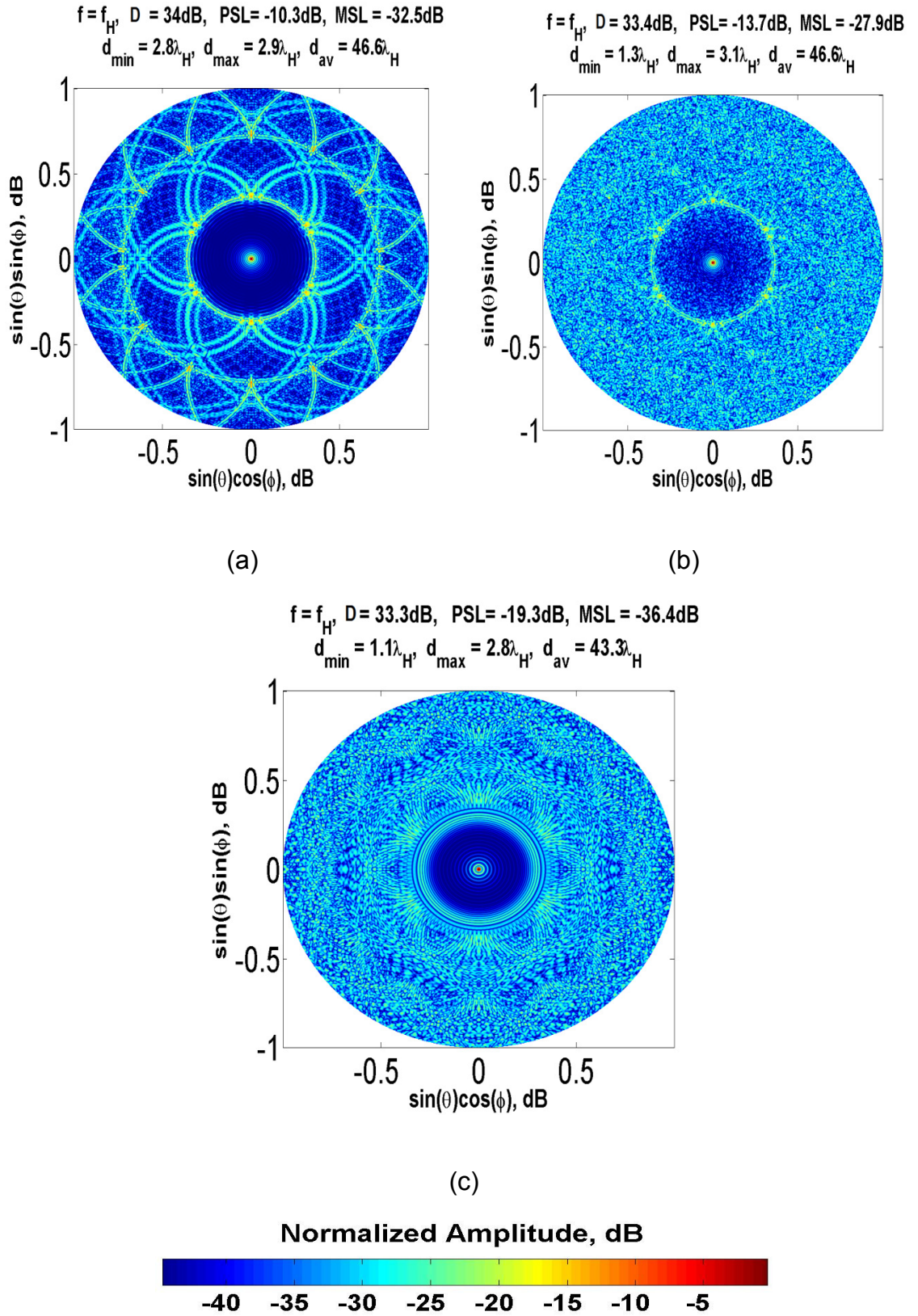


Figure 3.12: Radiation Pattern at the highest frequency for (a) Uniform, (b) Randomized, and (c) Tapered Concentric Rings arrays

3.4 Chapter Summary

This chapter considered the broadband performance and optimization of square, triangular, and concentric rings periodic arrays. The main advantage of periodic arrays is the ability to achieve high maximum directivity and low side lobes for relatively broad bandwidths when well sampled. However, at higher frequencies, the under-sampling causes peaks in the side lobe region which might be as high as the main beam (grating lobes), such as in the square and triangular arrays. Therefore, the broadband performance of periodic arrays is limited by two factors:

- 1- The formation of grating lobes which limits the highest operational frequency⁹ taking into consideration scanning requirements (more on scanning in section 6.2).
- 2- The inter-element spacing constraining the maximum element size which subsequently determines the lowest operational frequency

Moreover, from a cost versus directivity perspective, periodic array can achieve more directivity than $N \times D$ over a maximum bandwidth of one octave (Not including any scan requirements). More bandwidth can only be acquired at lower frequency making the array redundant in terms of number of elements and hence cost inefficient.

Optimization of periodic arrays can be achieved by changing the element positions as to break the periodicity in the geometry, preventing radiation from individual elements to add in phase and causing high side lobe peaks at higher frequencies

⁹ For some applications where the signals from all elements are correlated, the unwanted signals received by grating lobes can be eliminated reducing the bandwidth limitation. However, since correlation demands higher signal processing which increases the cost, beamforming arrays are often favoured especially for large arrays.

thus extending the operational bandwidth. However, breaking the periodicity also reduces the maximum achievable directivity of the array.

The tapered array performance shows how the breaking of periodicity reduces the maximum achievable directivity but prevents the formation of grating lobes at higher frequencies. This can also be achieved by randomization. Even though this comes at the expense of sacrificing maximum achievable directivity, the directivity can be maintained above $N \times D$ for many octaves while side lobe level can be kept reasonably under control. These techniques results in different directivity and side lobe profiles over the bandwidth depending on the initial geometry.

Chapter 4: Aperiodic Arrays

4.1 Introduction

Aperiodic arrays refer to arrays whose element distribution does not repeat across the aperture. Examples are random arrays, and certain types of fractal and spiral arrays. From chapter three, the optimization of periodic arrays for broadband performance results in aperiodic arrays and in this chapter we consider the broadband design and optimization of random and spiral aperiodic arrays.

4.2 Random Arrays

4.2.1 Minimum separation constraint random array

A random array can be constructed by defining an aperture size and distribute the elements randomly within that aperture. Similar to arrays in chapter 3, an aperture diameter of $100\lambda_H$ is defined which is allowed to contain 1000 elements. The elements are then distributed randomly across the aperture with a predefined minimum separation constraint.

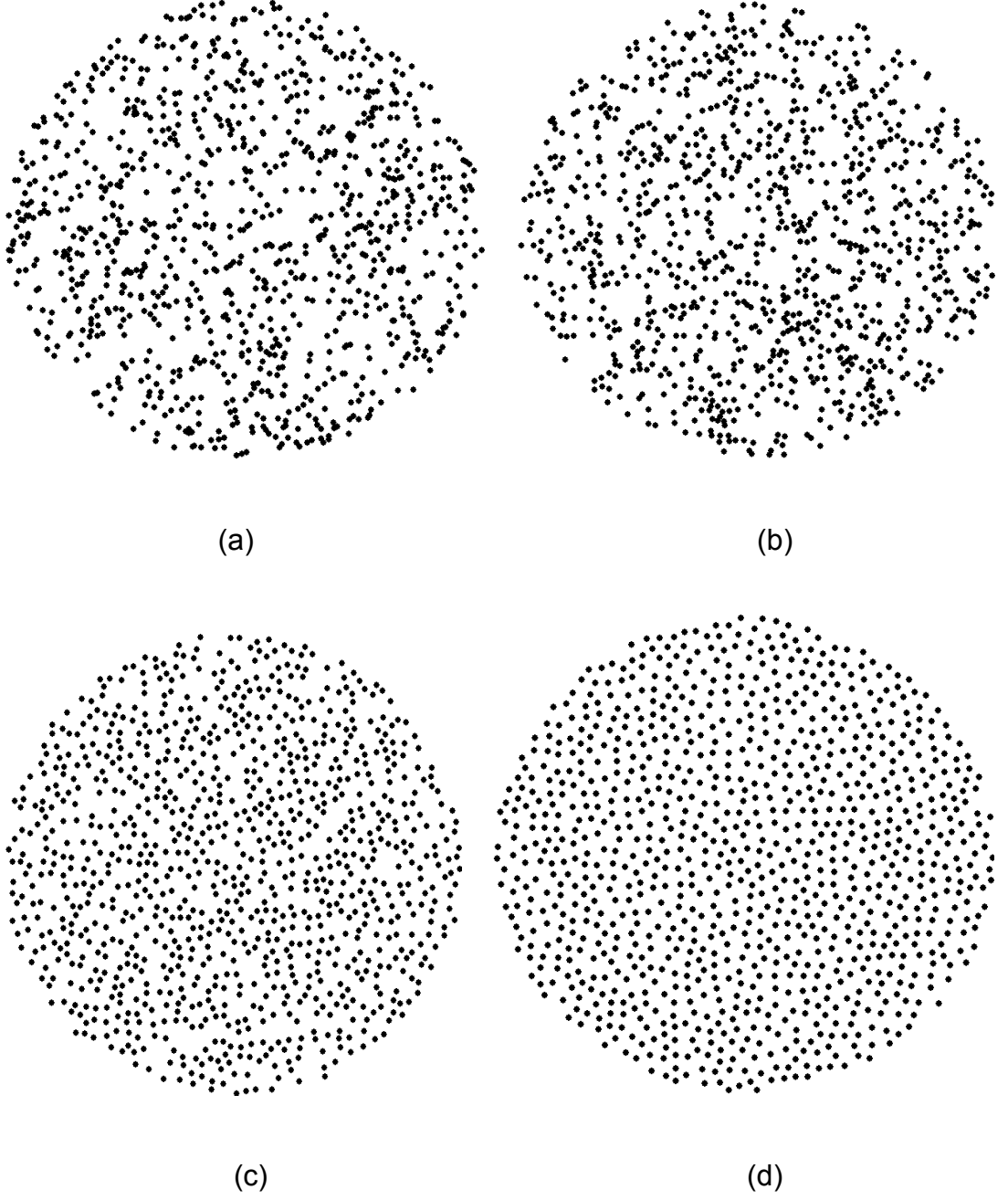


Figure 4.1: Random arrays with different minimum separation (a) $d_{min} = 0.3\lambda_H$,

(b) $d_{min} = 0.8\lambda_H$, (c) $d_{min} = 1.7\lambda_H$, (d) $d_{min} = 2.3\lambda_H$

Four arrays with different minimum separations are designed for comparison shown in figure 4.1. Due to the fixed aperture array and number of elements, there is a limit to the maximum minimum separation that can be enforced between the elements. With a reasonable computational time, the largest minimum separation constraint that can be achieved for this particular case is $2.3\lambda_H$ in figure 4.1(d).

- **Directivity and side lobe performance**

The directivity and side lobe performance of the different random arrays designed in the previous section are compared over a (1:20) band for hemispherical array elements similar to the arrays in chapter 3.

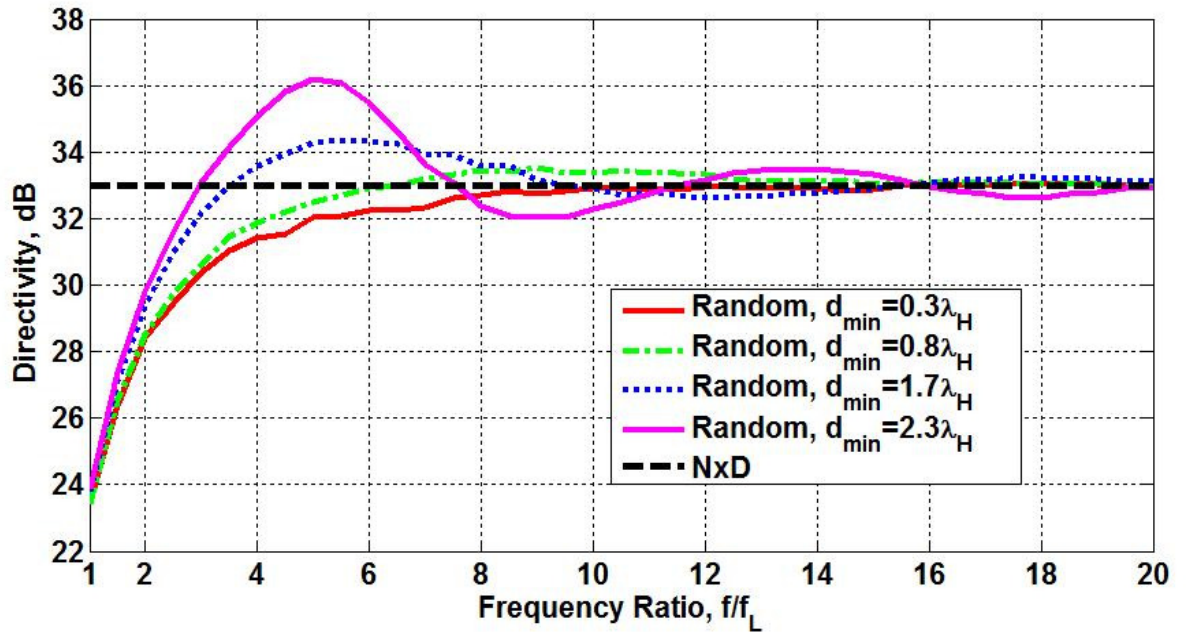


Figure 4.2: Directivity performances for random arrays with different minimum separations.

The effect of the minimum separation on the array directivity can be seen in figure 4.2 where the largest maximum achievable directivity is obtained by the array with the largest minimum separation. However, its directivity drops more sharply and oscillates more around $N \times D$ at higher frequencies than arrays with smaller minimum separations.

The directivity performance can be understood by examining the element distributions for the different arrays in figure 4.1 where a larger minimum separation ensures a more even distribution across the aperture and avoids the

formation of the dense clusters of elements and subsequently the empty regions seen in arrays with a smaller minimum separation. The dense regions reduce the elements contribution to the directivity since they are too close in terms of wavelength. Moreover, the associated empty region increase the under-sampling and cause higher side lobes as can be seen from the peak and average side lobes comparison in figures 4.3 and 4.4 respectively.

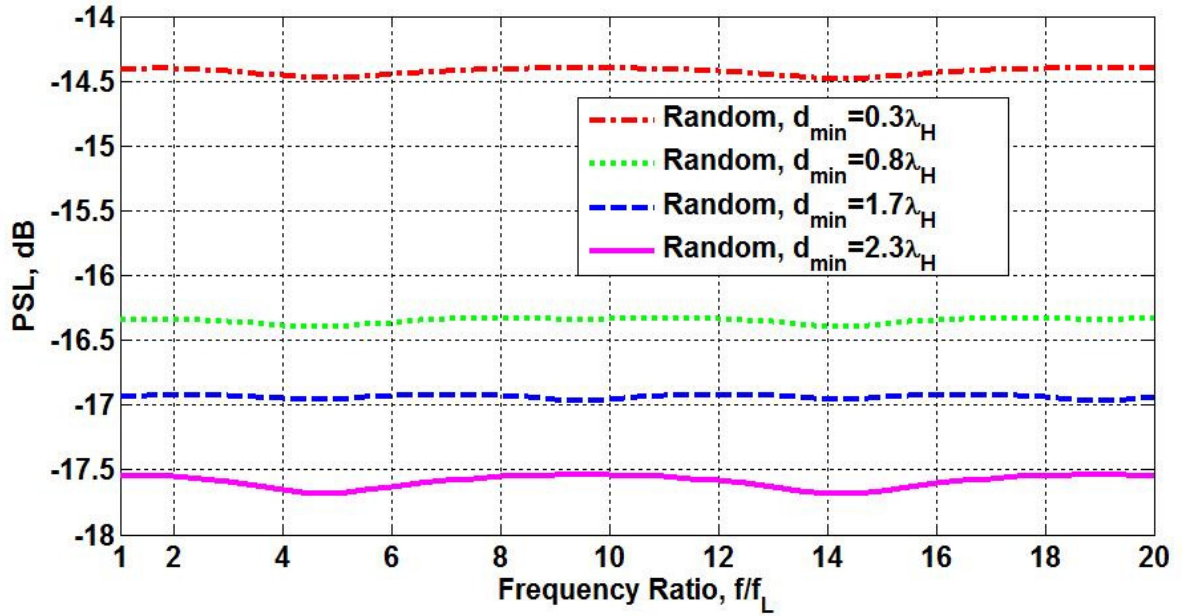


Figure 4.3: Peak sidelobe performance for random arrays with different minimum separations.

The peak sidelobes are maintained approximately constant over the entire band for all arrays, with the minimum peak sidelobe achieved by the array with the largest minimum separation which also achieves the lowest mean sidelobes. However, the larger minimum separation forces the elements to be nearly equally separated creating some form of periodicity which results in the slight directivity oscillation at higher frequencies.

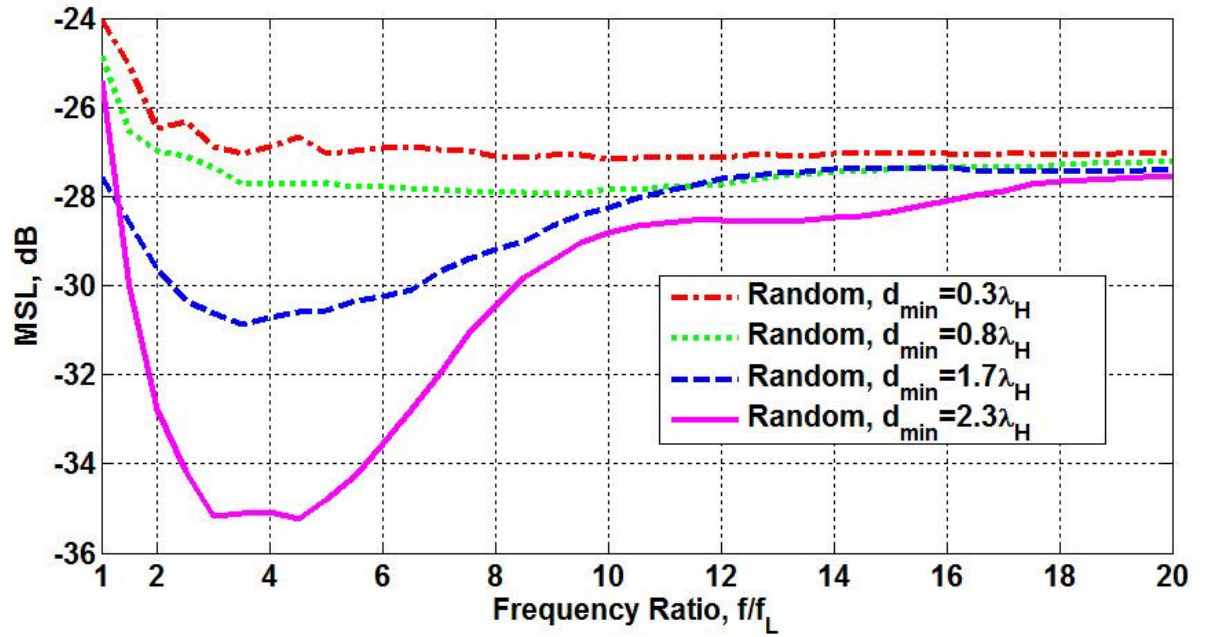


Figure 4.4: Mean sidelobe performance for random arrays with different minimum separations.

- **Radiation Patterns**

Similar to the arrays discussed in chapter 3, the radiation patterns for the random arrays are considered at the frequencies of the maximum achievable directivity, in addition to the highest frequency in the band:

Maximum achievable directivity

The radiation patterns for the different random arrays at the frequencies of their maximum achievable directivity are shown in figure 4.5. One can observe the lower side lobes in the radiation pattern of the array with the largest minimum separation compared to the radiation pattern of arrays with smaller minimum separation where high sidelobes dominate the radiation pattern.

It is noted that the array with the largest minimum separation achieves its maximum directivity when the maximum element separation is equal to $0.9\lambda_{max}$ comparable to the performance of the square array in chapter 3.

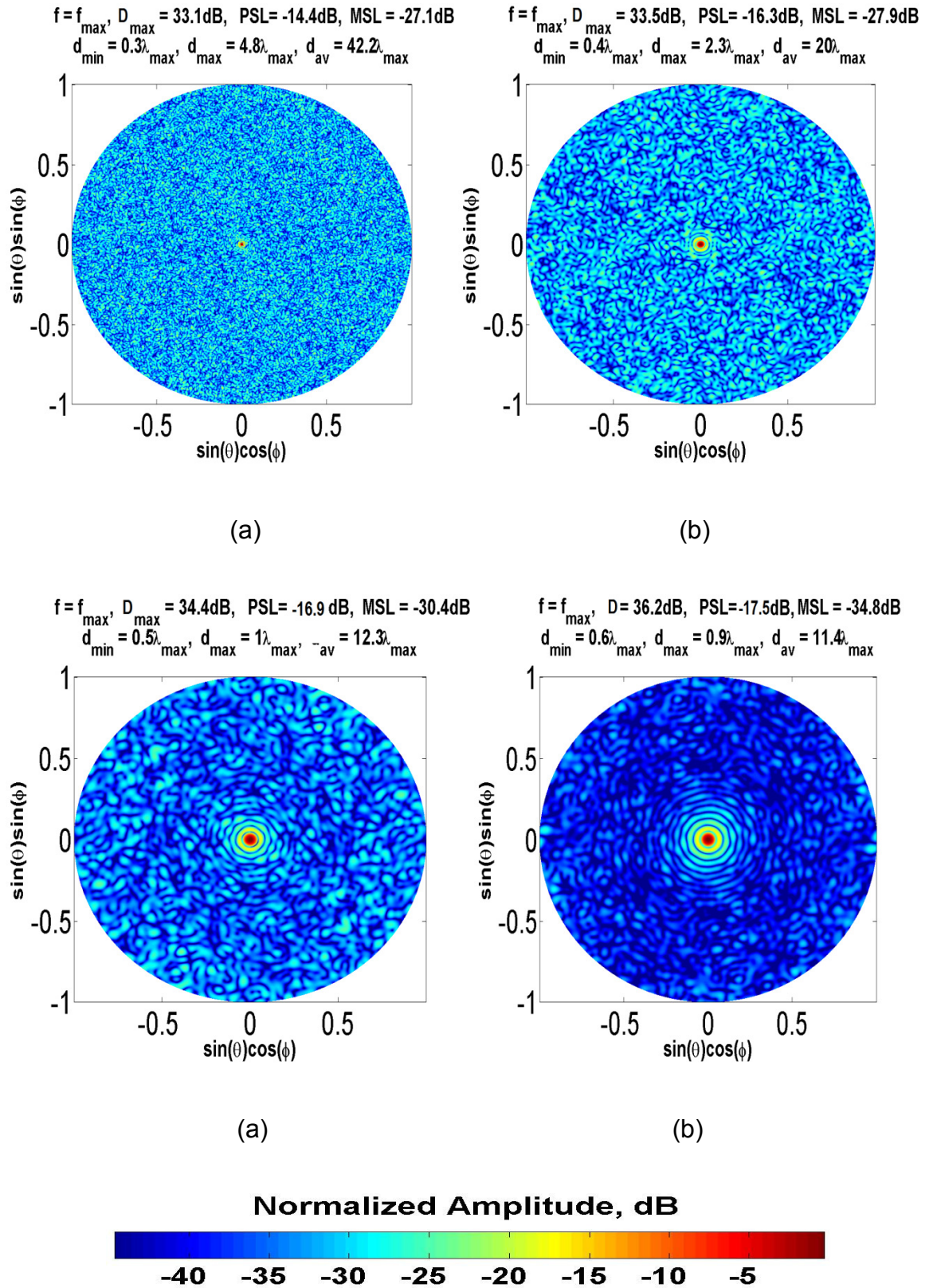


Figure 4.5: Radiation patterns at frequencies of maximum achievable directivity random arrays, (a) $d_{\min} = 0.3\lambda_H$, (b) $d_{\min} = 0.8\lambda_H$, (c) $d_{\min} = 1.7\lambda_H$, (d) $d_{\min} = 2.3\lambda_H$

Highest frequency

The radiation patterns for the random arrays at the highest frequency are shown in figure 4.6 where the arrays are largely sparse in terms of wavelength with high side lobes dominating the radiation pattern and the achieved directivity is approximately equal to $N \times D$. However, for the array with the largest minimum separation in figure 4.6(d), a lower side lobe region can be observed near the main beam as high side lobe levels begin to form at angles far away from the main beam, progressively moving to closer to the main beam as the frequency is increased.

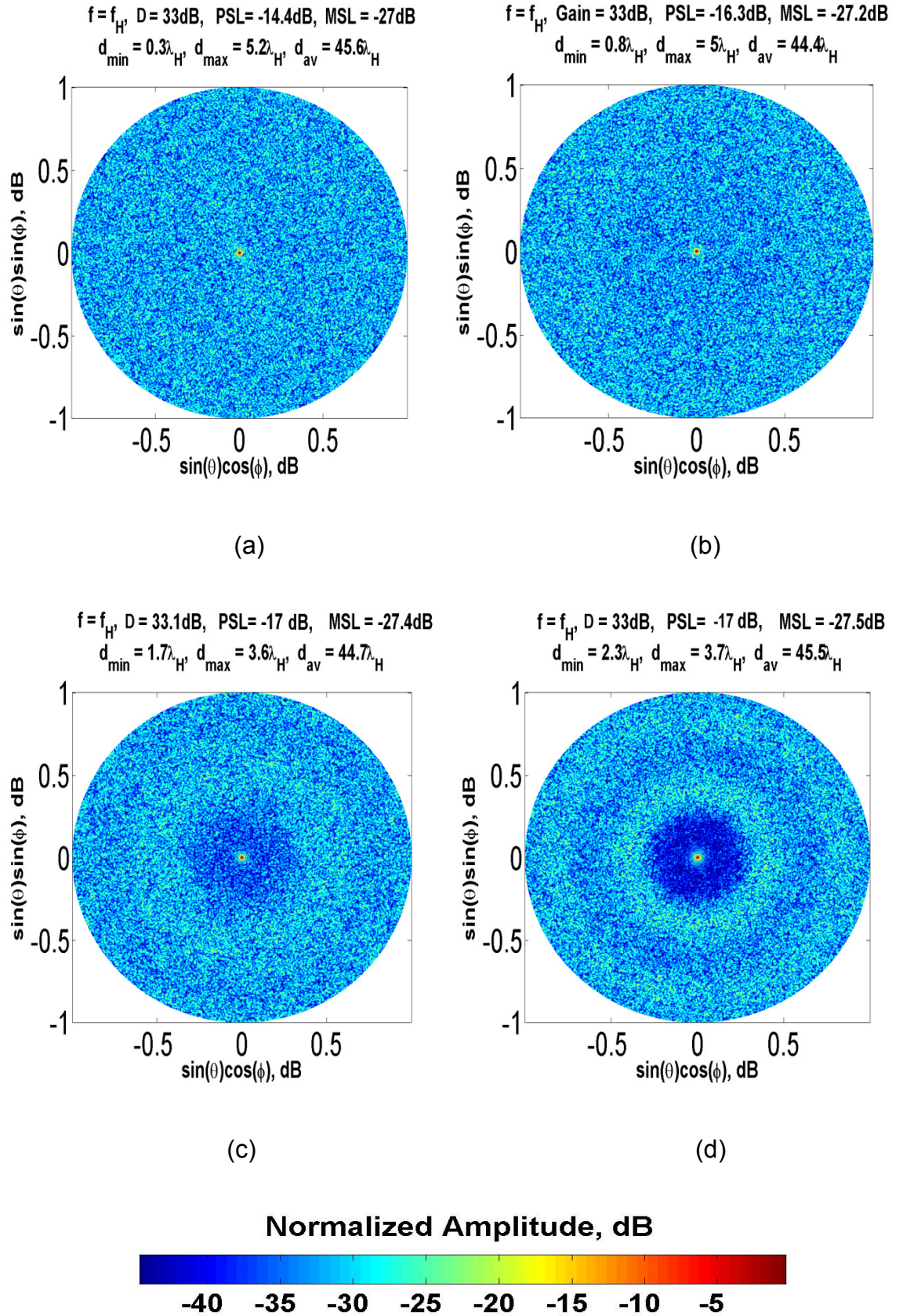


Figure 4.6: Radiation Patterns at the highest frequency for random arrays, (a) $d_{\min} = 0.3\lambda_H$, (b) $d_{\min} = 0.8\lambda_H$, (c) $d_{\min} = 1.7\lambda_H$, (d) $d_{\min} = 2.3\lambda_H$

4.2.2 Tapered Random Array

A large minimum separation constraint applied to random arrays has been seen to increase the maximum achievable directivity at a single frequency and reduce the sidelobes over the band. However, a random array designed for maximum achievable directivity criterion results in an oscillating directivity at higher frequencies decreasing below $N \times D$ over certain parts of the frequency band. In addition, the peak side lobe cannot be decreased below -17dB at any part of the band using this kind of design. The benefits of space tapering applied to reduce sidelobe level in periodic arrays are utilized here for optimizing the directivity and sidelobe performance of random arrays. The same Gaussian window used in section 3.1.1 for the tapered square and triangular arrays is used with the random array with largest minimum separation in figure 4.1(d) to design the array in figure 4.7. The array now is denser in the centre compared to the edges, and the minimum separation has decreased to $1.25\lambda_H$.

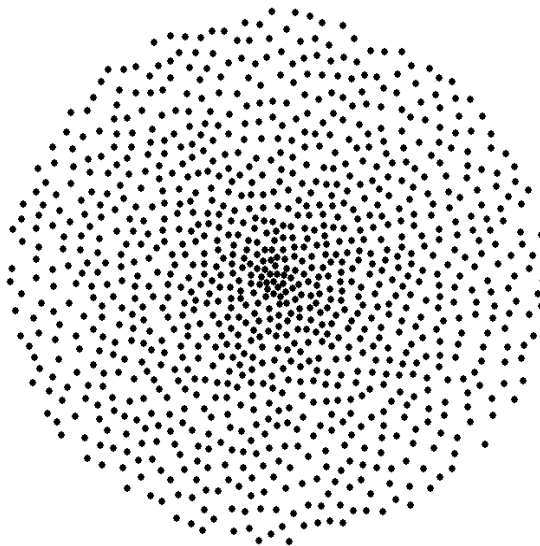


Figure: 4.7 Tapered random array

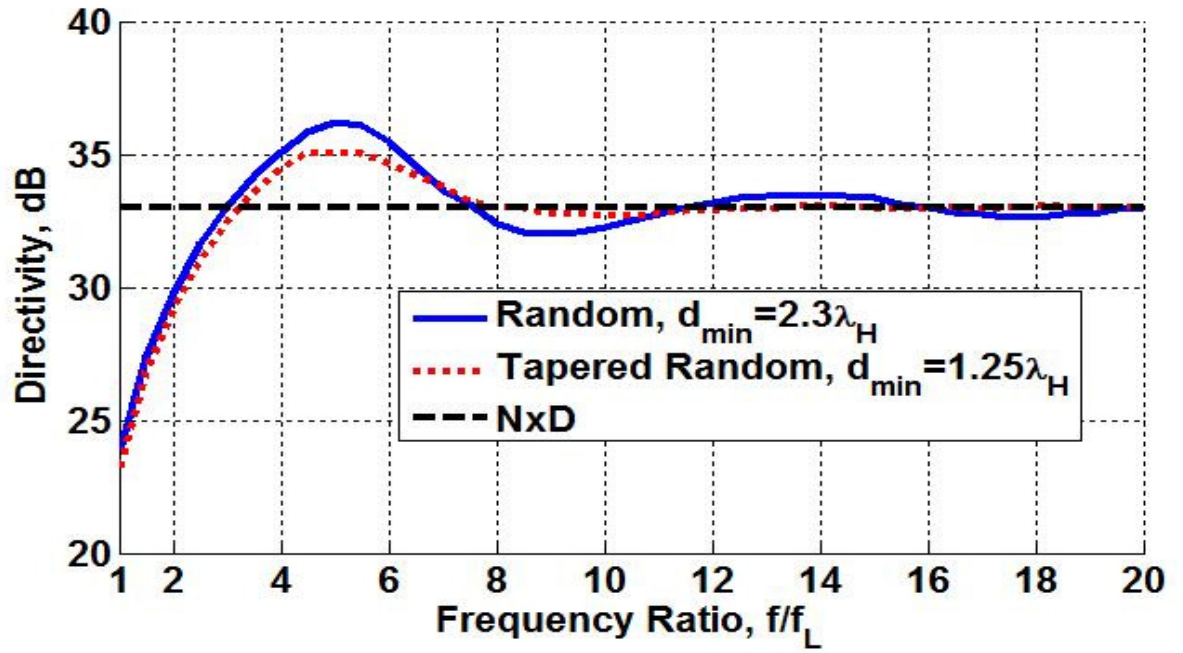


Figure 4.8: Directivity performance of tapered and un-tapered random arrays

The directivity and side lobe performance of the tapered random array are compared to the directivity and sidelobes of the un-tapered array in figures (4.8-4.10). The tapered array achieves less maximum achievable directivity than the un-tapered array (1 dB in this particular tapering). For the tapered array, the directivity drops more smoothly as the frequency is increased and oscillates less around $N \times D$ at higher frequencies. Furthermore, the peak sidelobe achieved has reduced over the band by a maximum of 1.5 dB, while maintaining the same mean sidelobe level as the un-tapered array. The results show that lower peak side lobes can be traded off with maximum directivity by applying space tapering. Lower sidelobes can be achieved by applying a selecting a narrower tapering window. The expense is a lower directivity in addition to closer minimum separation.

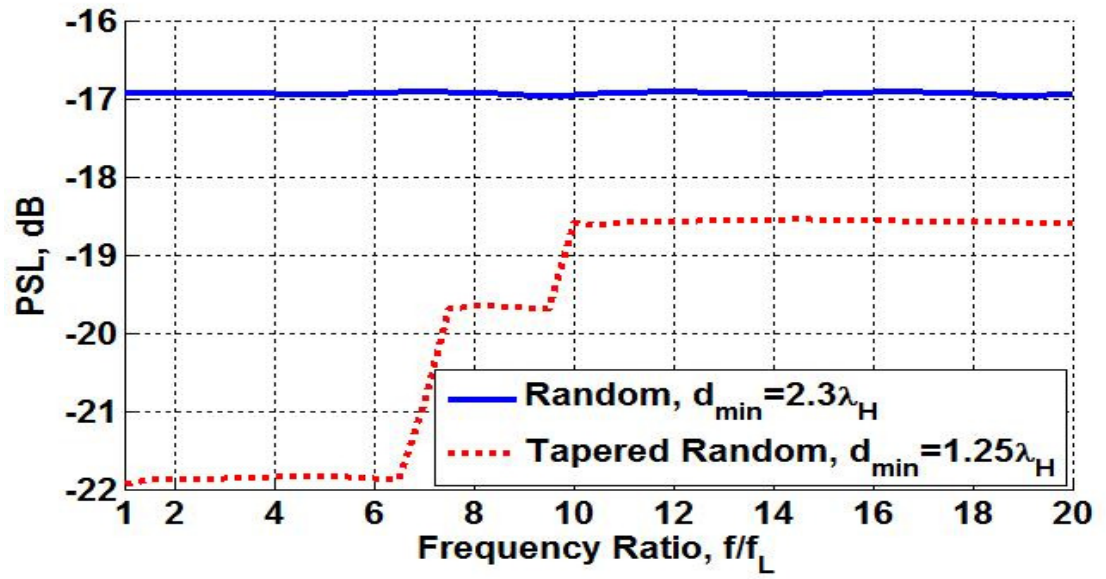


Figure 4.9: Peak sidelobe performance of tapered and un-tapered random arrays

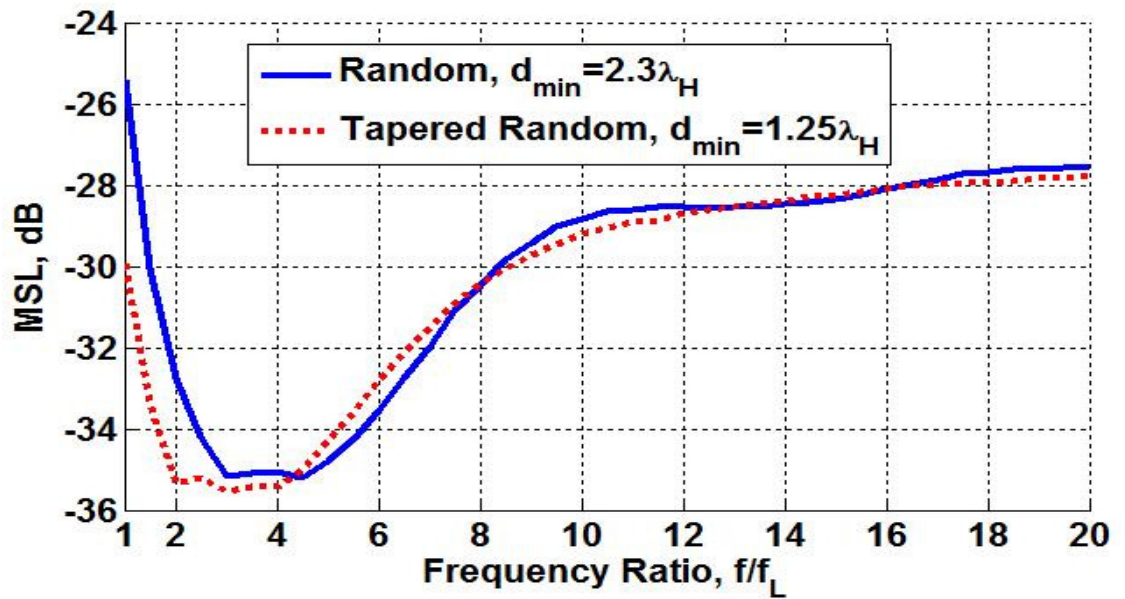


Figure 4.10: Mean sidelobe performance of tapered and un-tapered random arrays

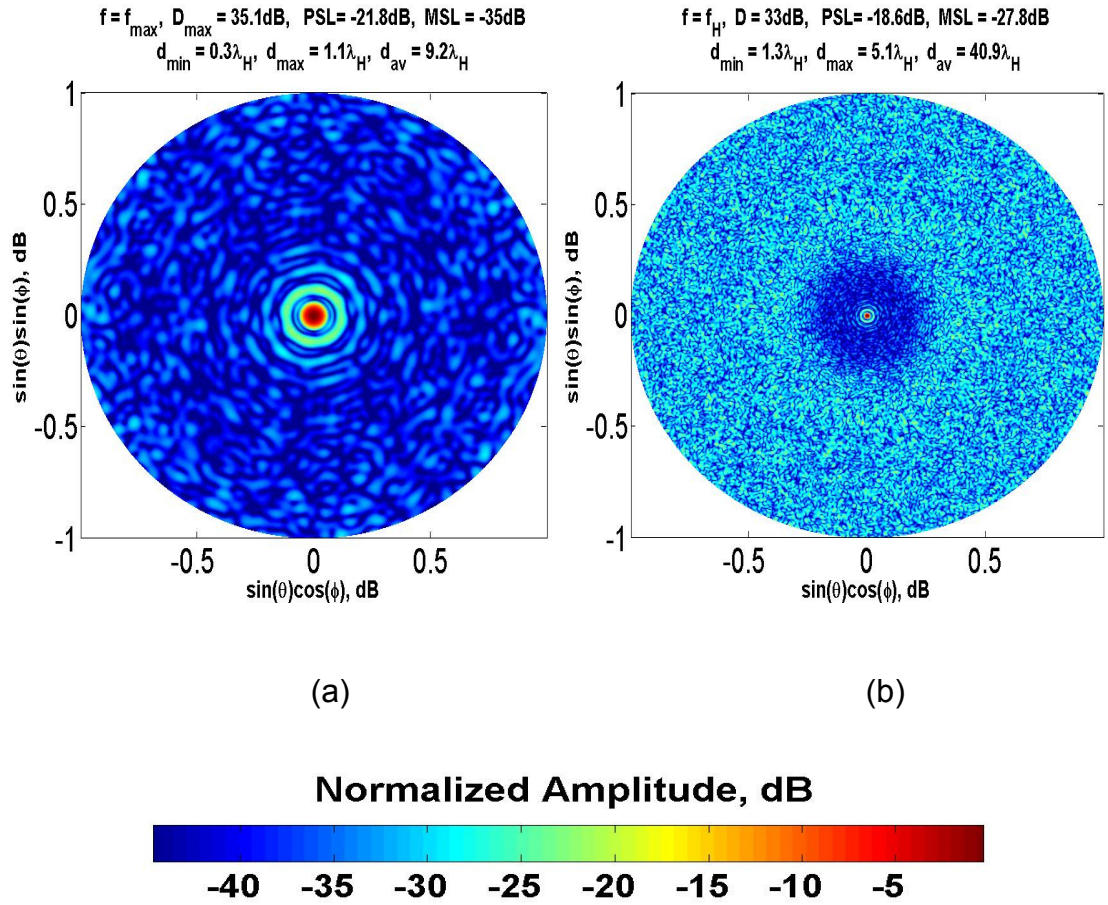


Figure 4.11: Radiation patterns of tapered random array (a) Frequency of maximum achievable directivity (b) Highest frequency

The radiation patterns of the tapered random array are plotted in figure 4.11 at the maximum achievable directivity and the highest frequency.

4.3 Spiral Arrays

A spiral can be defined as a curve which emanates from a central point, getting progressively farther away as it revolves around that point. A common way to describe a two dimensional spiral is by using polar coordinates (r, ϕ) , where r is a continuous monotonic function of the angle ϕ . There are many types of spirals that can be constructed such as Archimedean, logarithmic, Euler [50]. Designing antenna array geometry according to a spiral curve can generate a wide range of

aperiodic geometries that can be useful for optimizing the array broadband performance.

A special case of a logarithmic spiral is the golden angle spiral where its growth factor is related to the golden angle [20].

The polar equation for a Golden angle spiral is:

$$r_n = df(n) \dots \dots \dots (4.1)$$

$$\varphi_n = 2\pi\Phi n \dots \dots \dots (4.2)$$

where, r_n is the radial displacement of the n^{th} element, d is a scaling factor, φ_n is the angular displacement of the n^{th} element and Φ is the golden ratio = 1.618.... [51].

Provided that Φ is maintained as the golden ratio, equations (4.1) & (4.2) define a class of array geometry termed here Golden Angle Spirals defined for various functions $f(n)$.

The function $f(n)$ controls the radius of the n^{th} element from the centre and can be described as a space taper function. It is the design of this function that governs the broadband behaviour of the Golden Angle Spiral class of arrays.

4.3.1 Exponential Taper

The function $f(n)$ can be a simple exponential function $f(n) = n^{exp}$, where n is the index of the n^{th} element. The four arrays shown in figure 4.12 are designed for different exponentials. The larger the exponential value the denser the array elements are around the centre compared to the edges. Each array in figure 4.12 contains 1000 elements and has an aperture diameter of $100 \lambda_H$

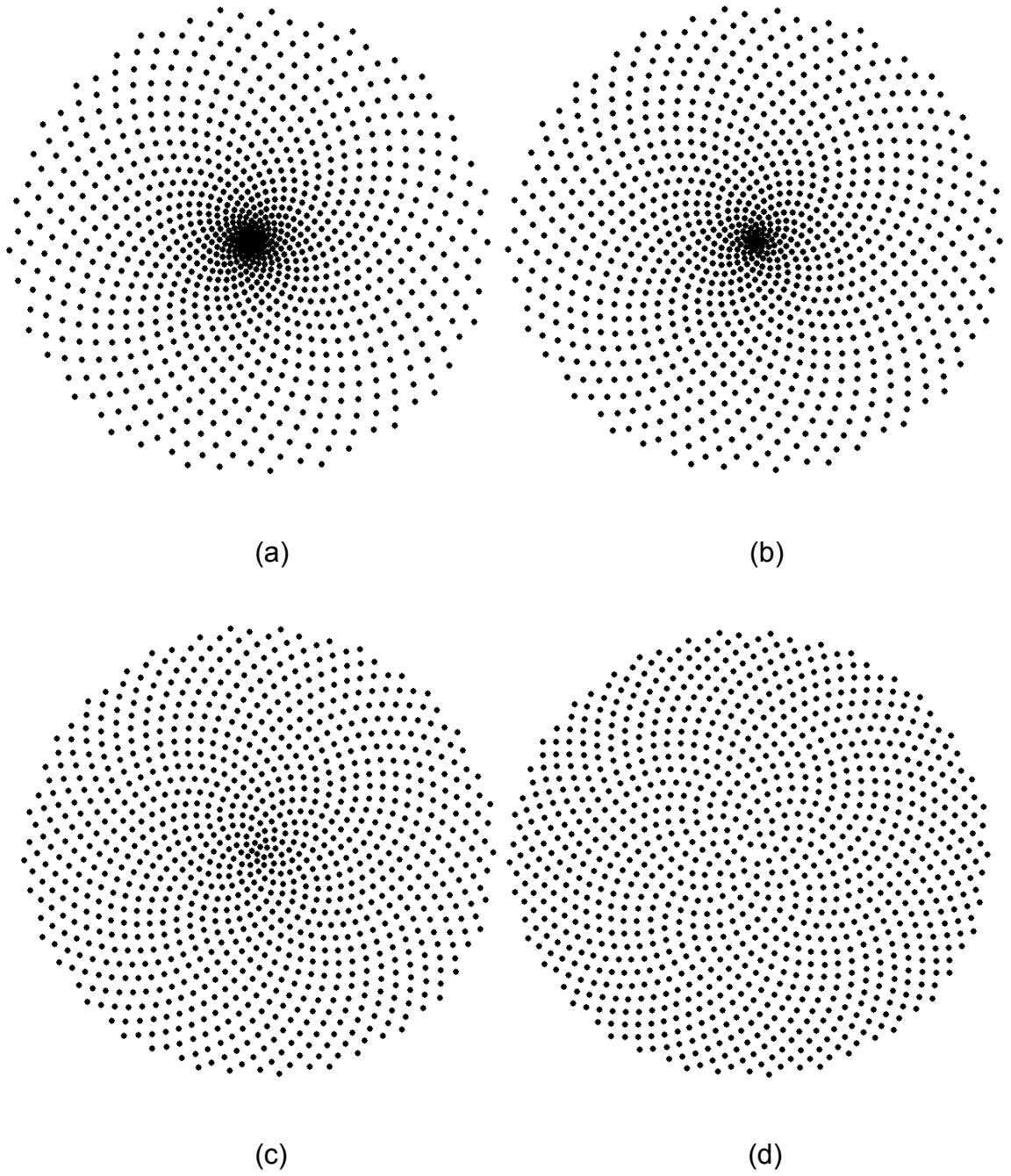


Figure 4.12: Exponential tapered golden ratio spiral (a) $exp = 1$, (b) $exp = 0.7$, (c)

$exp = \Phi^{-1} = 0.6180$, (d) $exp = 0.5$

- **Directivity and side lobe performance**

The directivity and side lobe performance for the exponential tapered golden angle spirals are computed over a (1:20) assuming a hemispherical element. For exponential value 1, as the frequency is increased, the directivity increases and converges towards $N \times D$ at higher frequencies. This is due to its massively dense centre compared to the edges where elements become too close together in terms of wavelength, reducing their contribution to the directivity. As the exponential is decreased, the array becomes less dense in the centre causing the array directivity to increase until a maximum achievable directivity of 38.2 dB when the value of the exponential is 0.5. As the exponential is decreased further, the array becomes sparser in the centre compared to the edges causing the maximum achievable directivity to drop as the array centre becomes more and more under-sampled.

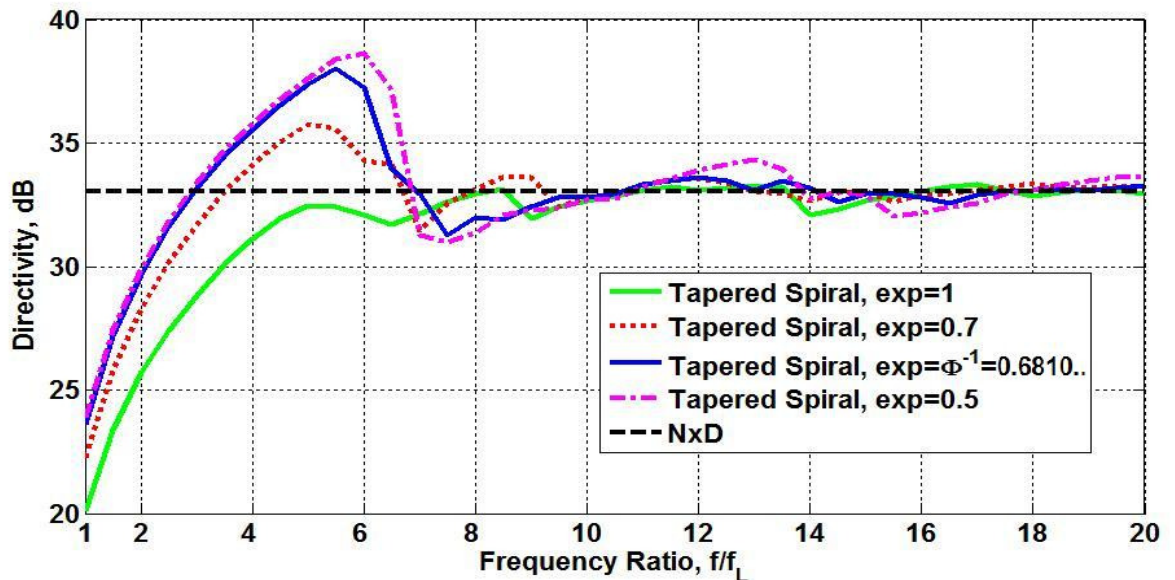


Figure 4.13: Directivity performance for exponential tapered golden angle spiral arrays

The exponentially tapered spirals can achieve the same maximum achievable directivity of a periodic square array with the same number of element (see section 3.1). However, despite the similar sharp directivity drop as the frequency is increased, the directivity converges towards $N \times D$ with little oscillations. Moreover, their peak and mean sidelobe performance can be maintained low over a broadband.

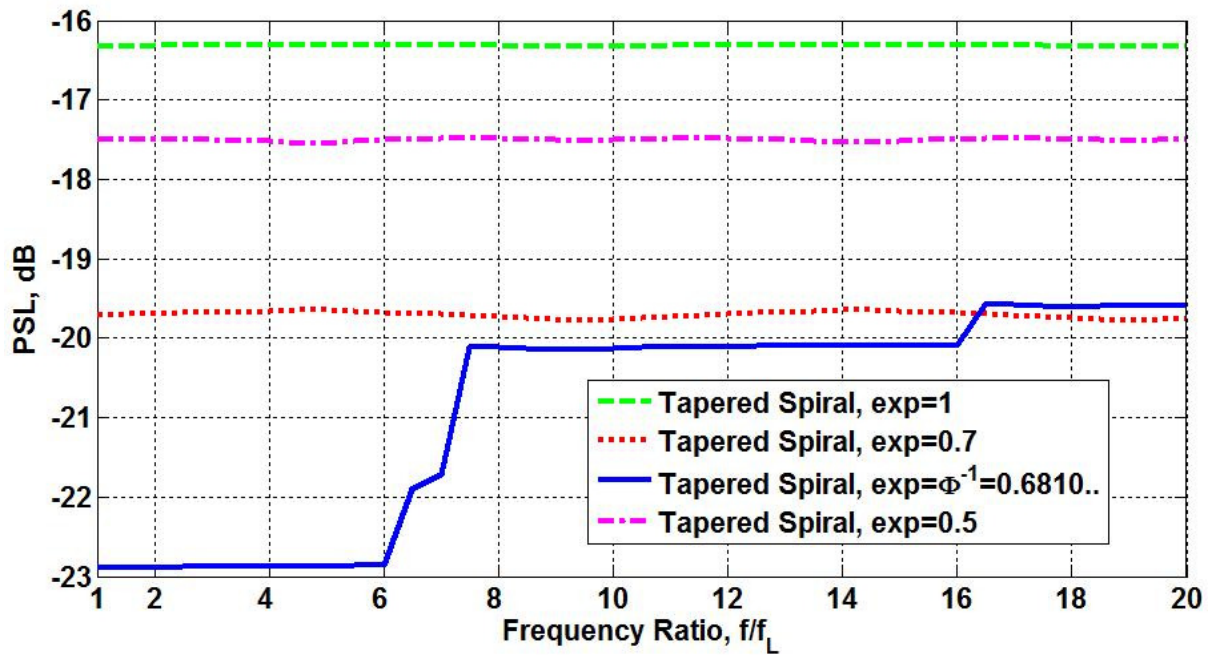


Figure 4.14: Peak sidelobe performance for exponential tapered golden angle spiral arrays

A particularly interesting peak side lobe performance is when the value of the exponential is equal to the golden ratio conjugate. At this point, it is observed that the peak side lobe is the lowest over the band, which then increase as the value of the exponential is changed. All arrays have controlled mean side lobe level converging to -30dB at the highest frequency on figure 4.15.

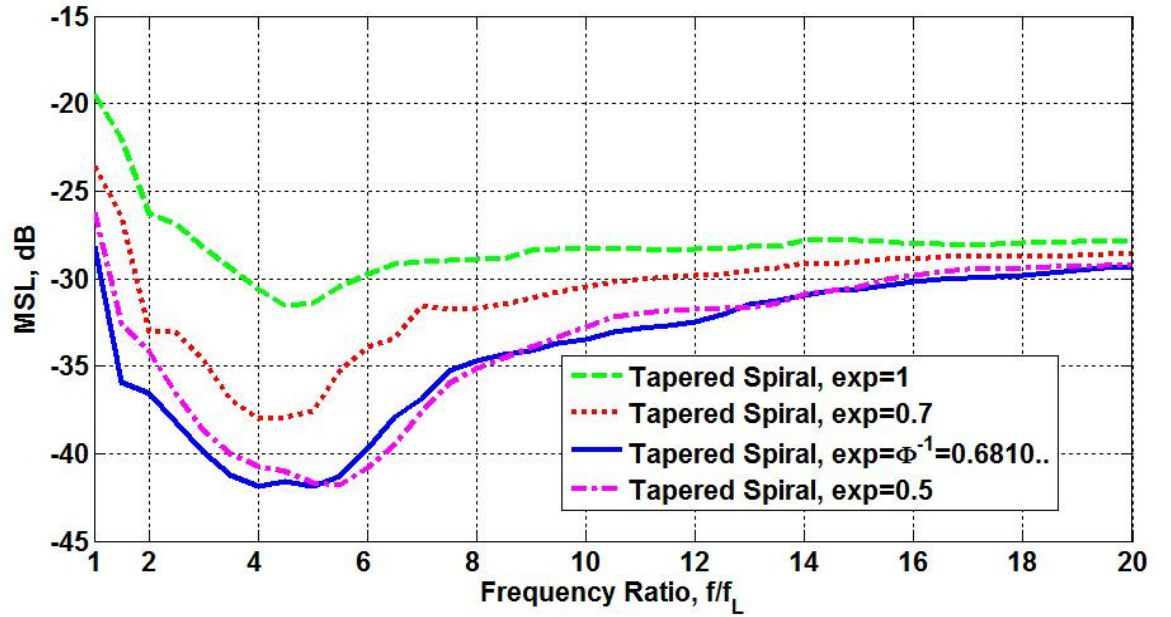


Figure 4.15: Mean sidelobe performance for exponential tapered golden angle spiral arrays

• Radiation Patterns

Similar to the previously considered arrays, the radiation patterns of the different exponentially tapered spiral arrays are considered at the frequencies of maximum achievable directivity, in addition to the highest frequency showing the associated directivity, peak and mean side lobe performance.

Maximum Achievable Directivity

The radiation pattern at the frequency of maximum achievable directivity the different exponentially tapered spiral arrays is shown in figure 4.16. The maximum achievable directivity for the array with most dense centre (figure 4.16(a)) occurs at a relatively higher frequency and does not exceed $N \times D$ with a peak side lobe no lower than -16.3 dB. For other arrays, the side lobe region is as low as -40 dB which can also be observed from the average sidelobe plots in figure 4.15. It is essential to note the minimum separation for each array at its maximum

achievable directivity, where it can be impractically small for an antenna element to be accommodated and have the physical size to operate at that particular frequency.

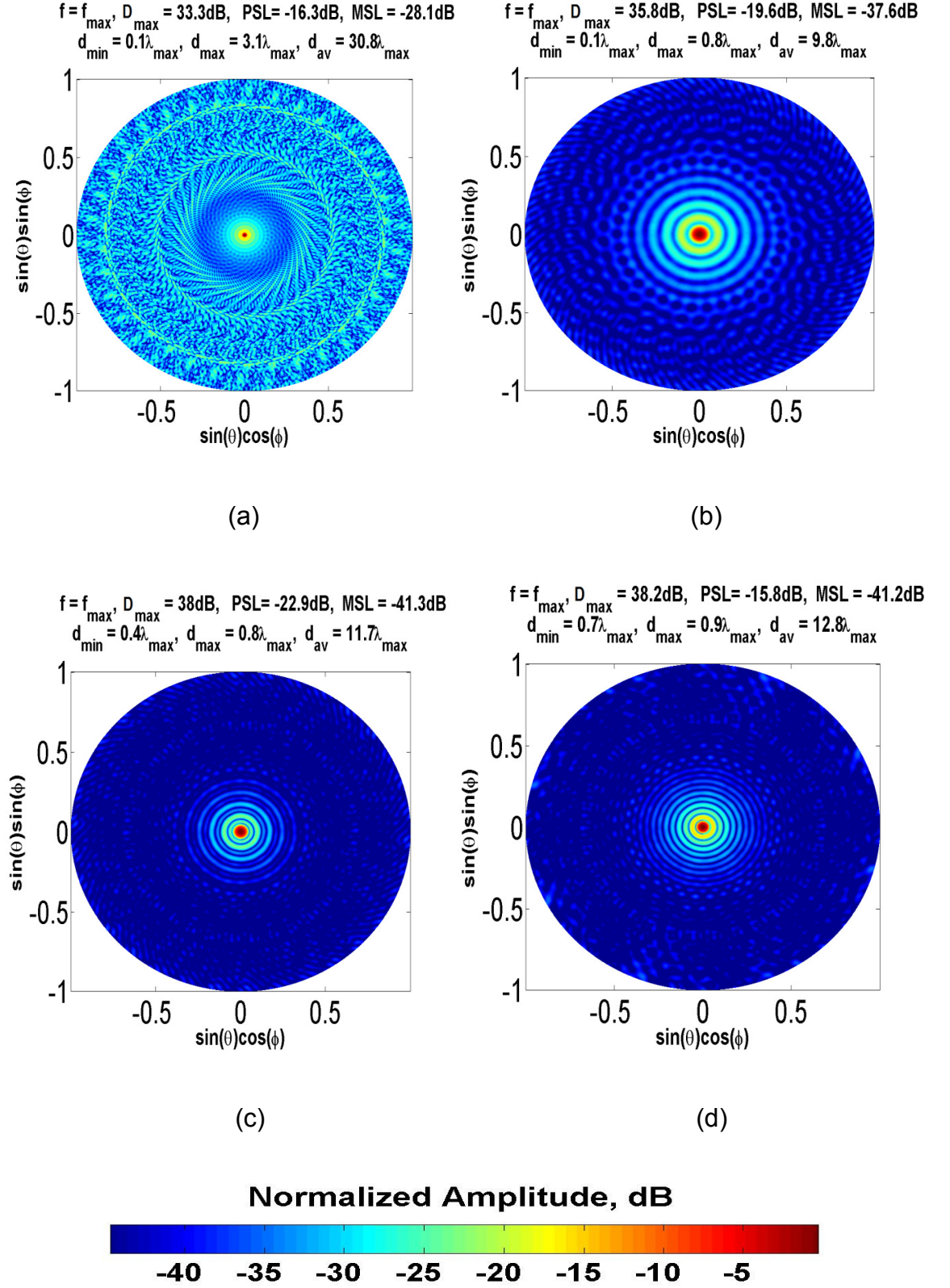


Figure 4.16: Radiation patterns of exponential tapered golden ratio spiral arrays at frequencies of the maximum achievable directivity (a) $\exp = 1$, (b) $\exp = 0.7$, (c)

$$\exp = \Phi^{-1} = 0.6180, \text{ (d) } \exp = 0.5$$

Highest frequency

The radiation patterns at the highest frequency for the exponentially tapered golden angle spirals are shown in figure 4.17. The aperiodic nature of these configurations prevents the formation of grating lobes at high frequencies, despite some element separations exceeding two wavelengths. Instead, approximately equal, level higher side lobes appear in the form of rings appearing at wide angles and move towards the main beam as the frequency is increased. The radiation patterns show the capability of spiral configuration to maintain low sidelobes despite the severe under-sampling.

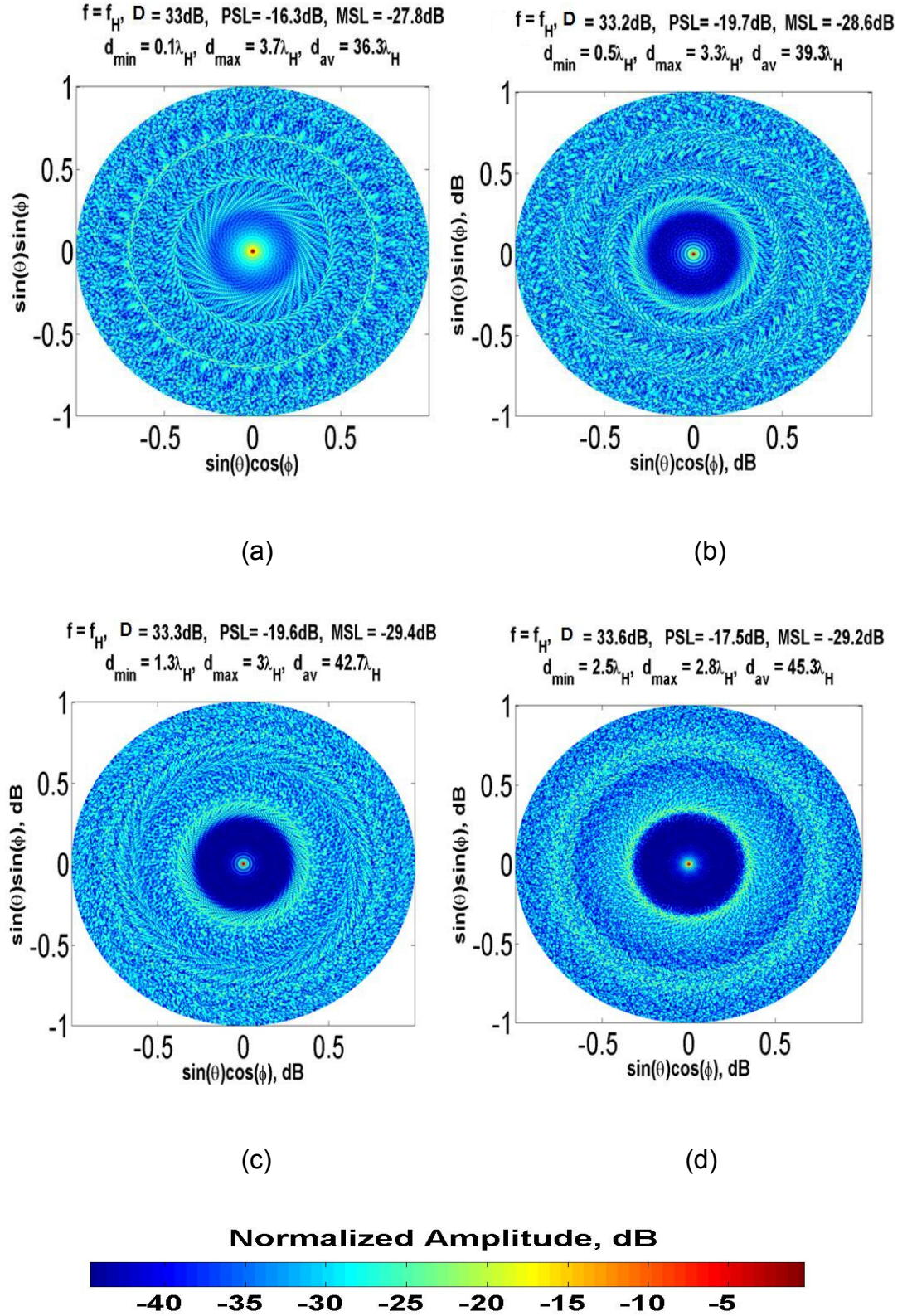


Figure 4.17: Radiation patterns of exponential tapered golden ratio spiral arrays at the highest frequency (a) $\exp = 1$, (b) $\exp = 0.7$, (c) $\exp = \Phi^{-1} = 0.6180$, (d) $\exp = 0.5$

4.3.2 Power Density Taper

So far, array tapering has been achieved by displacing antenna elements relatively closer or further away from the array centre according to certain tapering function as illustrated in section 3.1. Another form of tapering can be achieved by assuming N circles of increasing radii rings ρ_n , $n = 1, 2, \dots, N$ where, number N is the number of elements in the array. A tapering function $A(r)$ can then be selected such that the radius of a particular ring can be determined by integrating the power contained in that portion defined by the desired radius and equating to the total power divided by the total number of elements N . The detail of this algorithm can be reviewed from [21], and the relationship by which the radial distance is determined is shown in equations 4.3 and 4.4 below;

$$2\pi \int_{R_{n-1}}^{\rho_n} A(r)rdr = \frac{2\pi}{2N} \int_0^{R_{ap}} A(r)dr \dots\dots\dots 4.3$$

$$2\pi \int_{R_{n-1}}^{R_n} A(r)rdr = \frac{2\pi}{N} \int_0^{R_{ap}} A(r)dr \dots\dots\dots 4.4$$

Where R_{ap} is the radius of the array and $R_0 = 0$. Once the radial distance of the n^{th} element has been determined, the angular position can be calculated from equation 4.2 for a golden angle spiral configuration. Two array configurations are designed here with a Gaussian window with $\alpha = 2.5$ (see equation 3.1) and Dolph Chebyshev windows for -100dB sidelobe. This is shown in figure 4.17 (a & b). Both arrays are designed with 1000 elements and with aperture diameter of $100\lambda_H$.

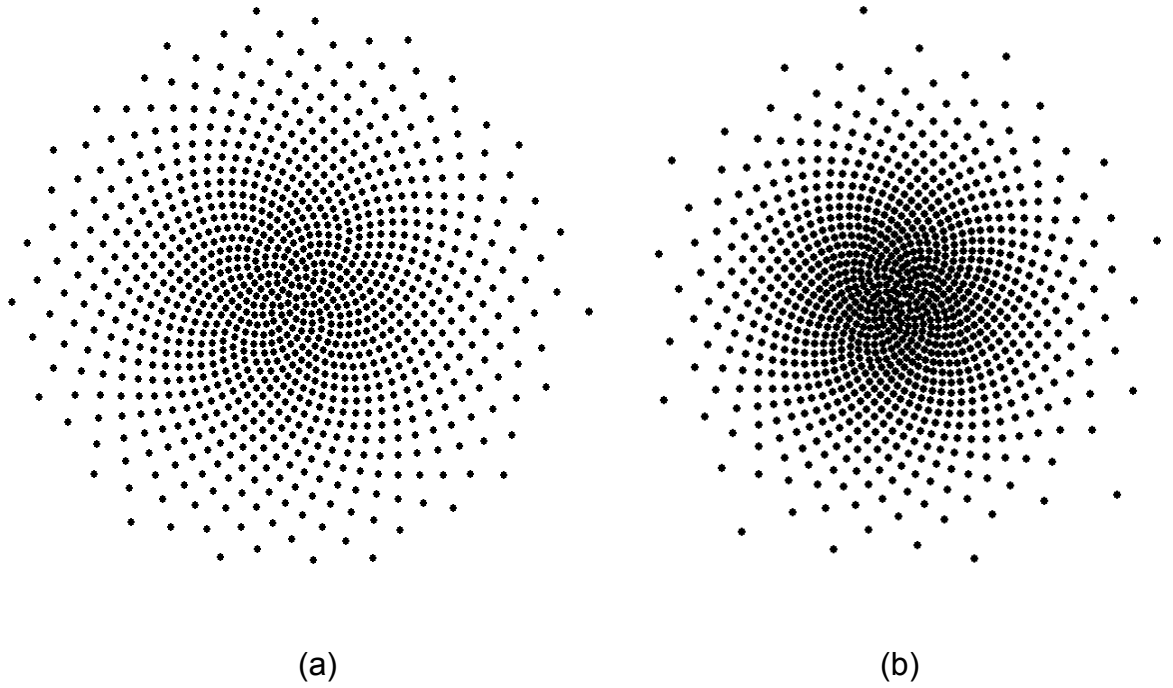


Figure 4.18: Power density tapered arrays (a) Gaussian, (b) Dolph Chebyshev

- **Directivity and sidelobe performance**

The directivity performance of the golden angle power tapered spirals is shown in figure 4.19. The directivity rises smoothly above $N \times D$ and extends for a bandwidth of approximately one and a half octaves before decreasing and converging towards $N \times D$. However, the maximum achievable directivity is reduced by 4 dB compared to the maximum achievable directivity by a square uniform array with the same number of elements (see section 3.1).

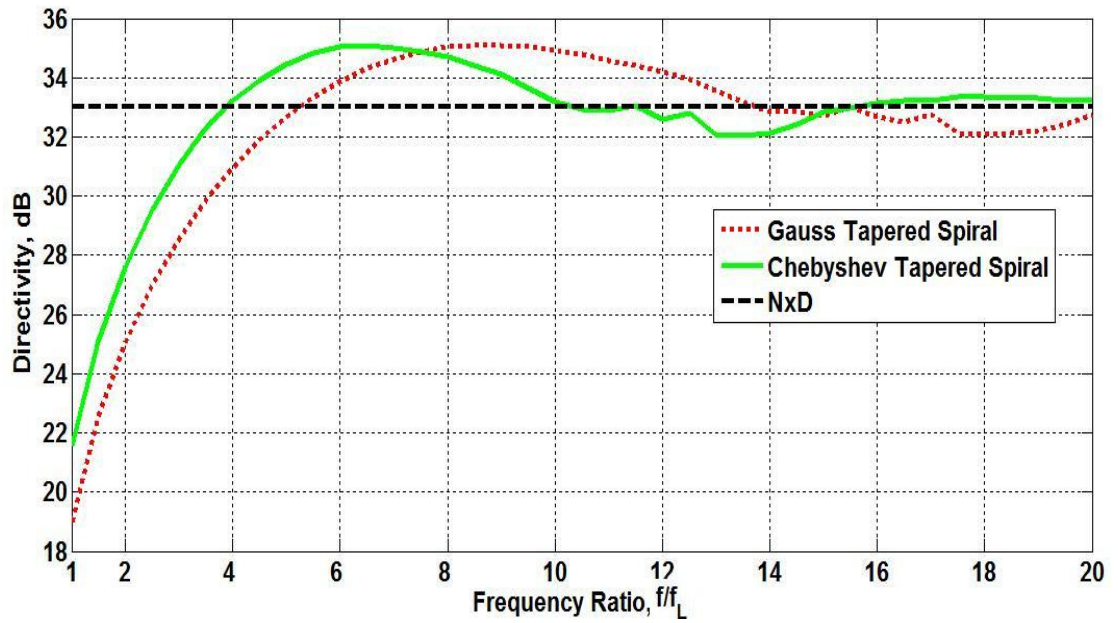


Figure 4.19 Directivity performance for power density tapered golden angle spiral arrays

The peak sidelobes performance given in figure 4.20, shows low peak sidelobes that rise slowly to no more than -19dB at the highest frequency. In addition, the mean sidelobes in figure 4.21 are also low, rising to no more than -29dB at the highest frequency.

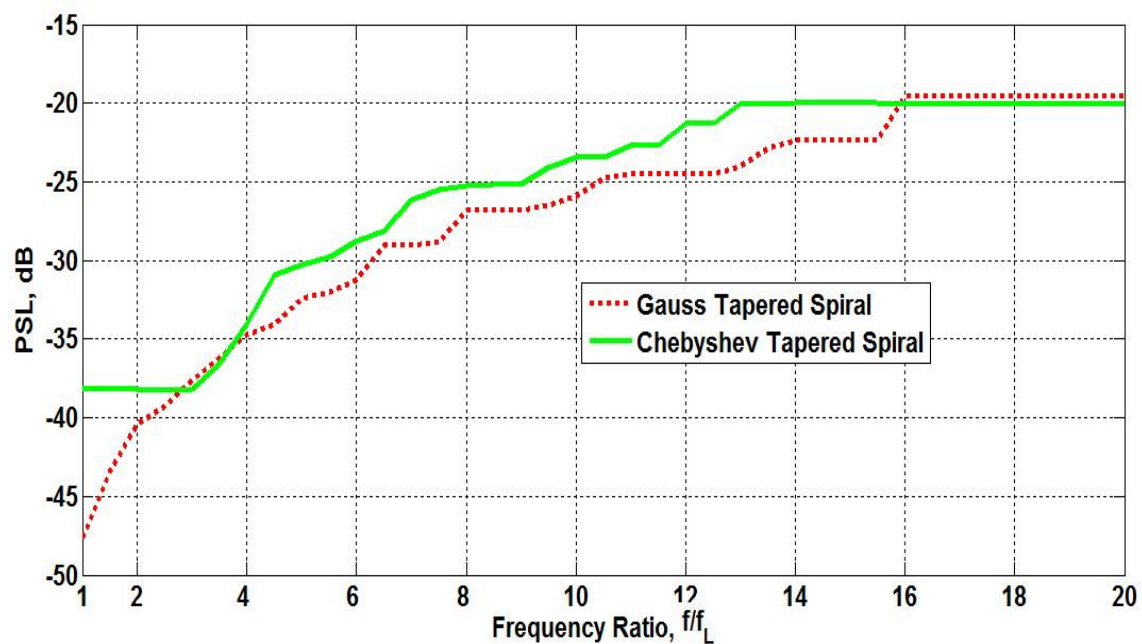


Figure 4.20 Peak sidelobe performance for power density tapered golden angle spiral arrays

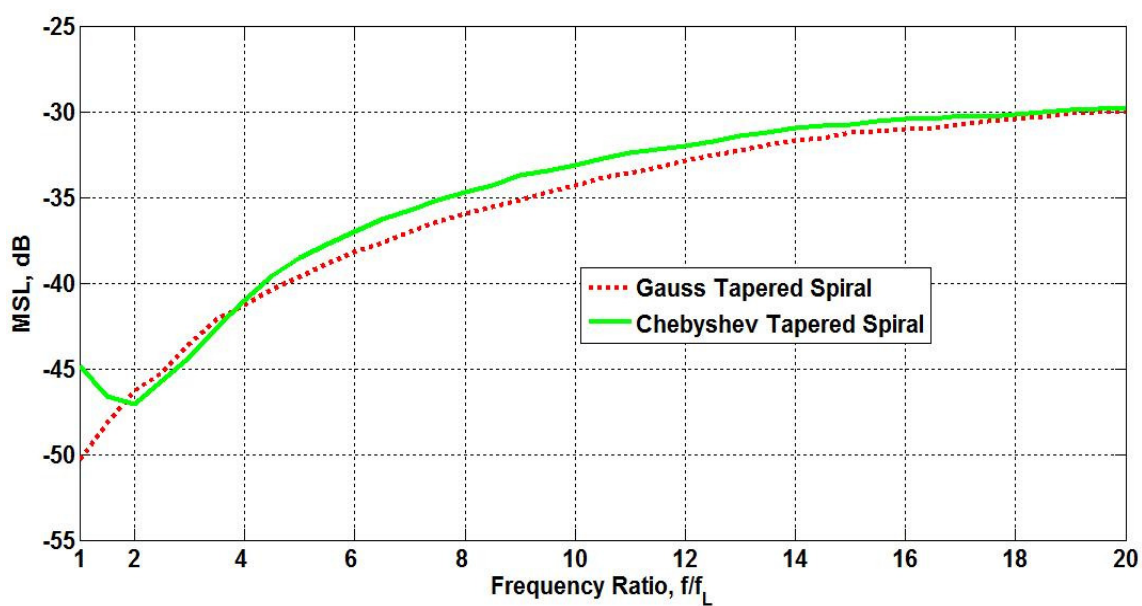


Figure 4.21 Mean sidelobe performance for power density tapered golden angle spiral arrays

- Radiation Patterns

Maximum Achievable Directivity

The radiation patterns of the density tapered spiral arrays at the frequency of maximum achievable directivity are shown in figure 4.22. The radiation patterns show a broader beam compared to previously considered arrays with a maximum achievable directivity to 35.1 dB at a minimum separation of $0.4\lambda_{max}$. The main advantage is a noticeable reduction in peak side lobe level of -28.2dB and -26.8 dB for the Gaussian and Chebyshev density tapered arrays respectively

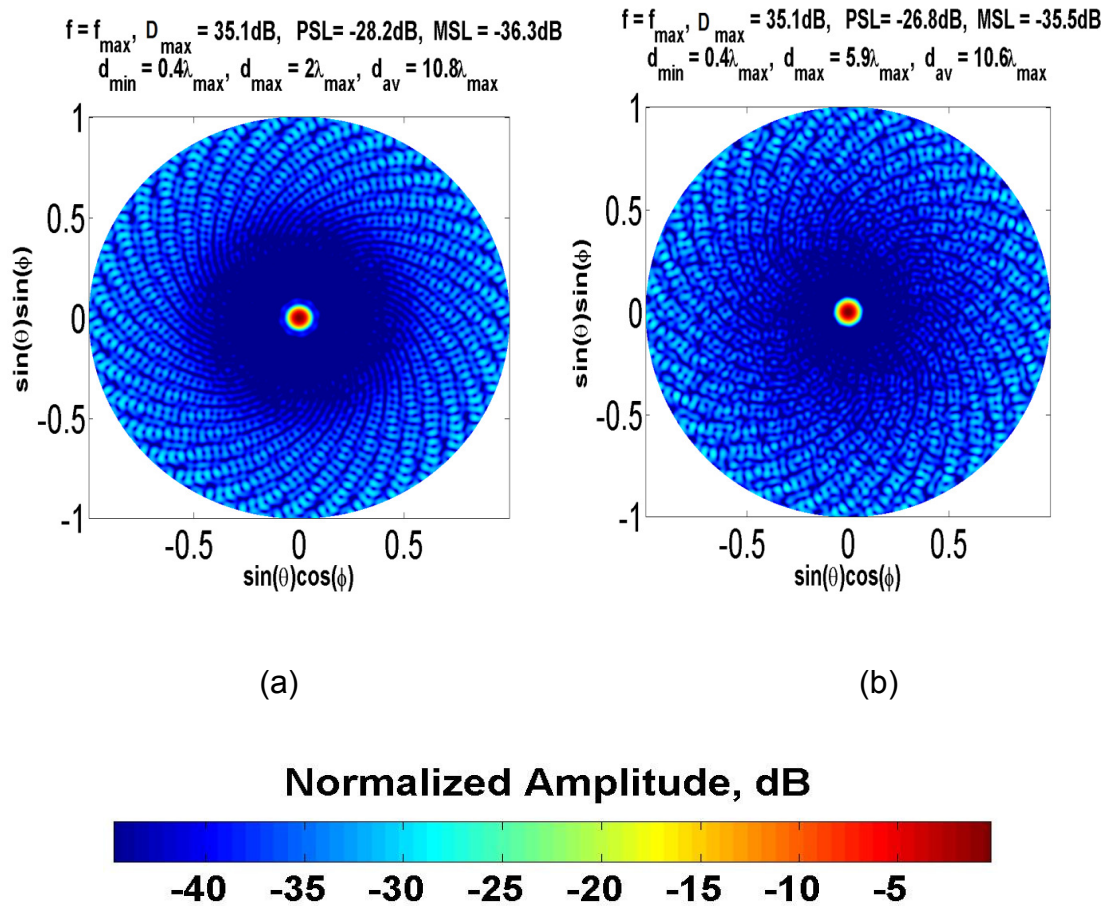


Figure 4.22 Radiation patterns of power density tapered golden ratio spiral arrays at frequencies of the maximum achievable directivity for (a) Gaussian taper (b) Chebyshev taper

Highest frequency

The radiation patterns for the density tapered spiral arrays at the highest frequency are shown in figure 4.23. The radiation patterns show a relatively lower side lobe region particularly near the main beam with no grating lobes despite a minimum separation larger than $1.3\lambda_H$.

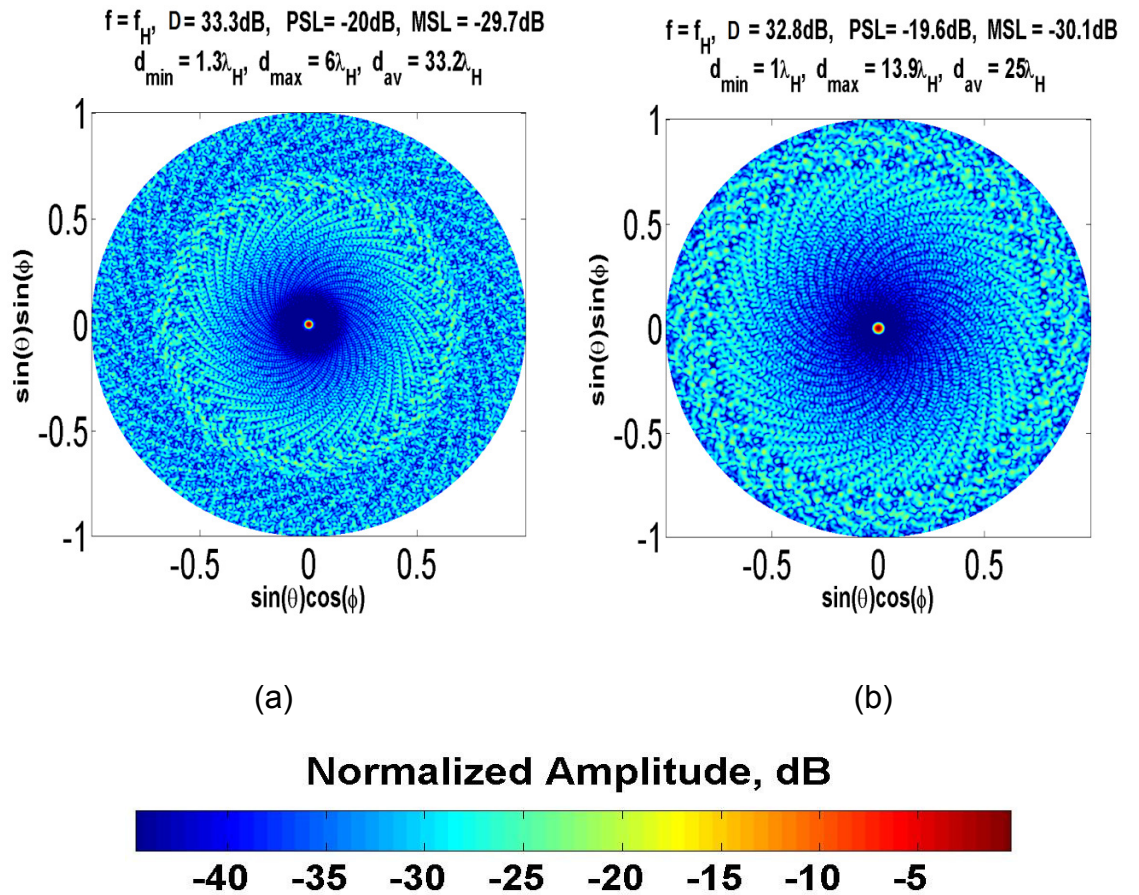


Figure 4.23 Radiation patterns of power density tapered golden ratio spiral arrays at frequencies highest frequency (a) Gaussian taper (b) Chebyshev taper

4.4 Other Array Geometries

From section 1.2.1, many array geometry optimization techniques have been published in the literature. Many of these techniques apply different search algorithms for narrowband performance optimization such as genetic algorithms in [15] and [16]. As mentioned in the same section, search algorithms become computationally complex when large number of elements is considered, particularly for broadband arrays. Therefore, these techniques have not been considered in this thesis due to their limited flexibility. However, a recent publication in [24] utilizes the combination of various aperiodic tiling and genetic algorithms to achieve element distributions that extends the bandwidth performance of the array. However, only the sidelobe performance has been considered for these geometries in [24]. Therefore, the optimized geometries in are discussed in this section.

The arrays from [24] are shown in figure 4.23 having a minimum separation of $1.75\lambda_H$.

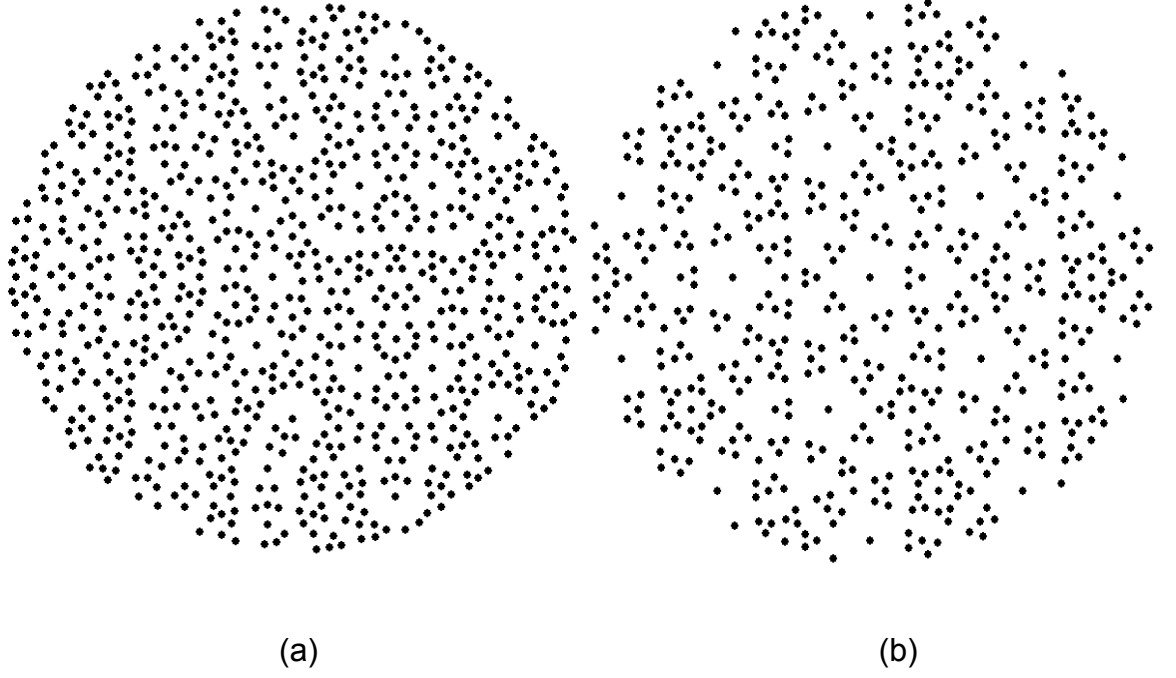


Figure: 4.24 Perturbed Danzer arrays [24]

The arrays from [24] are shown in figure 4.23 having a minimum separation of $1.75\lambda_H$.

- **Directivity and sidelobe performance**

The directivities of the two arrays are compared in figure 4.24 along with their correspondent $N \times D$. The figure shows that the maximum achievable directivity is achieved at minimum separation of $0.48\lambda_{max}$. This maximum achievable directivity is higher than $N \times D$ for both arrays. However, the directivity drops below $N \times D$

and dramatically oscillates at higher frequencies. The directivity drop is caused by a dramatic increase in side lobe level shown in figure 4.25

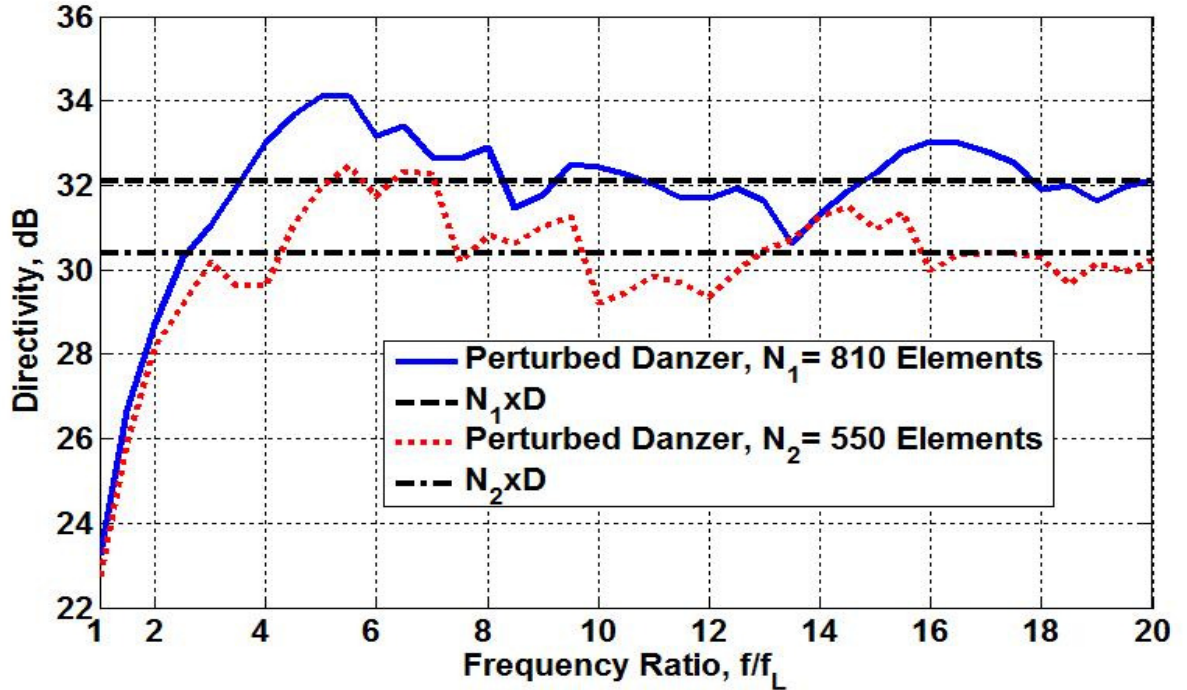


Figure 4.25: Directivity performance for Perturbed Danzer arrays

The rough behaviour of the directivity over the band for these types of array can be explained by the element tiling repetitions across the geometry. This technique forces the overall geometry to be highly irregular preventing any average performance. This leads to a poor directivity performance over the band compared to arrays previously considered arrays such as random and spiral arrays in sections 4.2 and 4.3 respectively.

The peak and mean side lobe level of the two arrays are shown in figures 4.26 and 4.27 respectively. The side lobe performance profile is comparable to that of the uniform concentric rings array discussed in section 3.3.

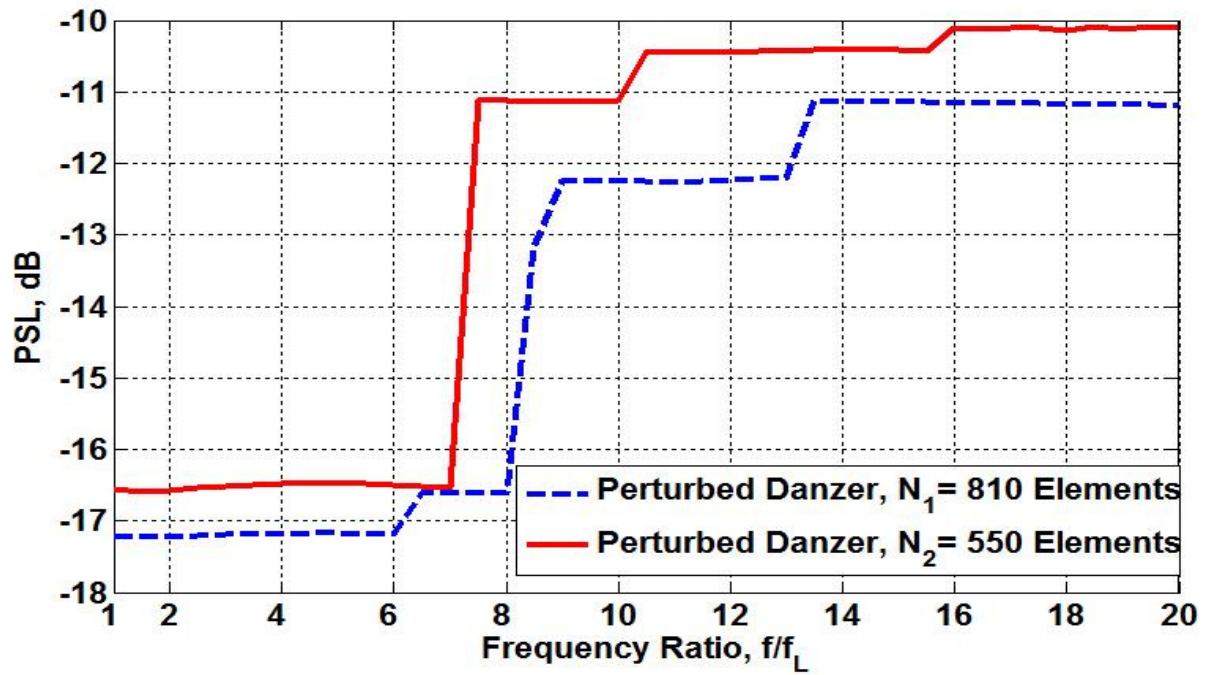


Figure 4.26: Peak sidelobe performance for Perturbed Danzer Arrays

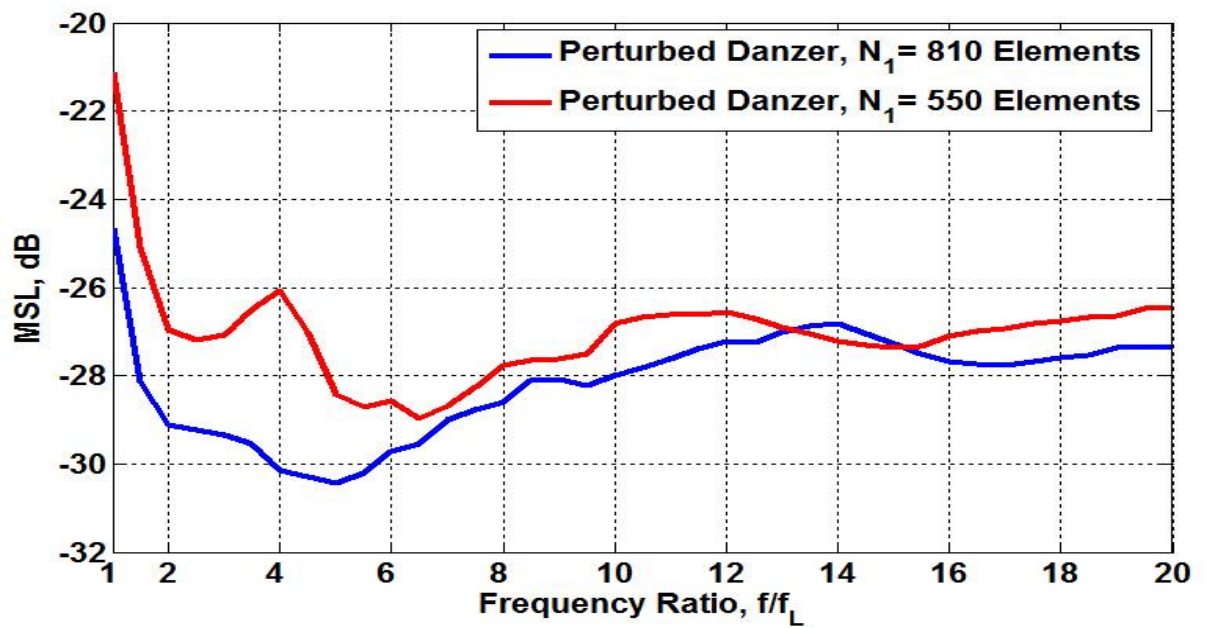


Figure 4.27: Mean sidelobe performance for Perturbed Danzer Arrays

4.6 Periodic Vs Aperiodic Array Comparison

The previous geometry studies shows how the element distribution can be utilized to tradeoff the broadband performance of antenna array. To outline this further, figures 4.28-2.4.30 compares the directivity, mean and peak side lobe performance for selected periodic and aperiodic arrays. The compared arrays are the periodic square and concentric rings array discussed in sections 3.2 and 3.3 respectively against the aperiodic random and gauss tapered golden ration spiral discussed in sections 4.2 and 4.3 respectively. Similar to the approach outlined in the geometry optimization technique in section 2.2, all arrays have equal number of elements and aperture dimensions.

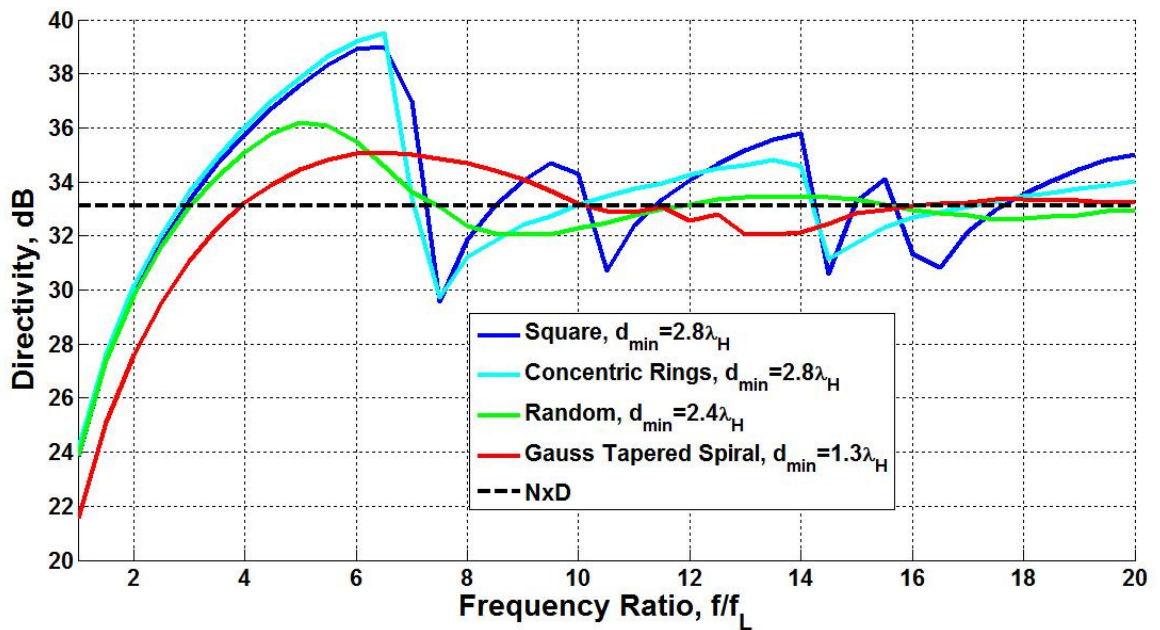


Figure 4.28: Directivity performance for periodic and aperiodic arrays

The results show how the high maximum possible directivity achieved by the periodic square and concentric rings array has been compromised for a better directivity performance over a wide band obtained by the smoother directivity response over the band

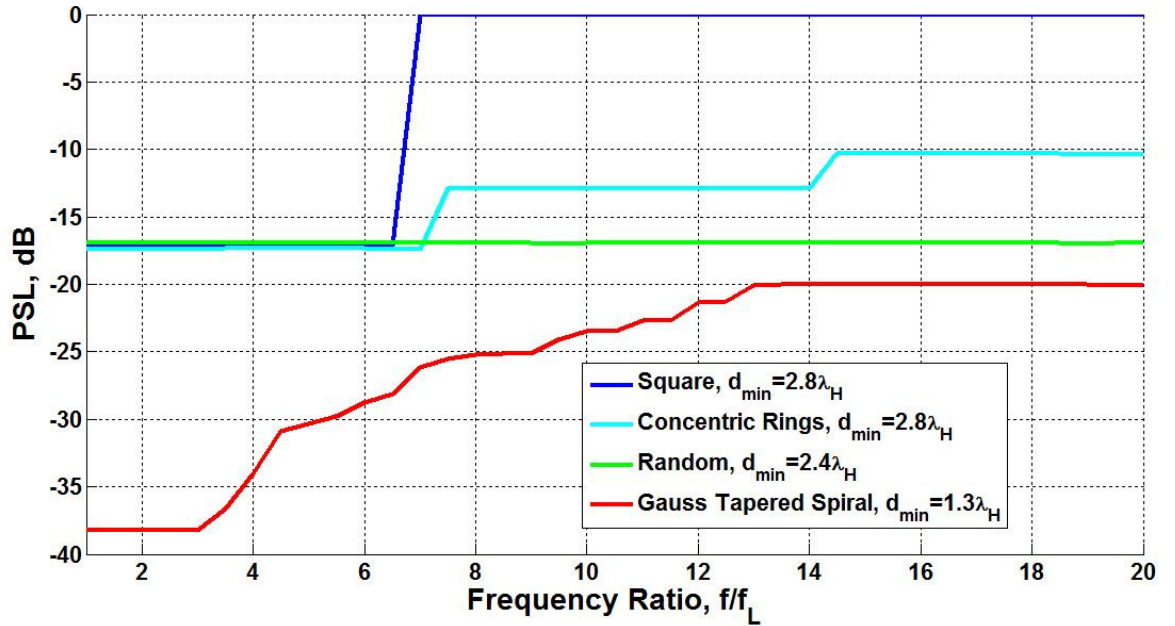


Figure 4.29: Peak side lobe performance for periodic and aperiodic arrays

This is obtained by eliminating the grating lobes in the case of the square periodic array and the high peaks in the periodic concentric rings array via the optimized aperiodic distributions for the random and gauss tapered spiral arrays.

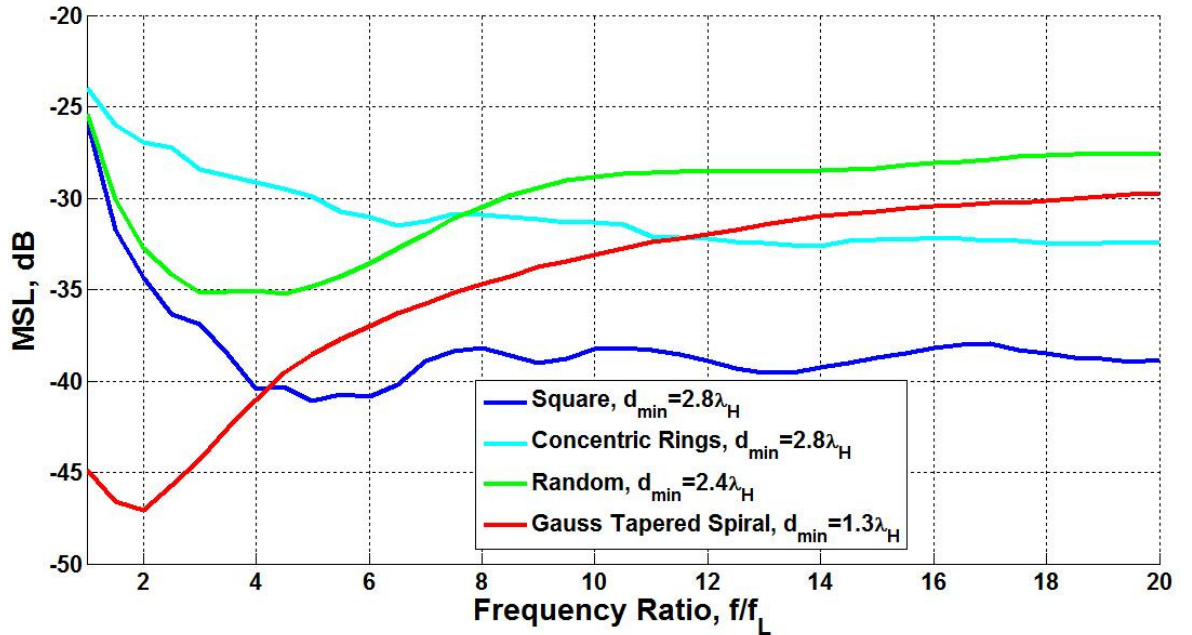


Figure 4.30: Mean side lobe performance for periodic and aperiodic arrays

4.5 Chapter Summary

This chapter considered the broadband performance and optimization of various aperiodic arrays. The study shows that aperiodic arrays are in general more superior in terms of cost efficiency than periodic arrays where higher directivity than $N \times D$ can be achieved over a much wider bandwidth from the same number of elements. This is achieved by avoiding close element separations which causes redundancy in terms of number of elements at low frequencies. In addition, various non-iterative techniques such as randomization algorithms and space tapering can be utilized to further improve the broadband performance. The tapering reduces the maximum achievable directivity at a narrow band, but can offer an improvement in terms of directivity and side lobe performance over wider bandwidths. A class of aperiodic arrays based on the golden angle spiral are shown to offer an attractive potential for cost efficient broadband array design showing a superior broadband directivity and sidelobe performance over other arrays.

The geometry study has shown the potential of a higher directivity with slightly dense geometries where the element separation is less than one wavelength. These arrays are termed here as semi-sparse arrays.

Chapter 5: Scaling and Mutual Coupling

5.1 Introduction

The geometry studies presented in chapters 3 and 4 show the broadband performance tradeoffs offered by the antenna element distribution in antenna arrays with equal number of elements and aperture dimension. The chosen sample size i.e. the number of antenna elements for these studies is equal to 1000. However, for general applications, it is necessary to be able to scale the arrays and their performances in order to meet performance requirements for various applications. Moreover, the effect of an antenna element pattern as well as the electromagnetic interaction between neighbouring antenna elements is essential for the evaluation of the overall performance. Therefore, a number of scaled array models are designed for full wave simulation comparison (in CST Microwave Studio) using the fork tapered slot antenna presented in section 2.2 as the antenna element.

The geometry studies also show that various random and tapered arrays can in general be more cost effective in terms of bandwidth than other array geometries, and therefore are more attractive for large scale applications. In addition, broadband periodic arrays have been widely considered in the literature [43]. Therefore, two types of aperiodic geometries are selected. A Gauss density

tapered spiral (we call this here “tapered spiral”), and a random array. The detailed design of these geometries is outlined in sections 4.2.2 and 4.1 respectively

5.2 Scaled model

The geometry optimization method in section 2.1 starts by assuming a constant number of elements over a constant aperture dimension. Then the elements are distributed with that aperture according to simple analytical function to yield the different geometries in chapters 3 and 4. In order to scale the arrays while maintaining its performance profile, the number of elements must be scaled as the aperture area. That is maintaining the same number of elements per unit area. Then, the same analytical function is used to distribute the new number of antenna elements over the scaled area.

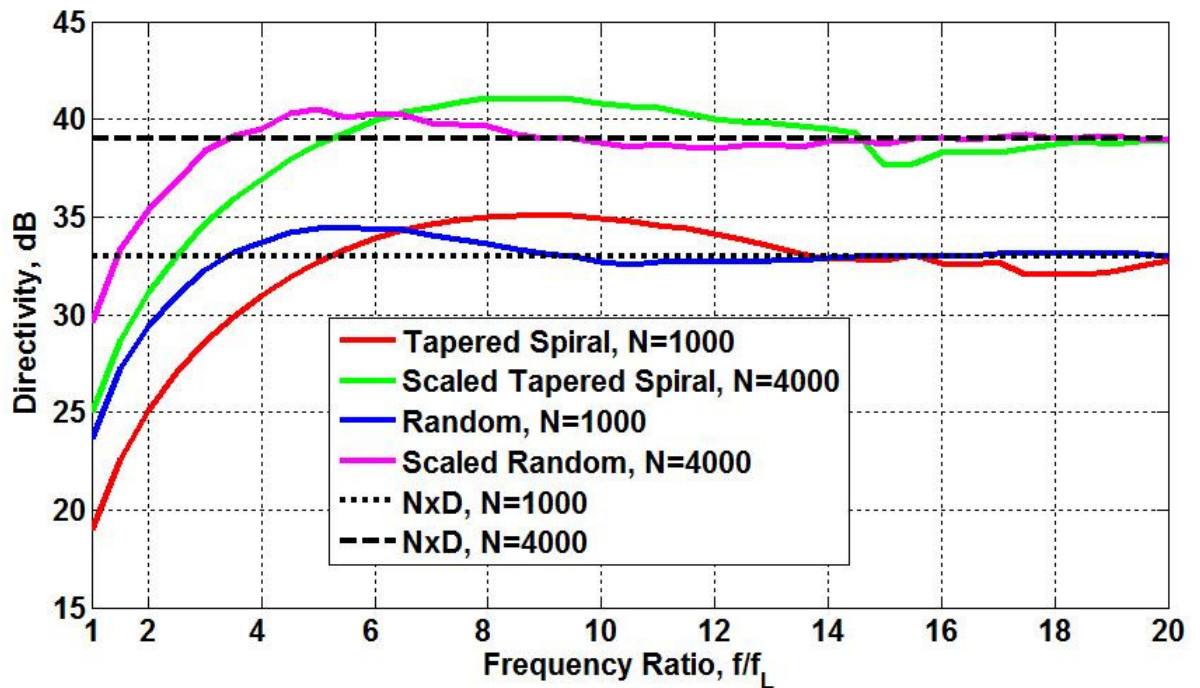


Figure 5.1: Directivity performance for scaled random and spiral arrays.

This can be demonstrated initially by designing a tapered spiral and a random array of 1000 elements and scaling their areas as well as the number of elements by 4. The minimum separations for the 1000 element arrays are $1.3\lambda_H$ and $1.7\lambda_H$ for the tapered spiral and random arrays respectively. The minimum separation for the scaled 4000 element arrays are $1.25\lambda_H$ and $1.7\lambda_H$ for the tapered spiral and random arrays respectively¹⁰. The directivity and mean side lobe performance for the original and the scaled arrays are shown in figures 5.1 and 5.2 respectively. The figures show the expected directivity increase of 6 dB for the larger arrays which also lead to a 6 dB reduction in mean side lobes. The performance profile of the scaled arrays in figures 5.1 and 5.2 is well preserved over the band. This is useful since it allows for more flexible geometry optimization of a manageable number of elements to achieve a required performance profile over the band before scaling the arrays to meet a certain minimum requirement. This is considered further in chapter 8.

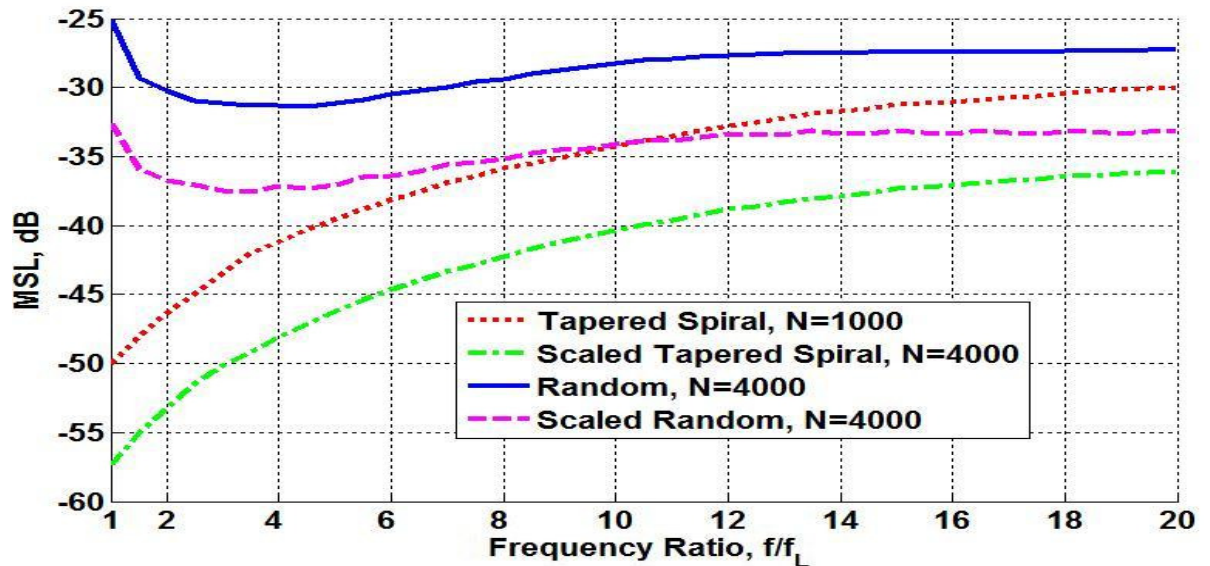


Figure 5.2: Mean sidelobe performance for scaled random and spiral arrays

¹⁰ The scaling of tapered array by the outlined scaling method does guarantee the same minimum separation and must be considered with care in order to allow for the physical size of the antenna element.

The peak side lobe performance of the original and scaled arrays is shown in figure 5.3. For the random array, the peak side lobe remains the same over the band despite scaling the array. This is due to the peak side lobe being the first side lobe near the main beam which remains the highest over the band. However, the far out sidelobes will continue to rise at higher frequencies, caused by the increasing under-sampling, until exceeding the level of the first sidelobe (not shown here). In the case of the tapered array where the first side lobe is a low -24dB, due to the tapered distribution, the peak side lobes is at far angles from the main beam at higher frequencies and continue to rise as the frequency is increased. Therefore, the scaled tapered array peak side lobe is also reduced by 6 dB.

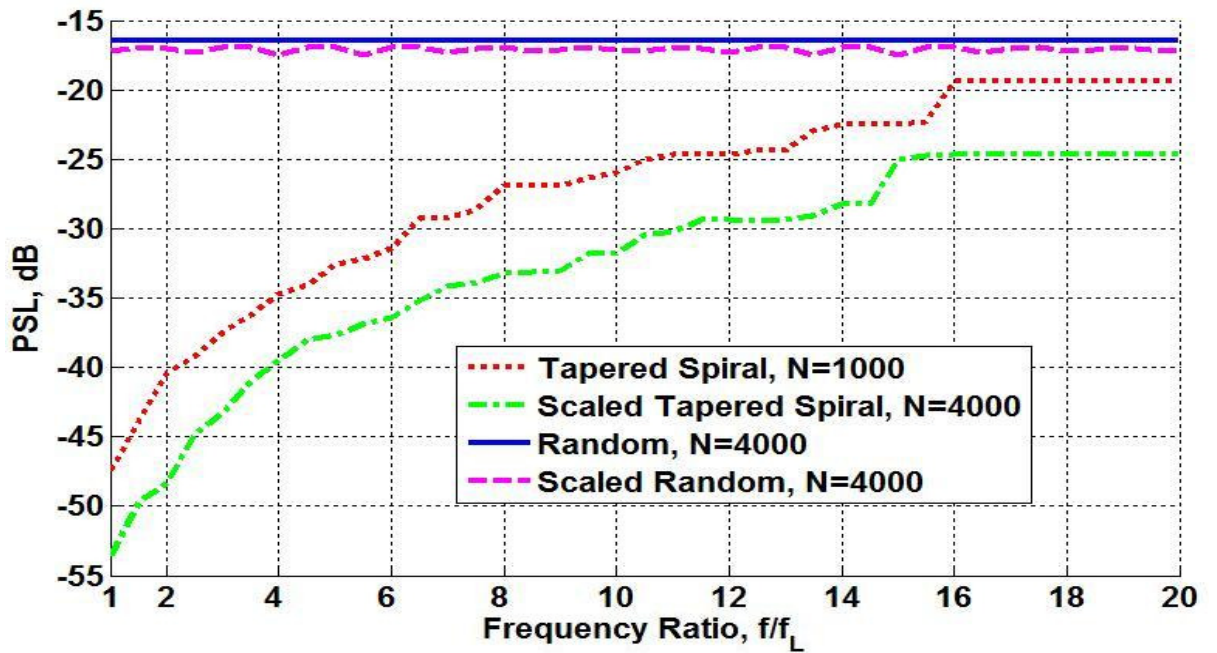


Figure 5.3: Peak side lobe performance for scaled random and spiral arrays.

The previous calculations have been carried out assuming a constant element radiation pattern with the effect of mutual coupling ignored. Unfortunately, due to the large size of these arrays, a full wave simulation is impossible to achieve by

the available commercial electromagnetic computational tools. However, reasonable predictions can be made regarding the array geometry, scaling and the overall mutual coupling effect.

5.3 Full wave Scalability

A tapered spiral array of a 32 fork tapered slot antennas is designed to operate between 0.3 and 1.3 GHz with a maximum possible directivity at 0.3 GHz the maximum directivity of the tapered spiral array corresponds to frequency ratio of 8 in figure 5.1. The array is shown in figure 5.4 (a). Another array is designed with twice the aperture area and number of elements shown in figure 5.4 (b).

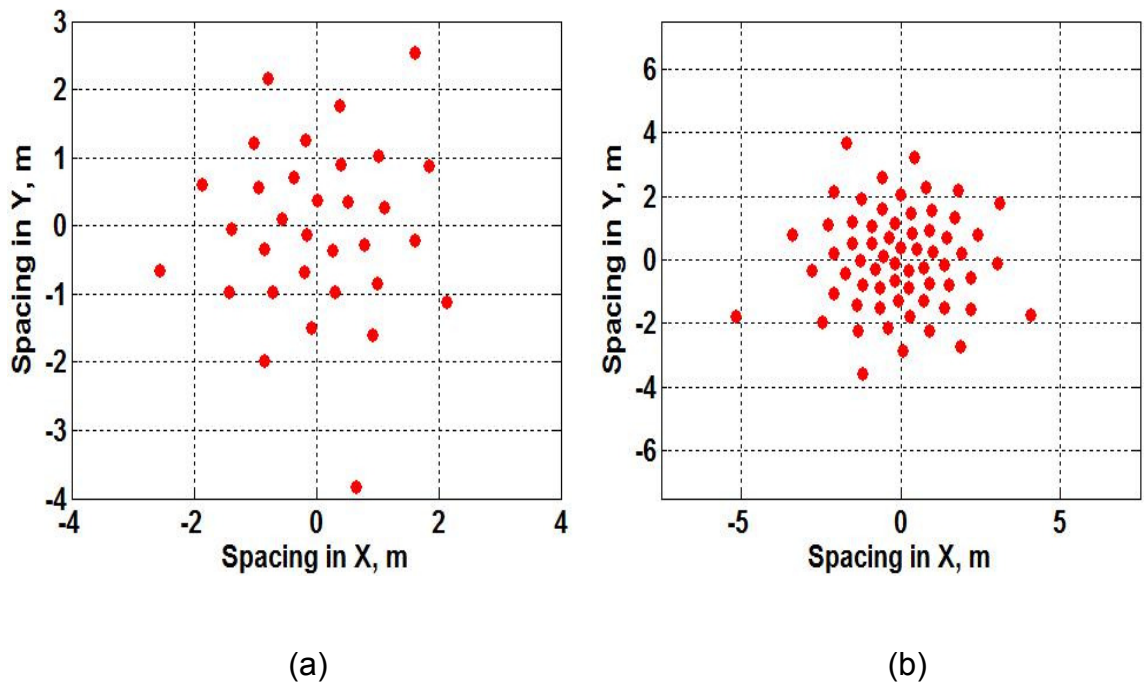


Figure 5.4 Scaled arrays for full wave Simulation performance for tapered spiral arrays, (a) 32 elements (b) 64 elements.

A full wave simulation was then carried out using CST microwave design studio for a uniform amplitude and phase simultaneous excitation where the radiation

patterns and total return loss for all elements are computed over the band for both arrays.

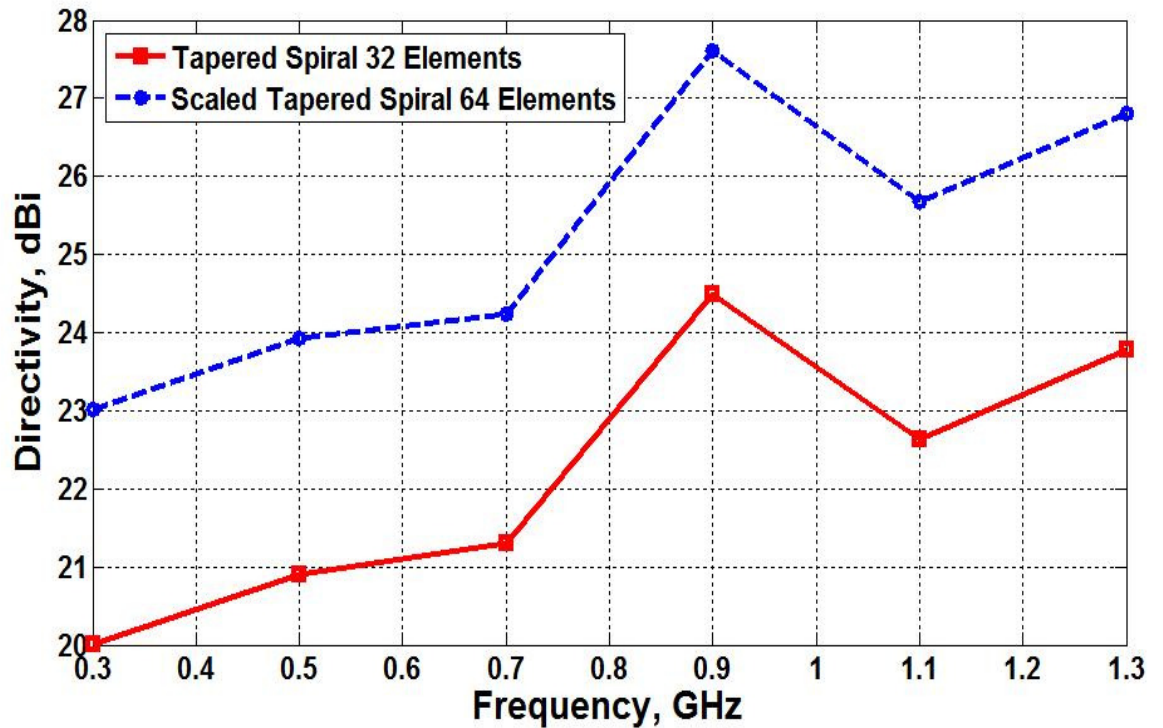


Figure 5.5: Directivity performance for scaled tapered spiral arrays.

The directivity and side lobe performances are shown in figures 5.5-5.7. The results show a good approximation to the scalability where an expected 3 dB increase in directivity has been achieved while a 3dB reduction is seen for the mean side lobe level.

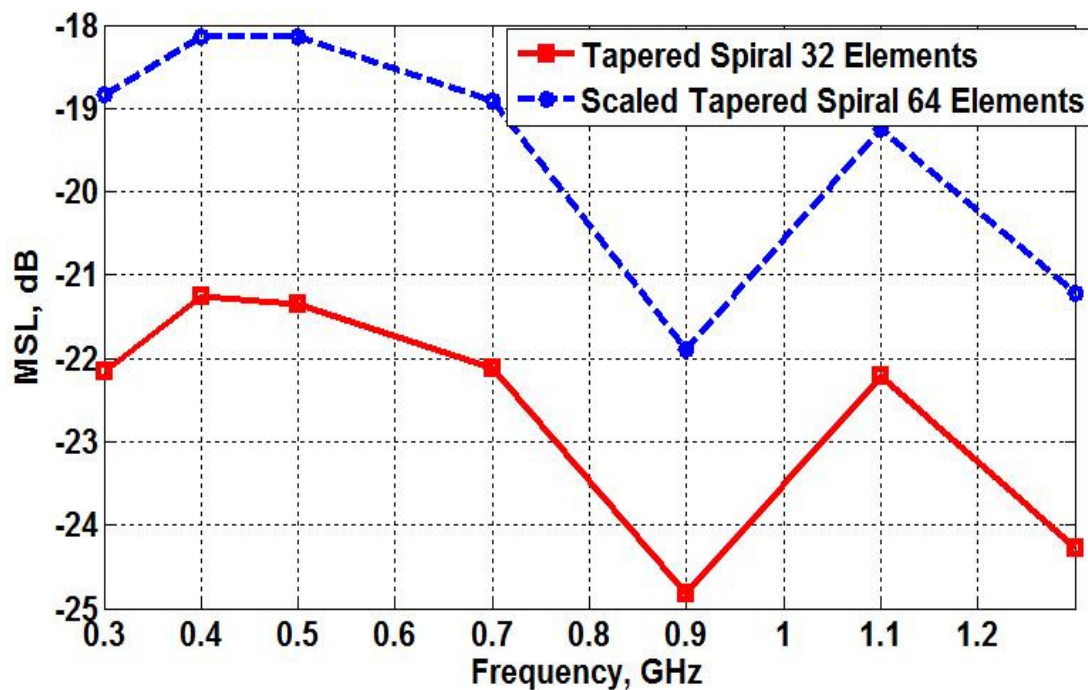


Figure 5.6: Mean side lobe performance for scaled Tapered spiral arrays.

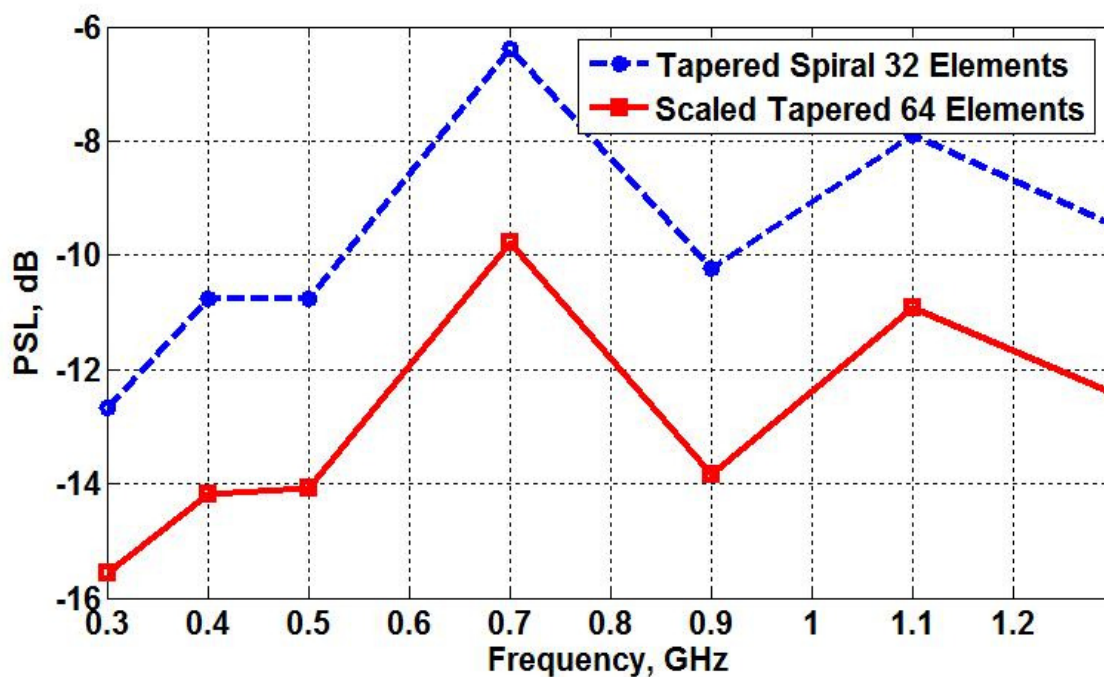


Figure 5.7: Mean sidelobe performance for scaled Tapered spiral arrays.

Mutual Coupling effect

From section 2.4 it is shown that the effect of mutual coupling can change the impedance matching at the array elements feed point resulting in mismatch and hence loss of efficiency. Therefore it is possible to assess the effect mutual coupling over the band by computing the array total efficiency. This can be calculated from

$$\eta_{total} = \eta_{loss} \eta_{rad} \dots \dots \dots (5.1)$$

Where η_{loss} is the mismatch efficiency and η_{rad} is the radiation efficiency. Since perfect conductors are assumed for this simulation the radiation efficiency is close to 100% and can be negligible. The total efficiency for the two tapered spiral arrays as well as the isolated antenna element is shown in figure 5.8.

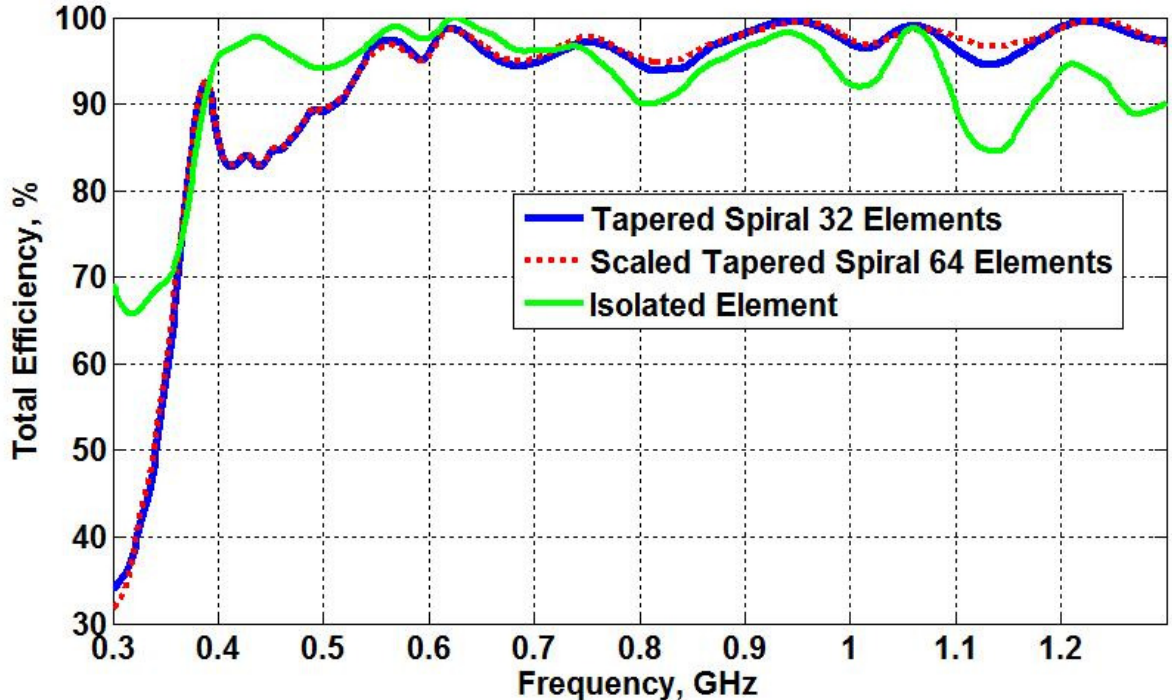


Figure 5.8: Total Efficiency for Isolated element, Tapered Spiral and scaled Tapered spiral arrays.

The results show the effect of mutual coupling on the total efficiency of the array where the efficiency drops at low frequency due to closer element separation in term of wavelength. This illustrates the complex behaviour of the coupling on the overall efficiency performance

In addition, the result show the similar effect of mutual coupling on efficiency for the two arrays except at the low end of the band where the coupling is higher. The result shows that it is possible to estimate the effect of mutual coupling on the total array efficiency for larger scaled geometries particularly at high frequency where the mutual coupling effect on the impedance is low.

5.4 Full Wave Geometry Comparison

In order to demonstrate the effect of the geometry with a full wave solution, a 32 element random array is designed with the same aperture area as the 32 element tapered spiral from the previous section. Subsequently, similar to the tapered spiral array, the random array also corresponds to frequency ratio 8 in figure 5.1. The Tapered spiral and random arrays are shown in figure 5.9 with minimum separations of 0.46λ and 0.56λ respectively, where λ is the wavelength at the lowest frequency of 0.3 GHz. Therefore, these arrays are semi-sparse arrays.

The directivity performance of the two arrays is shown in figures 5.10 where an expected 1 dB directivity increase at low frequencies is achieved with the tapered spiral array while both arrays having equal directivity at higher frequencies. This is consistent with directivity comparison in figure 5.1.

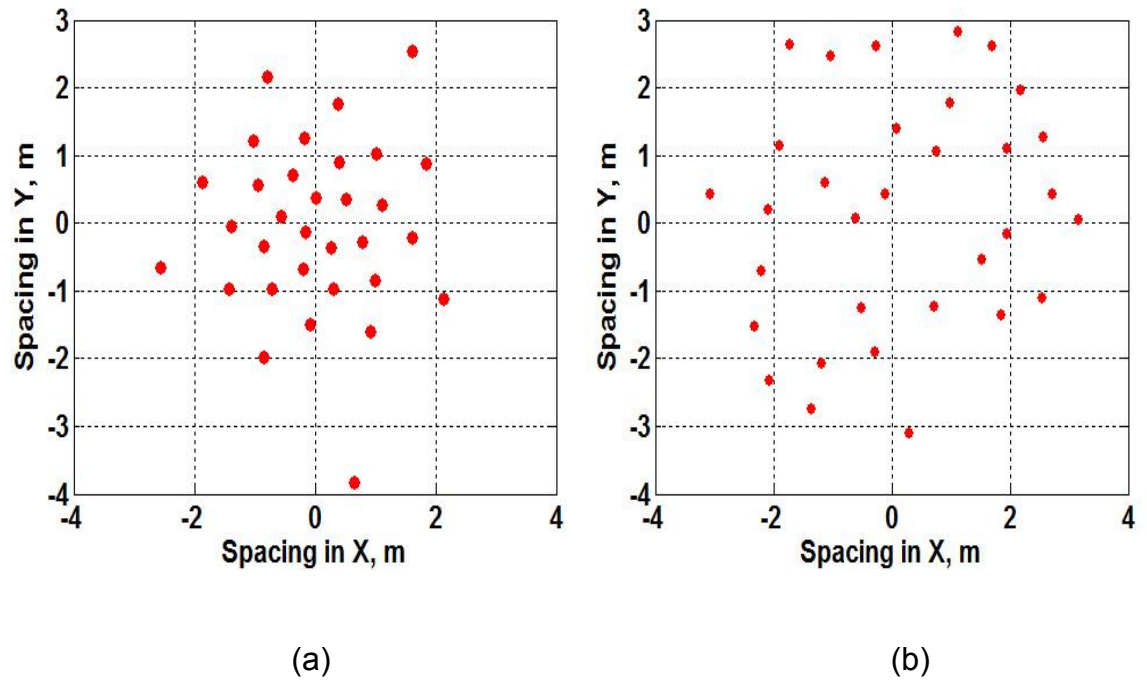


Figure 5.9: Scaled arrays for full wave simulation performance for: (a) 32 elements Tapered Spiral Array (b) 32 elements Random Array.

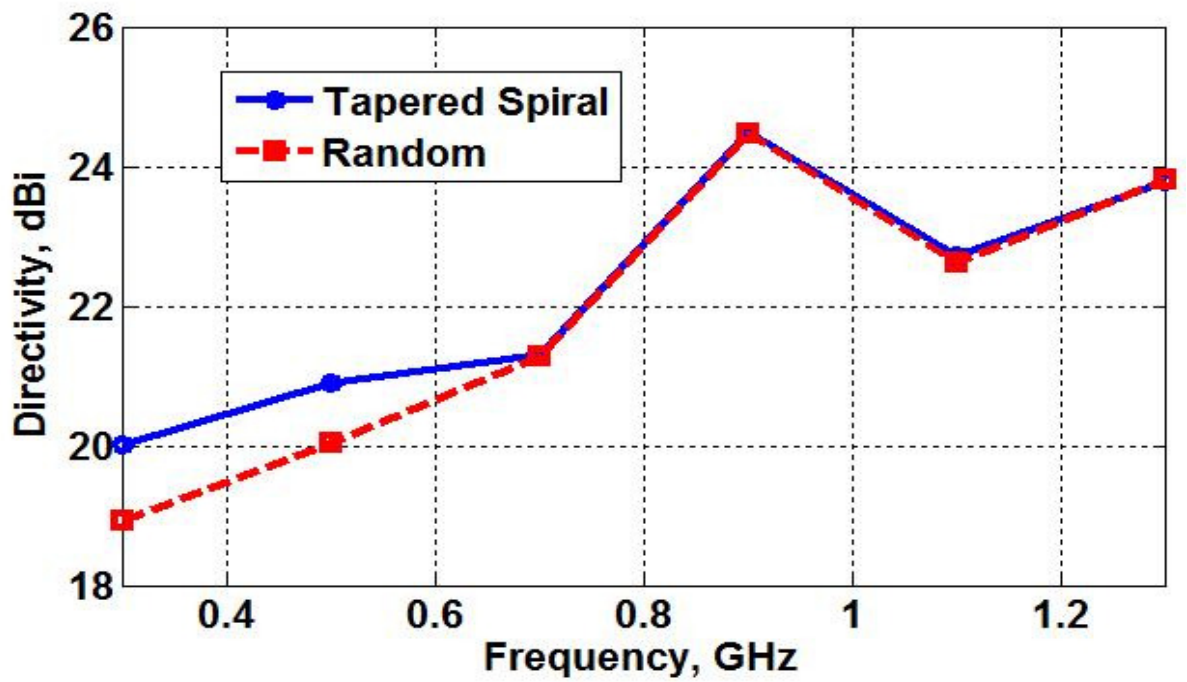


Figure 5.10: Directivity performance for scaled tapered spiral and random arrays

The side lobe performance in figures 5.11-12 show the lower side lobes achieved with the tapered spiral array.

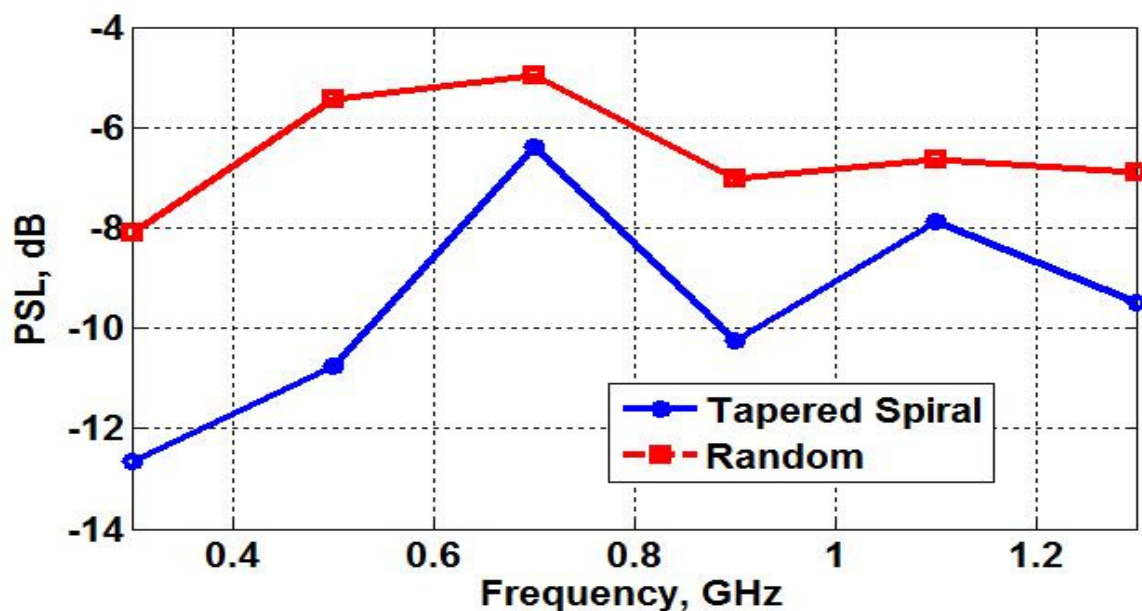


Figure 5.11: Peak side lobe performance for scaled Tapered spiral and Random arrays

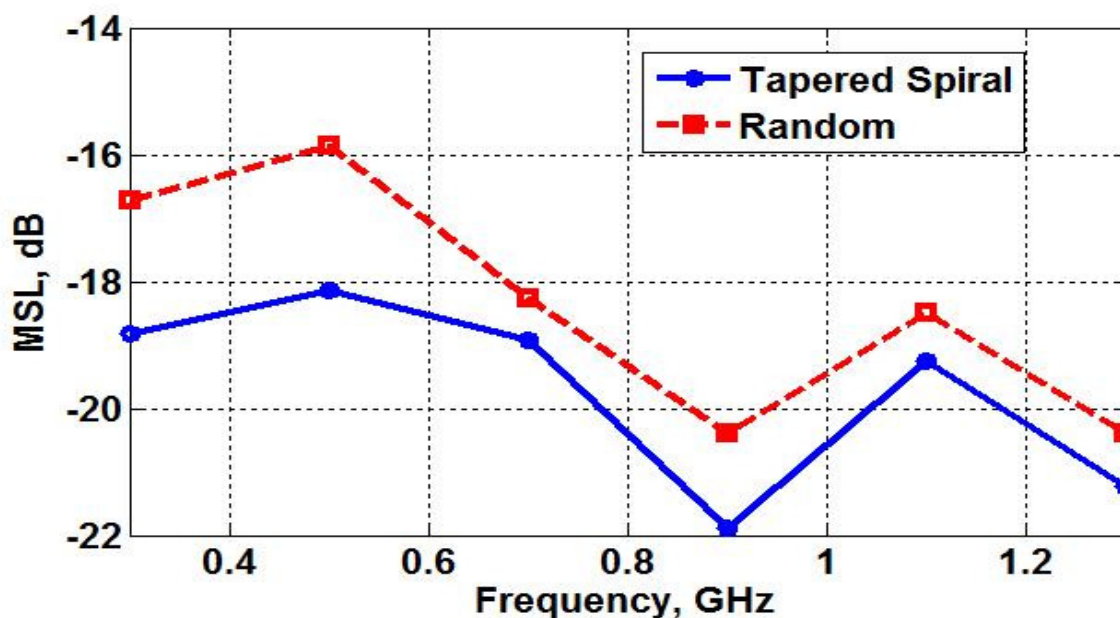


Figure 5.12: Mean side lobe performance for scaled Tapered spiral and Random arrays

The geometry comparisons show that different performance tradeoffs can be achieved for the same number of antenna elements by applying different distributions over the same aperture dimension.

- **Mutual coupling effect**

Similar to the efficiency calculation in the previous section the overall efficiency of the random array is compared with that of the tapered spiral array as well as the isolated element in figure 5.13. The result show a better efficiency achieved with the random array due to larger element separations across the aperture compared to the tapered spiral with its relatively dense centre. This shows that while tapered arrays can provide a better directivity and sidelobes over the band, they might suffer from low efficiency if designed with a minimum separation closer than 0.4λ at the lowest frequency. However, as will be discussed in chapter 8, a lower efficiency might be useful for some applications especially when the resultant antenna noise temperature is significantly higher than the ambient temperature.

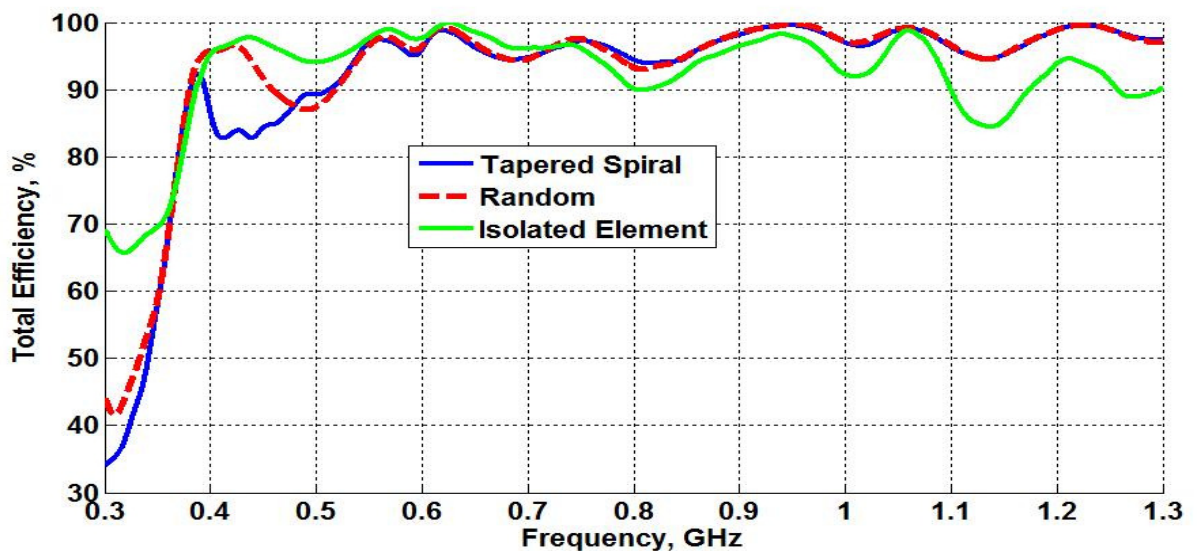


Figure 5.13: Total Efficiency for Isolated element, Tapered spiral and Random arrays.

It is important to note that the geometry performance tradeoffs might not apply if the antenna element radiation pattern contains rapid variations which might cause complex effect on the overall array radiation pattern. Moreover, the mutual coupling effect depends on the antenna element structure as well as separation. Therefore, the efficiency calculation particularly at low frequencies only applies to that particular element.

5.5 Chapter Summary

This chapter considered the scalability and the effect of mutual coupling for two aperiodic geometries. It is shown through full wave simulations that provided the number of elements per unit area remain the same, the arrays and their performances can be scaled to any number of elements and frequency band. In addition, the full wave simulations of two equal apertures and number of elements random and tapered spiral arrays show the advantage of the element distribution in the array in terms of directivity and side lobe performance. In addition, the results show the effect of mutual coupling for different geometries. While closer separation can lead to better directivity and side lobe performance, it might cause a drop in efficiency due to higher mutual coupling effect.

Chapter 6: Beamforming

6.1 Introduction

So far, the study has focused on the impact of different array geometries on the array performance assuming equal amplitude and phase voltages i.e. weights, applied to each antenna element in the array (uniform weights). However, in practice, the performance of the array can be controlled by applying different weights schemes. In general, the aim is to maximize the signal to noise ratio by forming a more optimum patterns where the maximum receive power is directed towards the desired signal/s while reducing the power received by the array in the directions of noise sources. This can be understood by expanding the array factor formula in section 2.2 as:

$$F(\theta, \phi) = \sum_{n=1}^N W(n)A(\theta, \phi)e^{[jk(x_n \sin\theta \cos\phi + y_n \sin\theta \sin\phi)]} \dots \dots (6.1)$$

Where $W(n)$ is the voltage weight at the n^{th} element.

While this is beneficial, changing the amplitude and phase at the element feed point can result in a change in the input impedance particularly in heavy coupling environments. Moreover, the antenna element distribution in the array can change the effectiveness of the weighting scheme.

This chapter studies the effect of simple beamforming algorithms on the performance of the random and tapered spiral array distributions discussed in the previous chapter including full wave simulations.

6.2 Mutual coupling compensation

From section 2.3, the relationship between the voltages at the antenna elements feed point and their currents are related by the mutual coupling matrix $\overline{\overline{M}}$ via:

$$\overline{V} = \overline{\overline{M}} \cdot \overline{I} \dots \dots \dots (6.2)$$

The mutual coupling matrix (or impedance matrix) for an N element array can be obtained by treating the array as N port network and calculating the scattering parameters due to one element being excited, while every other element in the array is terminated with matched load. This process can then be repeated for each element in the array obtaining the scattering matrix $\overline{\overline{S}}$ for the N port network. The impedance matrix $\overline{\overline{M}}$ can then be obtained from the scattering matrix $\overline{\overline{S}}$. The relationship between the scattering and the impedance matrix is given in [52].

Once the mutual coupling matrix is obtained the amplitude and phase of the current flowing on each element due to uniform voltage weights can be determined. Due to the mutual impedances the resultant currents do not have equal amplitude and phase. However, an equal current on each element is required then. The voltage weights corresponding to that current can be determined from equation 6.2

The above has been applied to the 32 elements random and tapered spiral array shown in section 5.2.

Figures 6.1-6 show comparisons between the ideal, uncompensated and compensated radiation patterns for the two arrays at 300, 400 and 500 MHz in both the E and H planes.

The results show poor pattern corrections particularly at 300 MHz for both arrays. A slight improvement is observed in the compensated pattern at 400 and 500 MHz particularly around the main beam.

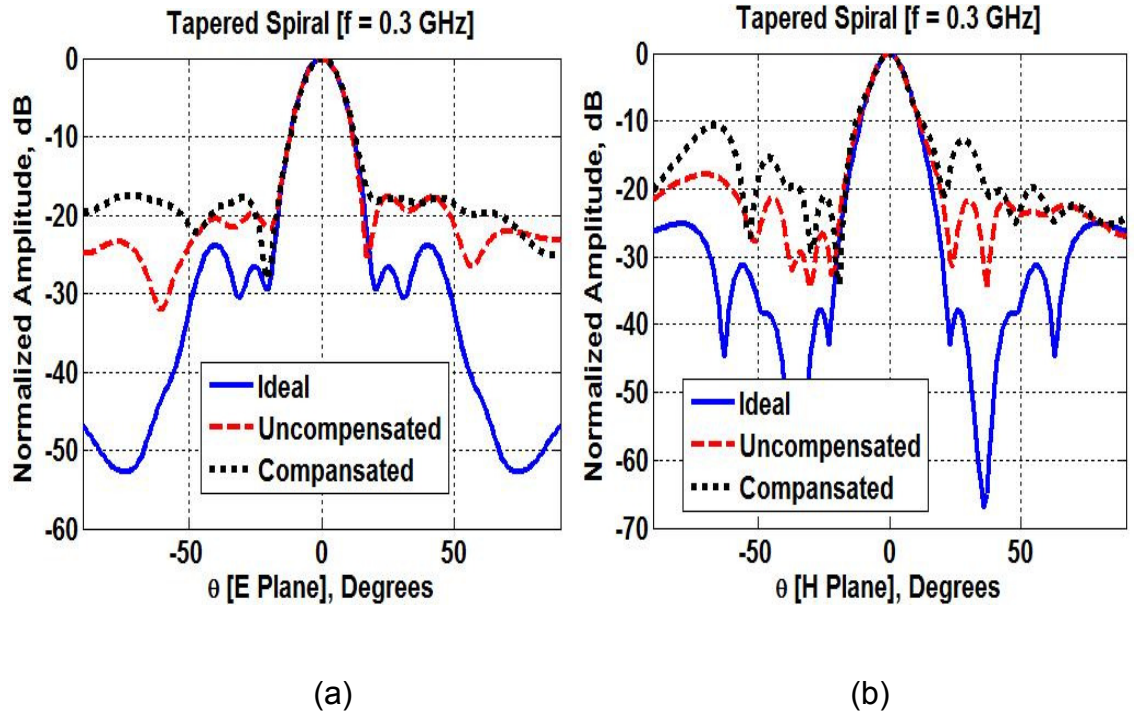


Figure 6.1: Radiation patterns for ideal, uncompensated and compensated tapered spiral at 300 MHz (a) E plane, (b) H plane

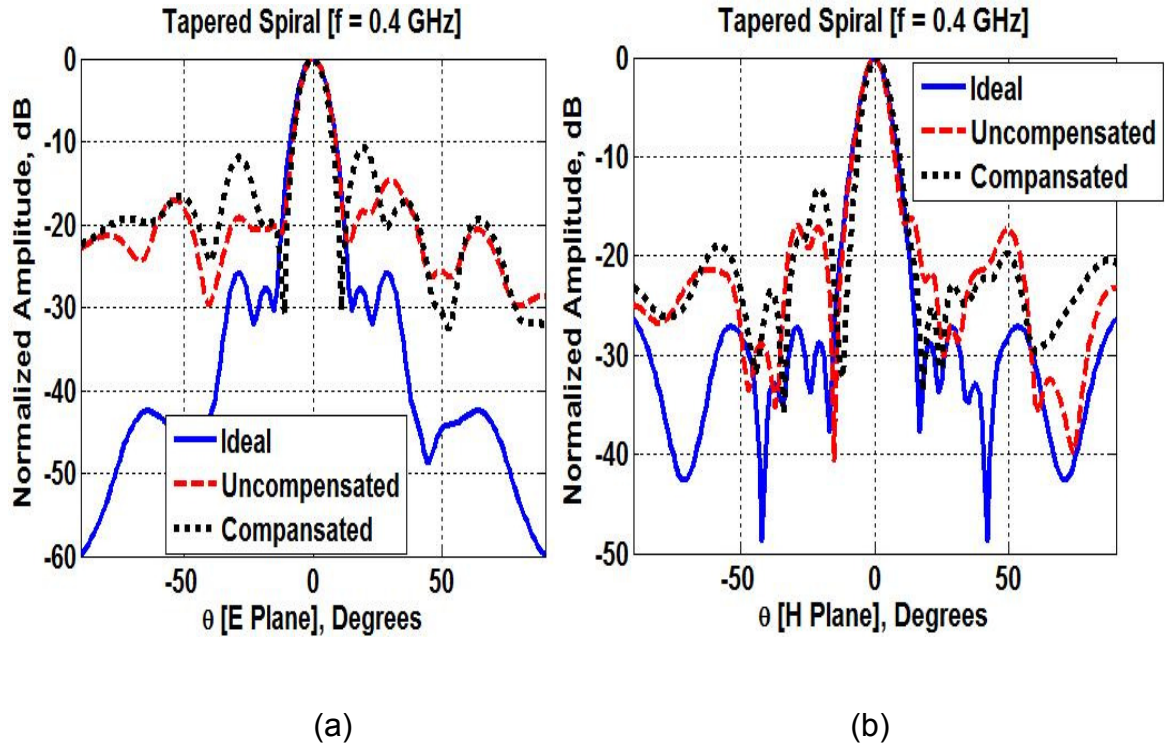


Figure 6.2: Radiation patterns for ideal, uncompensated and compensated tapered spiral at 400 MHz (a) E plane, (b) H plane

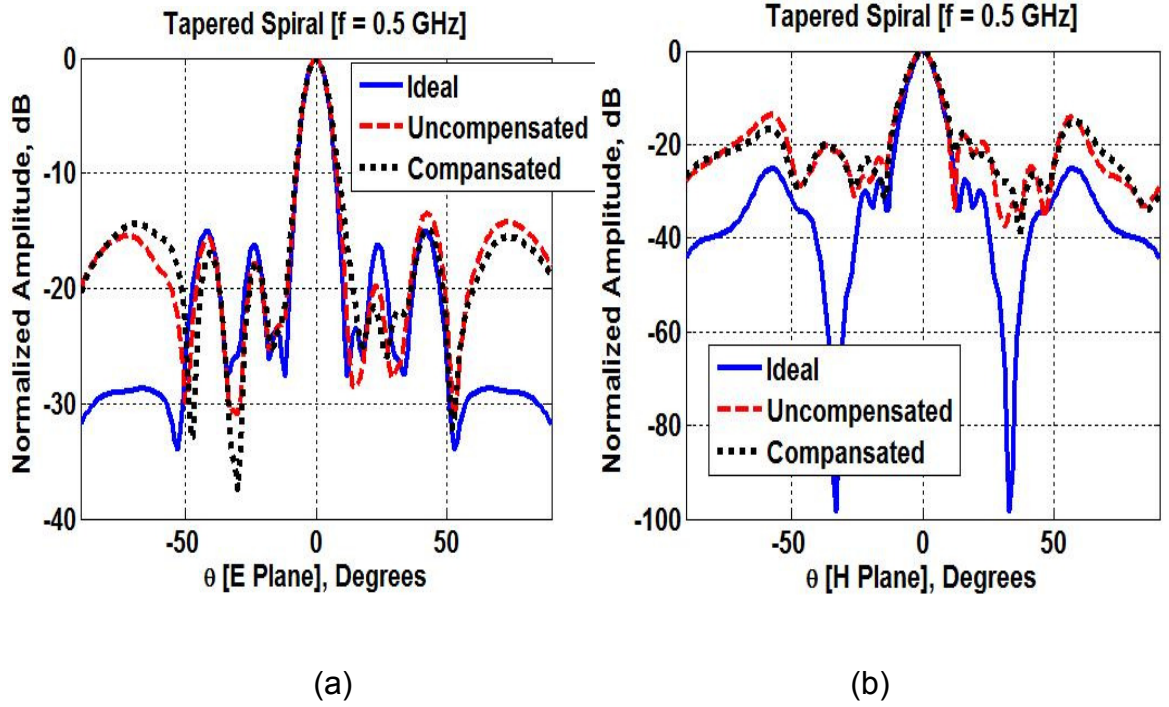


Figure 6.3: Radiation patterns for ideal, uncompensated and compensated tapered spiral at 500 MHz (a) E plane, (b) H plane

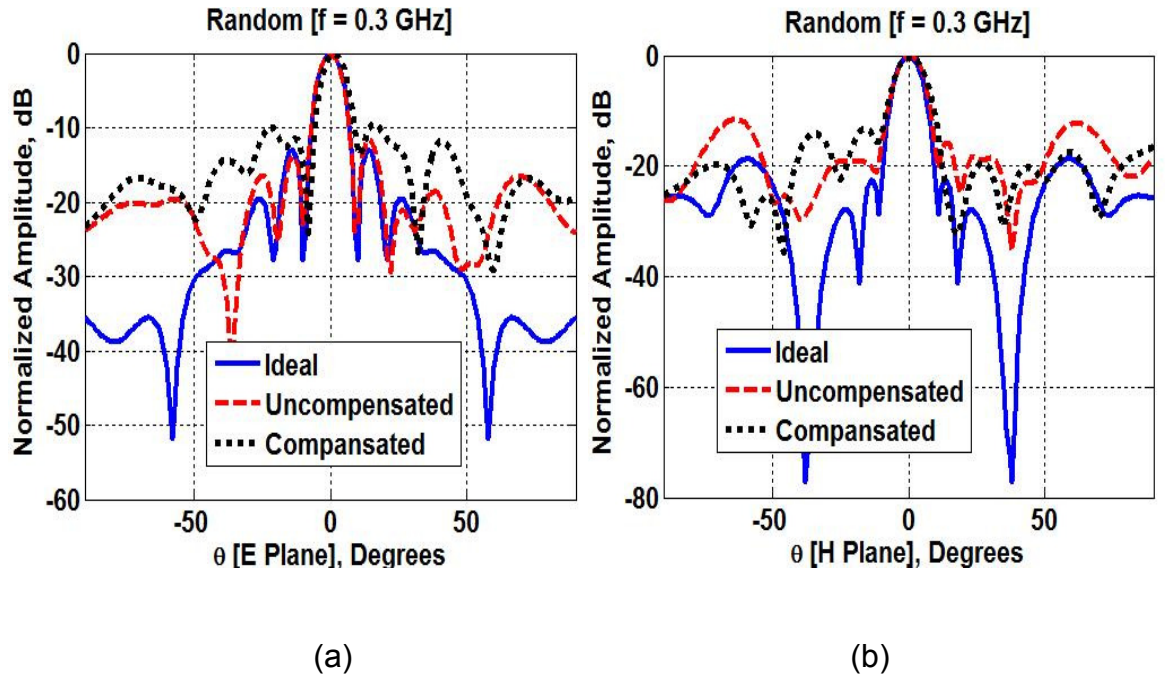


Figure 6.4: Radiation patterns for ideal, uncompensated and compensated random array at 300 MHz (a) E plane, (b) H plane

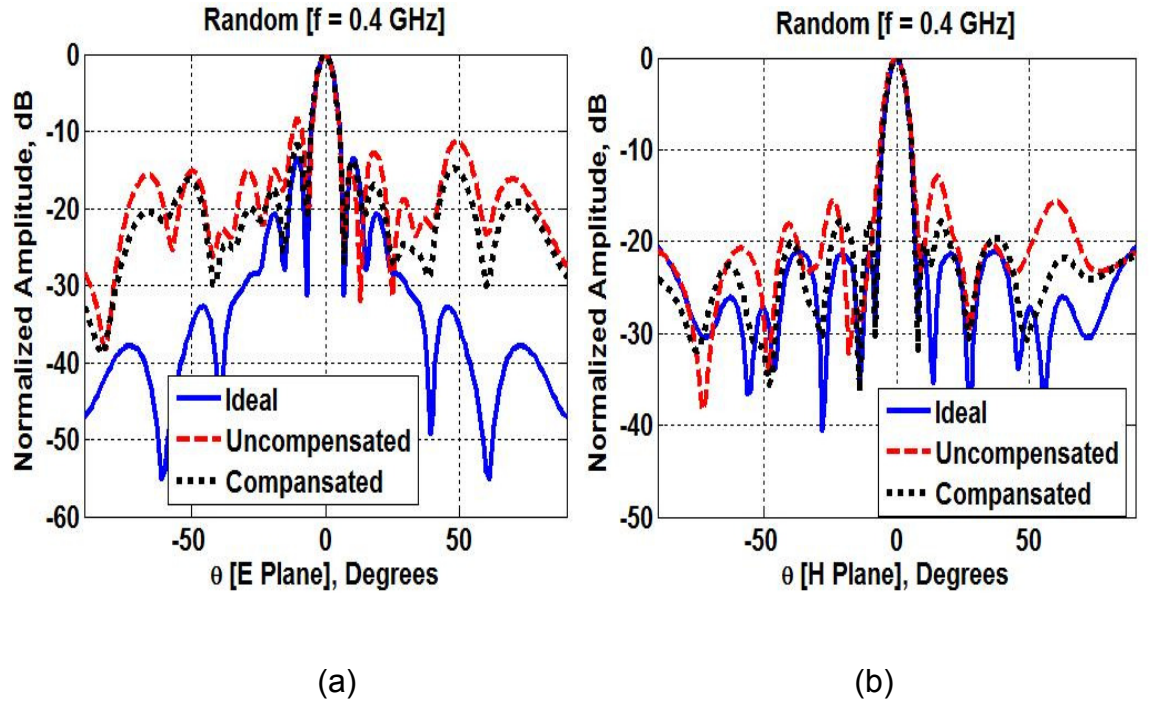


Figure 6.5: Radiation patterns for ideal, uncompensated and compensated random array at 400 MHz (a) E plane, (b) H plane

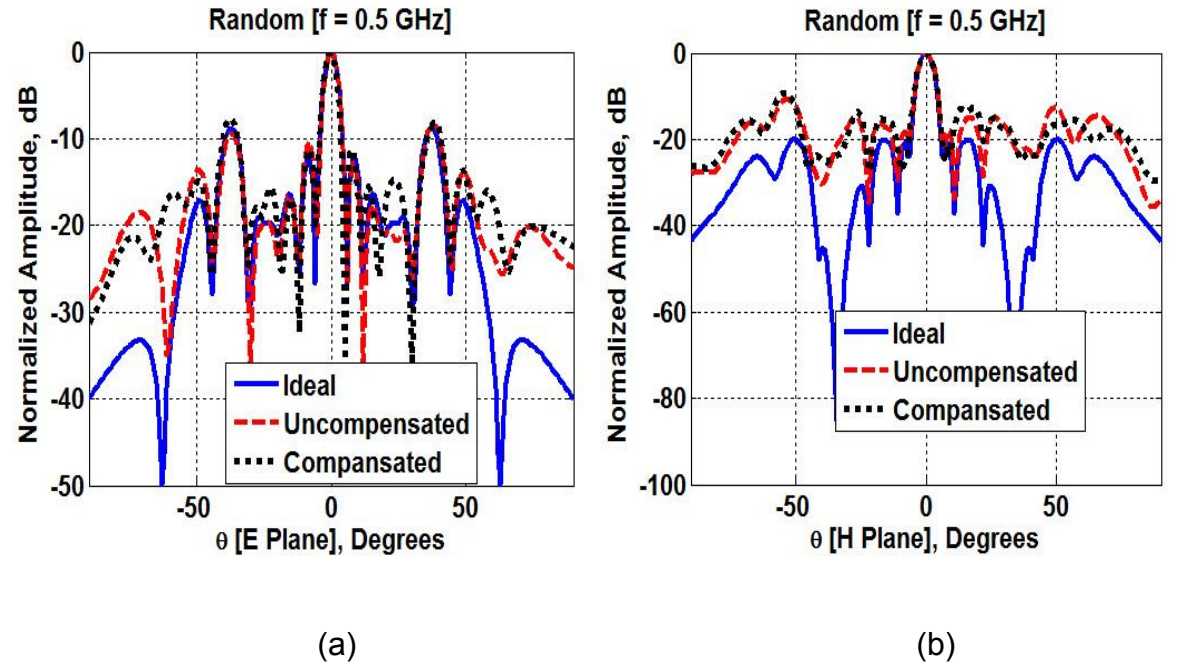


Figure 6.6: Radiation patterns for ideal, uncompensated and compensated random array at 500 MHz (a) E plane, (b) H plane

The above results show the limitation of pattern corrections due to the mutual coupling effect in aperiodic broadband array by means of voltage weight multiplication at the antenna feed point. While this technique can provide reasonable compensation for an array of simple dipole elements [68] due to the simplicity of the current flow, the technique becomes limited when applied to complex broadband antenna elements due to their complex three dimensional structure. This can be visualized by comparing the current flow on the element surface in different coupling environments as well as the isolated element shown in figures 6.7-9 for 300, 500 and 900 MHz.

The result shows significant variations in current flow when compared to the isolated element even for a low mutual coupling environment. This can be observed from the figures where different current components flow on the surface of the elements and not around the edges as in the case of the isolated element. Such variations cannot be controlled by the simplistic approach of voltage compensation weights which merely controls the excitation of the current at the feed point.

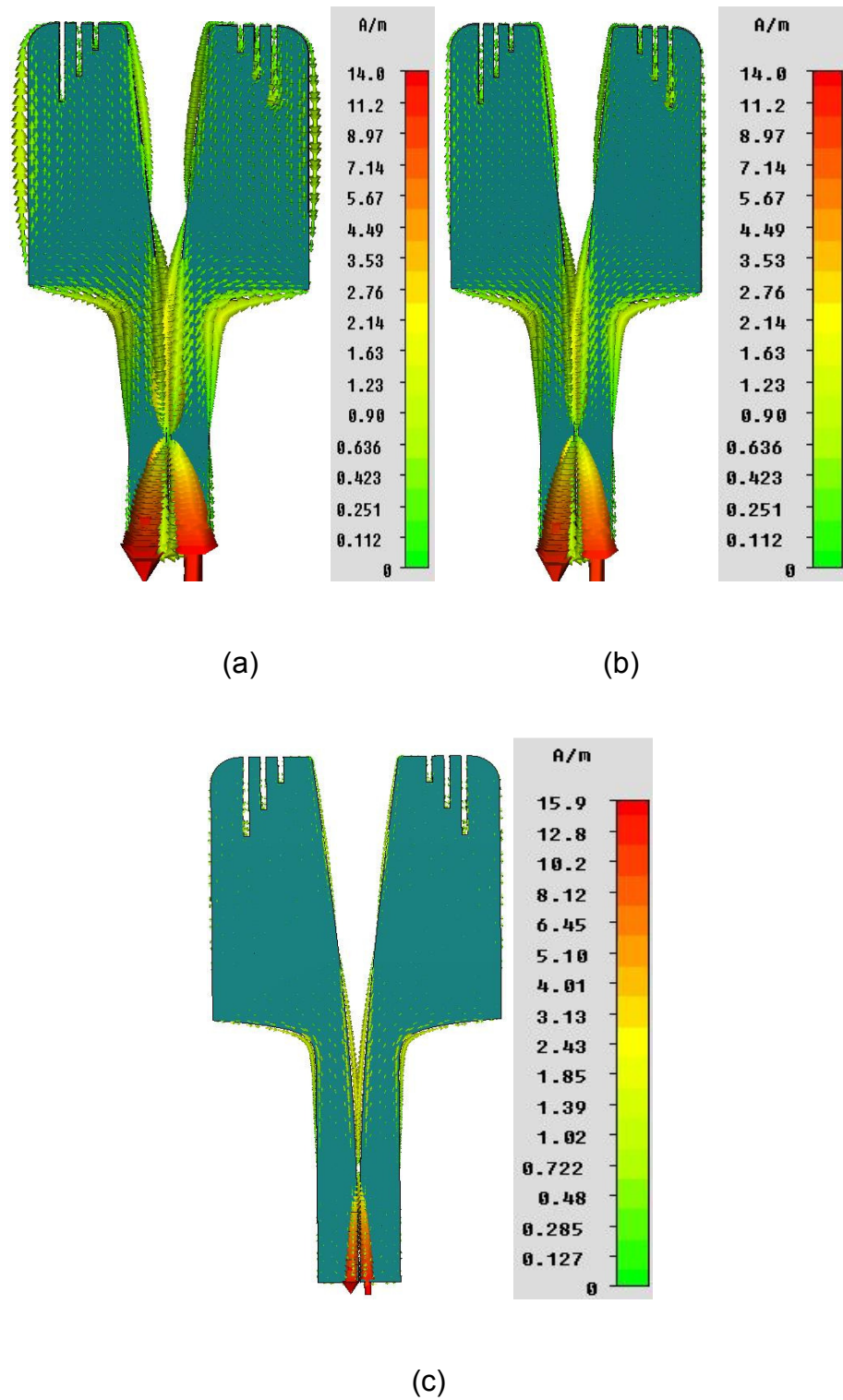
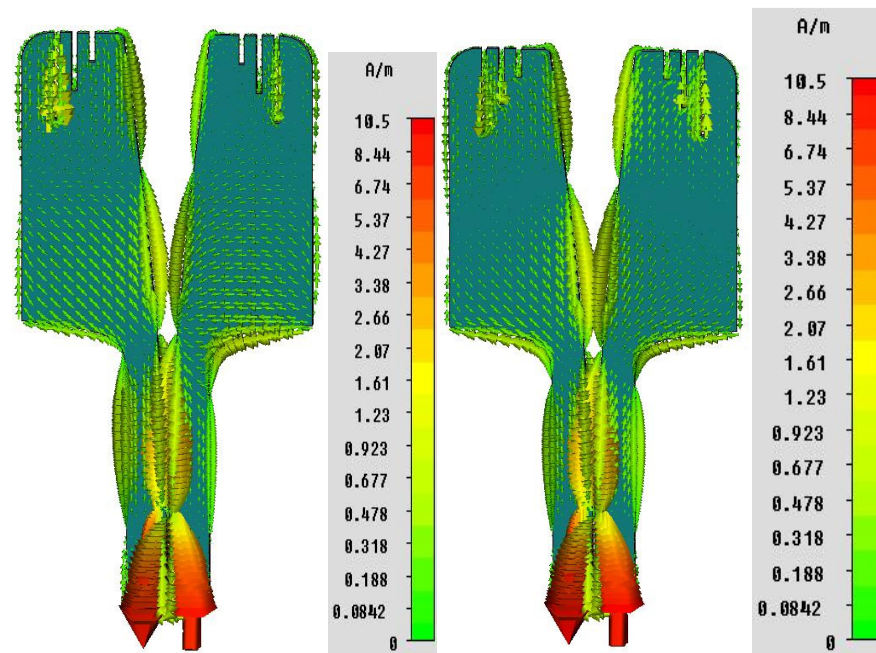
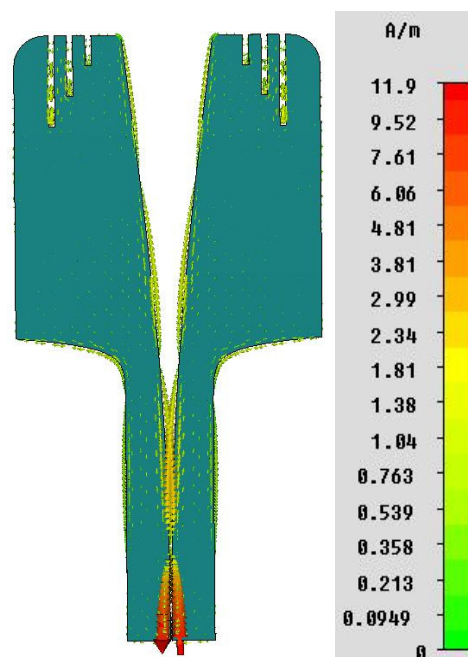


Figure 6.7: Antenna element 300 MHz surface current for different mutual coupling environments (a) high coupling, (b) low coupling, (c) no coupling



(a)

(b)



(c)

Figure 6.8: Antenna element 500 MHz surface current for different mutual coupling environments (a) high coupling, (b) low coupling, (c) no coupling

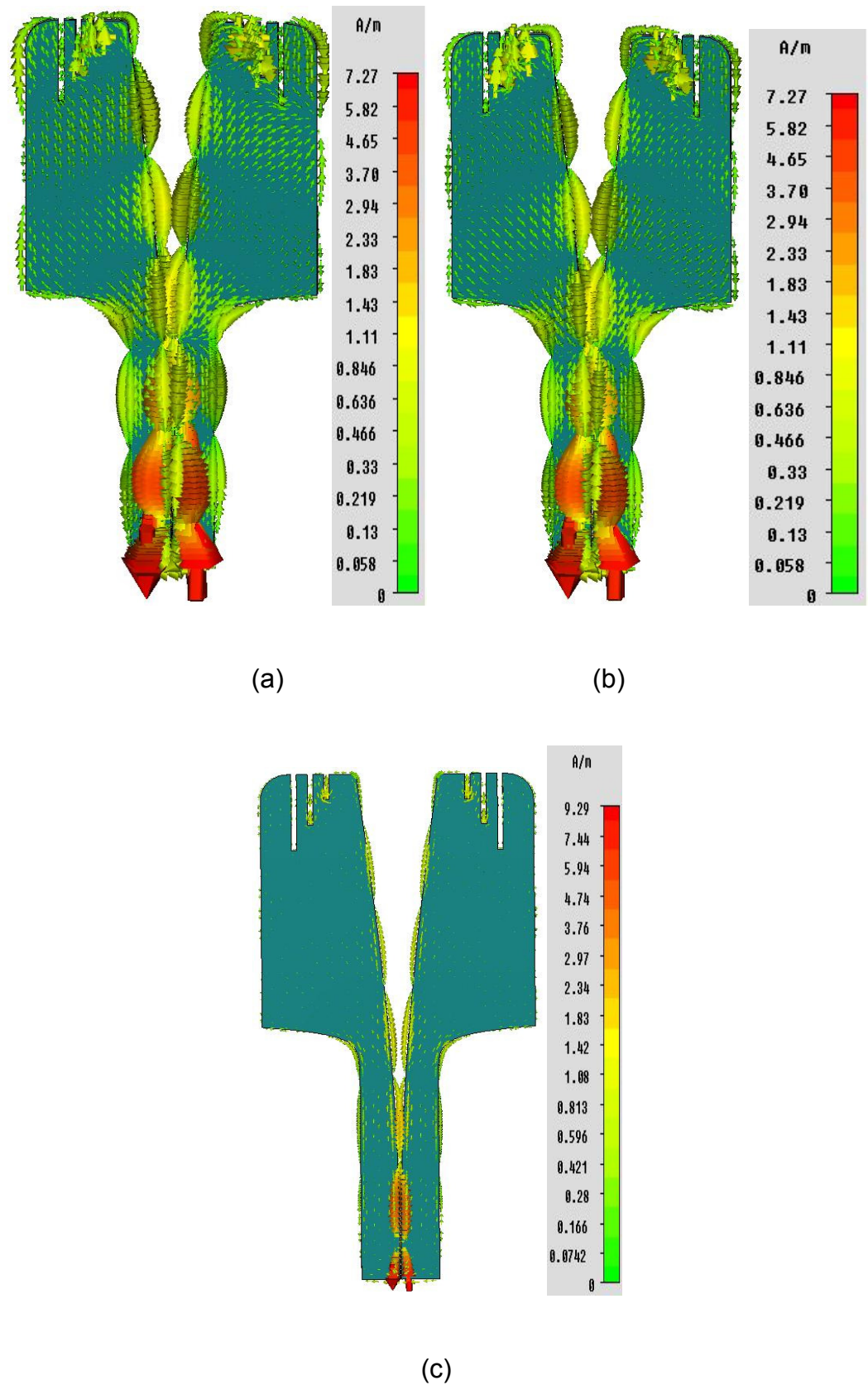


Figure 6.9: Antenna element 900 MHz surface current for different mutual coupling environments (a) high coupling, (b) low coupling, (c) no coupling

6.3 Scanning

One great benefit of phased antenna arrays is the ability to electronically steer the main beam in different directions. This can be achieved by introducing the appropriate phase shift at each element in the array which corresponds to directing the main beam in a certain direction [69]. The value of the phase shift for each element in the array, assuming no mutual coupling is present, can be calculated from:

$$W(n) = e^{[jk(x_n \sin \theta_{scan} \cos \phi_{scan} - y_n \sin \theta_{scan} \sin \phi_{scan})]} \dots \dots \dots (6.3)$$

Where θ_{scan} and ϕ_{scan} are the angles of the desired scan direction, x_n and y_n are the coordinates of the n^{th} element and k is the wave number. The details of antenna array scanning are given in [69].

The effect of element spacing on the array scanning performance can be crucial. For instance, a periodic array must have a minimum spacing to prevent the appearance of grating lobes in real space at the maximum required scan angle. This due to the periodicity discussed in section 3.2 where the array factor has maxima at $k d \sin \theta = 2m\pi$, where $m = 0, \pm 1, \pm 2 \dots$. Subsequently the minimum separation required to avoid grating lobes at a maximum scan angle θ_{scan} in a periodic array must satisfy the relationship:

$$d \leq \frac{\lambda}{1 + |\sin \theta_{scan}|} \dots \dots \dots (6.4)$$

For large scale periodic arrays, the narrower grating lobe allows for a slight increase in the minimum separation without causing its appearance in real space [69].

In the case of aperiodic arrays where no grating lobes are formed even at larger element separations, the effect of scanning causes increase in the side lobe level which continue to rise for wider scan angles. It is essential to take into account the effect of the element pattern on the scan performance. In addition to the drop of the array directivity due to the resultant broader main beam, the directivity and sidelobes are also affected by the element pattern particularly in the scan direction. A low power in the scan direction can significantly reduce the overall directivity of the array.

The effect of a 30 degree scan on the performance of random and tapered spiral array with 1000 hemispherical elements are shown in figures 6.10-12. The results show a drop of directivity by around 0.7 dB and an increase in the mean side lobe by the same magnitude. The scanning does not affect the peak side lobe level in the case of a random array as it remains at the level of the first side lobe of -17dB, figure 6.11. However, for the tapered spiral array where the peak side lobe level is due to side lobes at wider angles, the scanning causes increase in peak sidelobe level by 2 to 5 dB over the band.

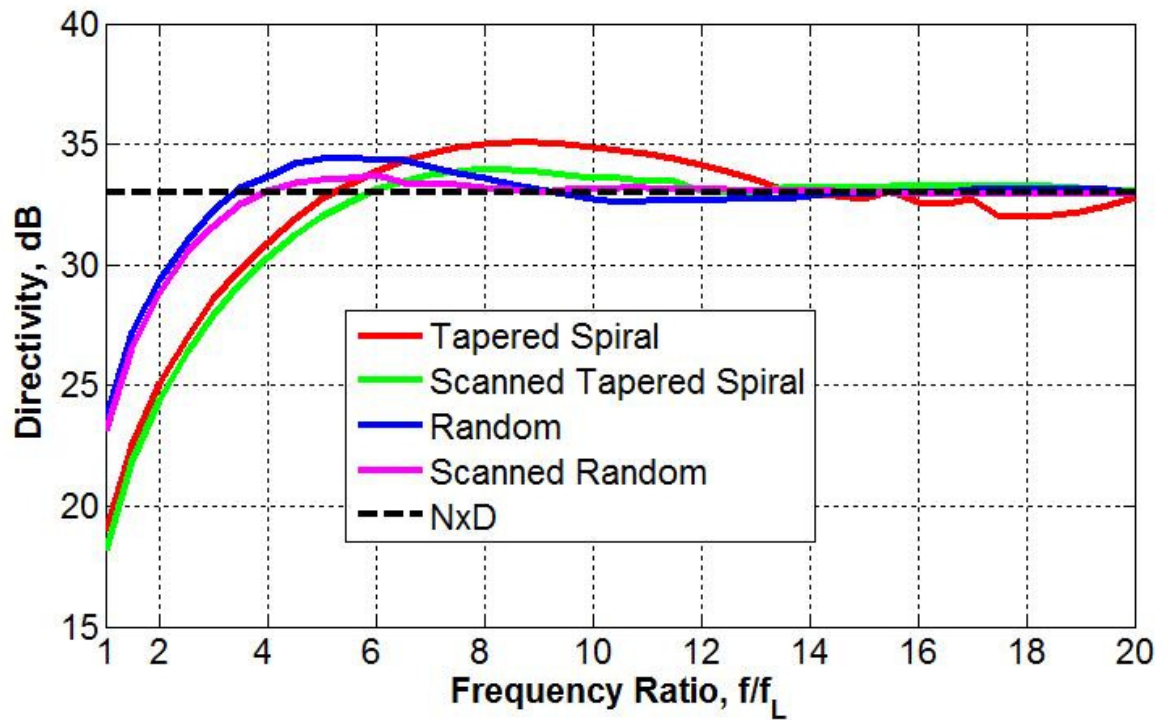


Figure 6.10: Directivity performance for random and spiral arrays with 30 degrees scan angle (1000 hemispheric elements)

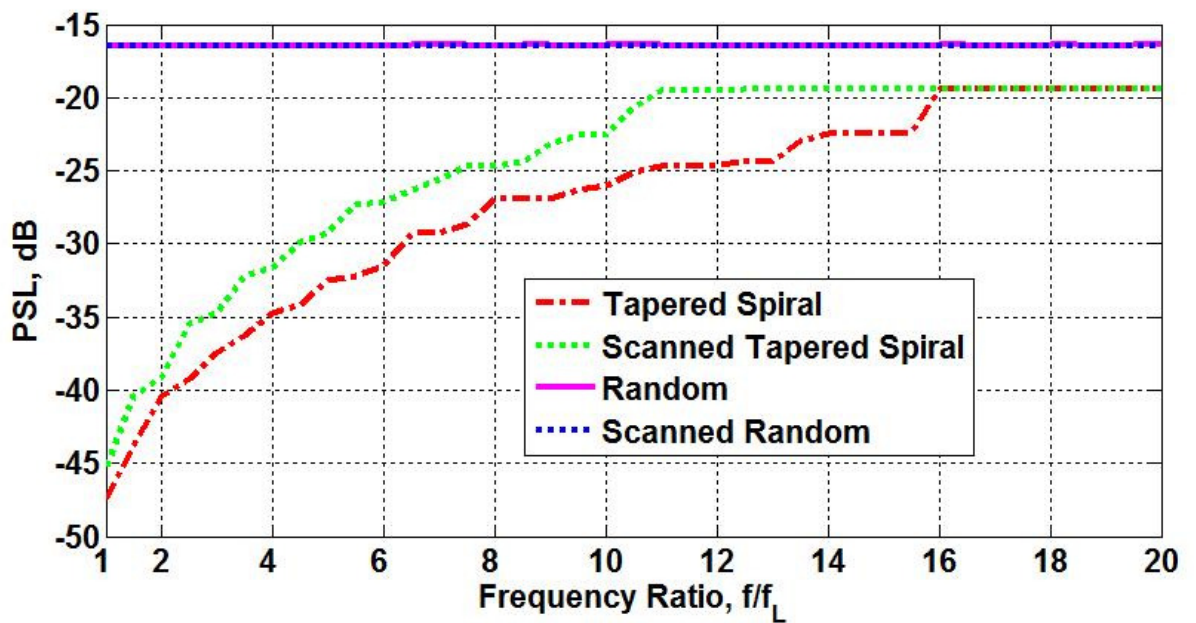


Figure 6.11: Peak sidelobe performance for random and spiral arrays with 30 degrees scan angle (1000 hemispheric elements)

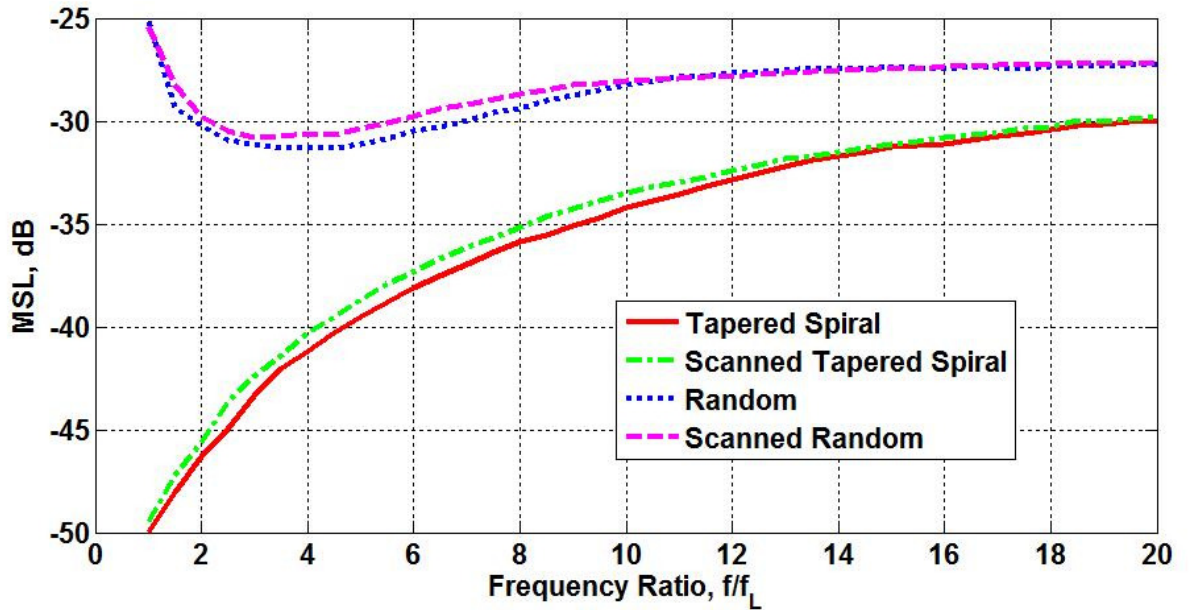


Figure 6.12: Mean sidelobe performance for random and spiral arrays with 30 degrees scan angle (1000 hemispheric elements)

The above shows the effect of scanning for aperiodic geometries assuming constant idealized element patterns. However, as stated above, the element radiation pattern plays a major part in the scan performance. This shown here for a full wave simulation of the 32 element random and tapered spiral arrays designed in section 5.3 with 30 degrees scan angle in the H plane using the tapered slot fork antenna from section 2.3.

The results for directivity and side lobe levels are shown in figures 6.13-6.15. The results show the tapered spiral array to retain the better directivity and side lobe performance over the band for both boresight and scan angle.

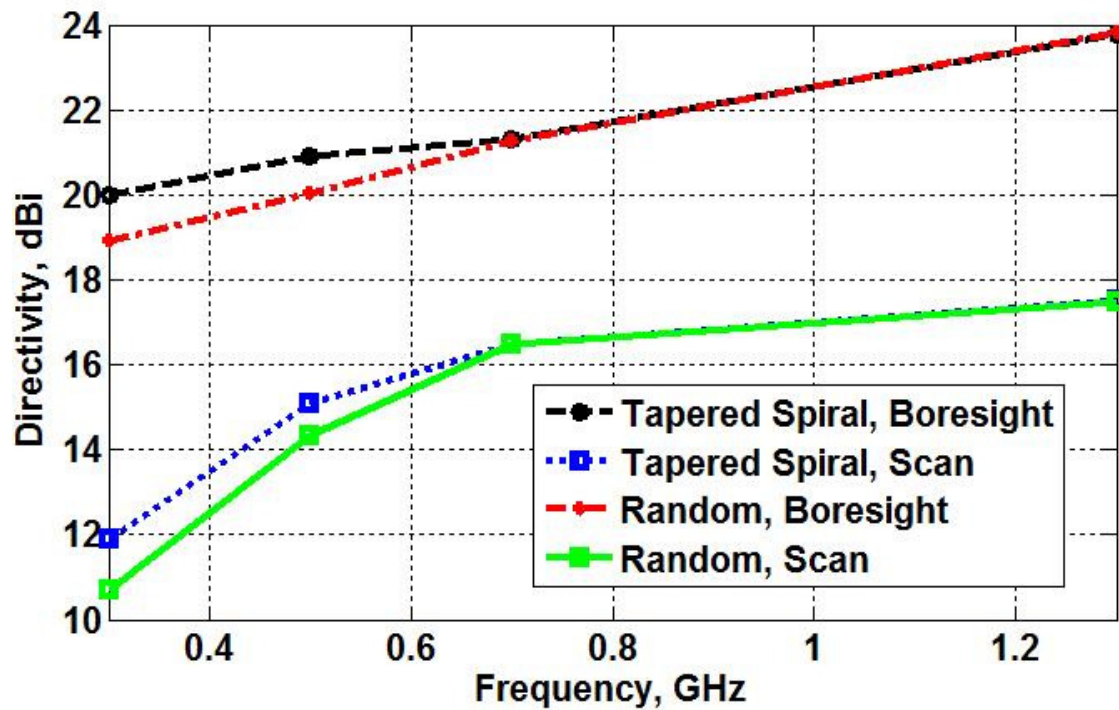


Figure 6.13: Directivity performance for random and spiral arrays with 30 degrees scan angle (full wave simulation)

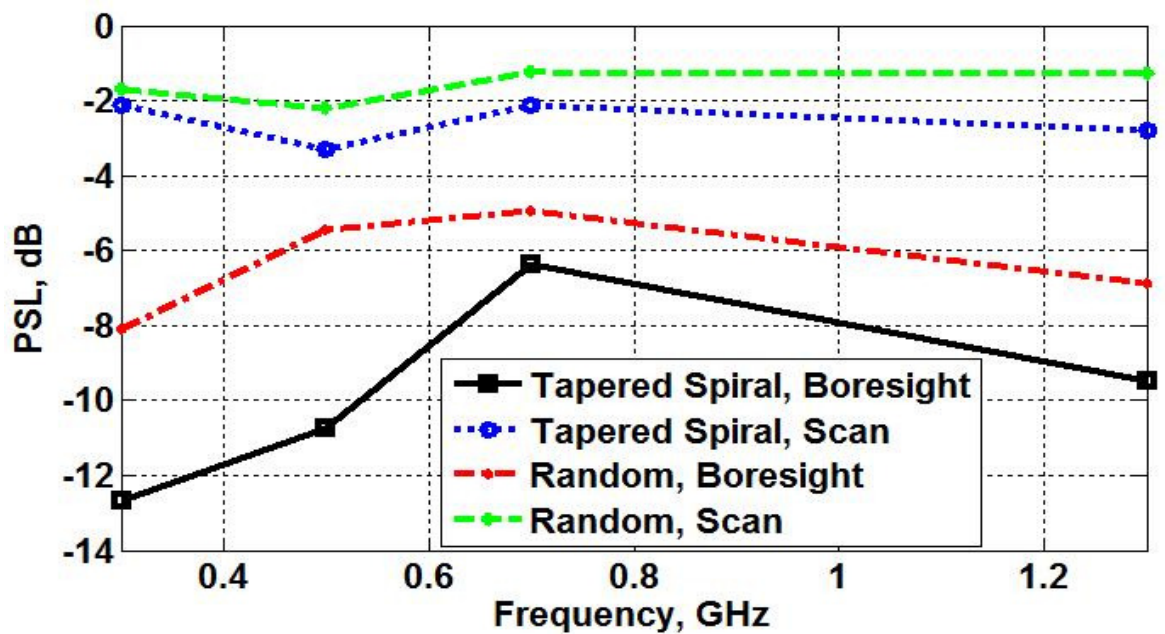


Figure 6.14: Peak sidelobe performance for random and spiral arrays with 30 degrees scan angle (full wave simulation)

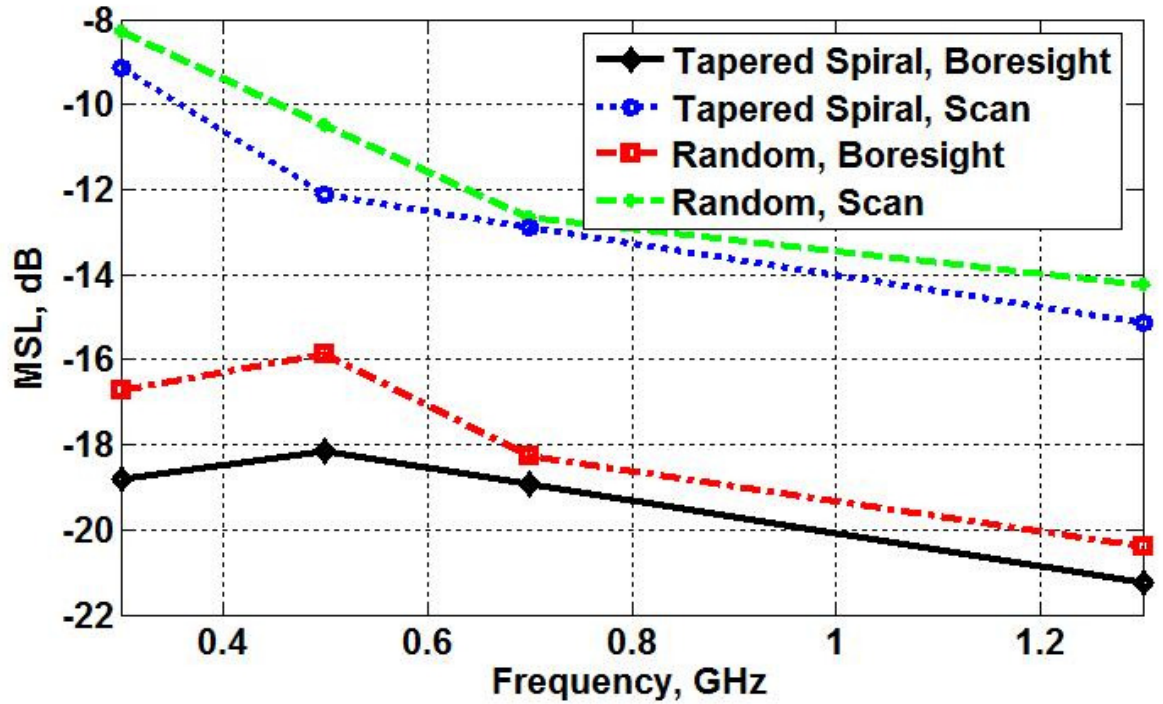


Figure 6.15: Mean sidelobe performance for random and spiral arrays with 30 degrees scan angle (full wave simulation)

6.4 Amplitude Taper

A common beamforming approach is applying different relative amplitude for each element in the array according to a certain taper distribution¹¹ such as a Gaussian, Taylor etc. In well sampled equally spaced arrays such a scheme can result in a specific side lobe level provided by the amplitude distribution window. However, this often comes at the expense of broadening the main beam resulting in a lower directivity [43]. For sparse irregular arrays, this technique becomes limited due to their under-sampling and their non uniform distributions which require a more optimum solution for the amplitude weights [39].

¹¹ It is essential to differentiate between space tapering (used previously to refer to element position tapering) and amplitude tapering in this section referring to voltage weight tapering.

The effect of a 25 dB side lobe Taylor distribution is applied to the 32 element random and tapered spiral arrays for full wave simulations. The results for the directivity and side lobe performance are shown in figures 6.18-6.20.

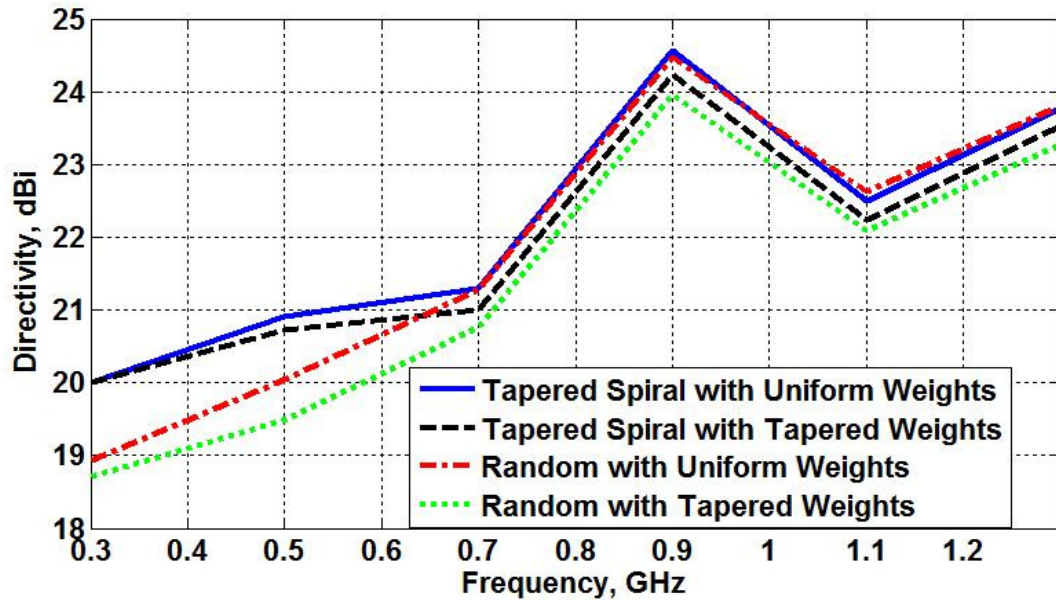


Figure 6.18: Directivity performance for scaled random and spiral arrays with amplitude taper

The results show a drop in the array directivity in addition to drop in both mean and side lobe level for both arrays due to the amplitude tapering as expected. However, the tapered spiral array with the tapered weights show a more sensitivity to the effect of applying amplitude taper weights in terms of reducing side lobe levels. This is due to the closer element separation particularly in the center of the tapered spiral compared to the random array. Nonetheless, the effect of amplitude tapering on both arrays, shown in figures 6.21-22, show a slight drop in the overall efficiency at lower frequencies in the case of the tapered spiral while the random array efficiency remains unchanged. This is due more relative power being applied to the more inefficient center elements caused by the mutual coupling.

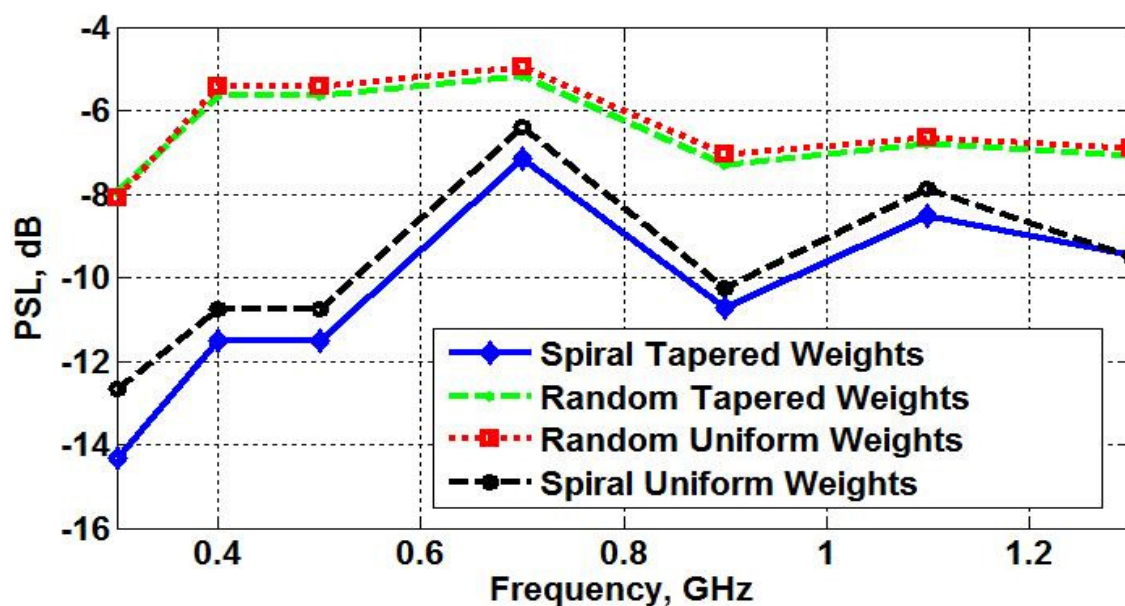


Figure 6.19: Mean sidelobe performance for scaled random and spiral arrays with amplitude taper

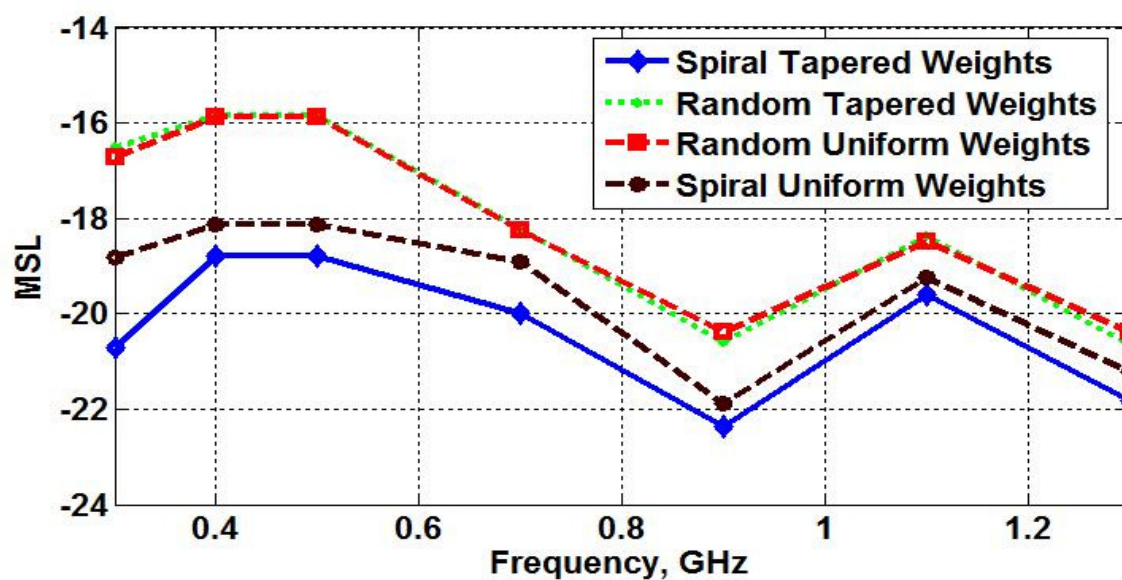


Figure 6.20: Mean sidelobe performance for scaled random and spiral arrays with amplitude taper

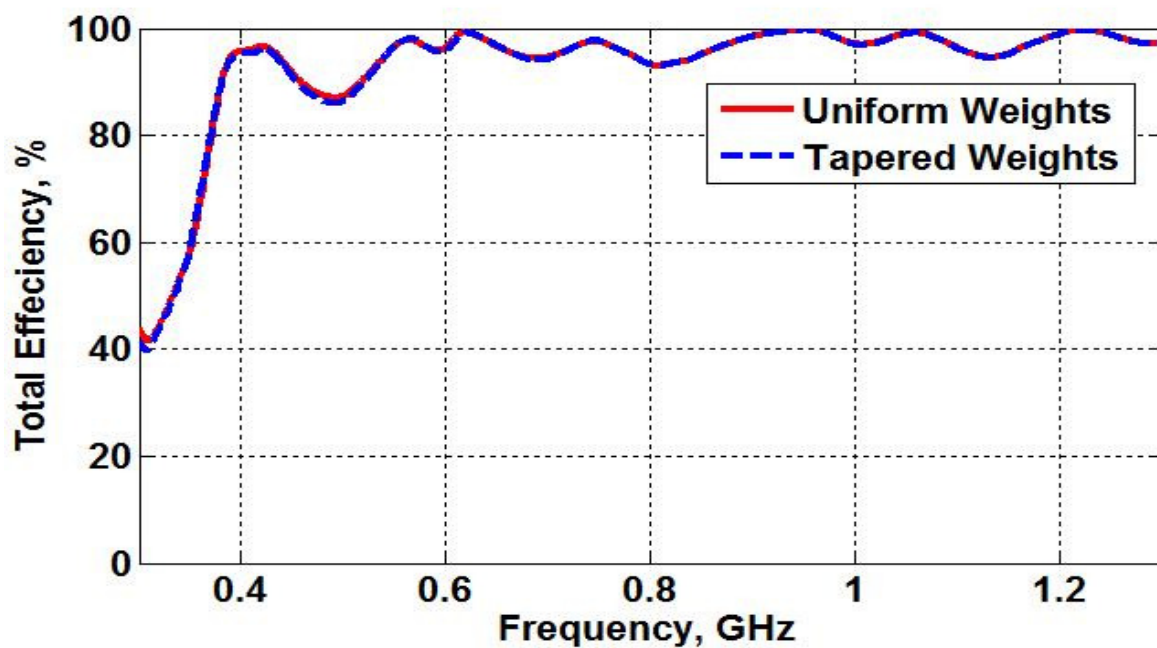


Figure 6.21: Total Efficiency for random array with uniform and tapered weights

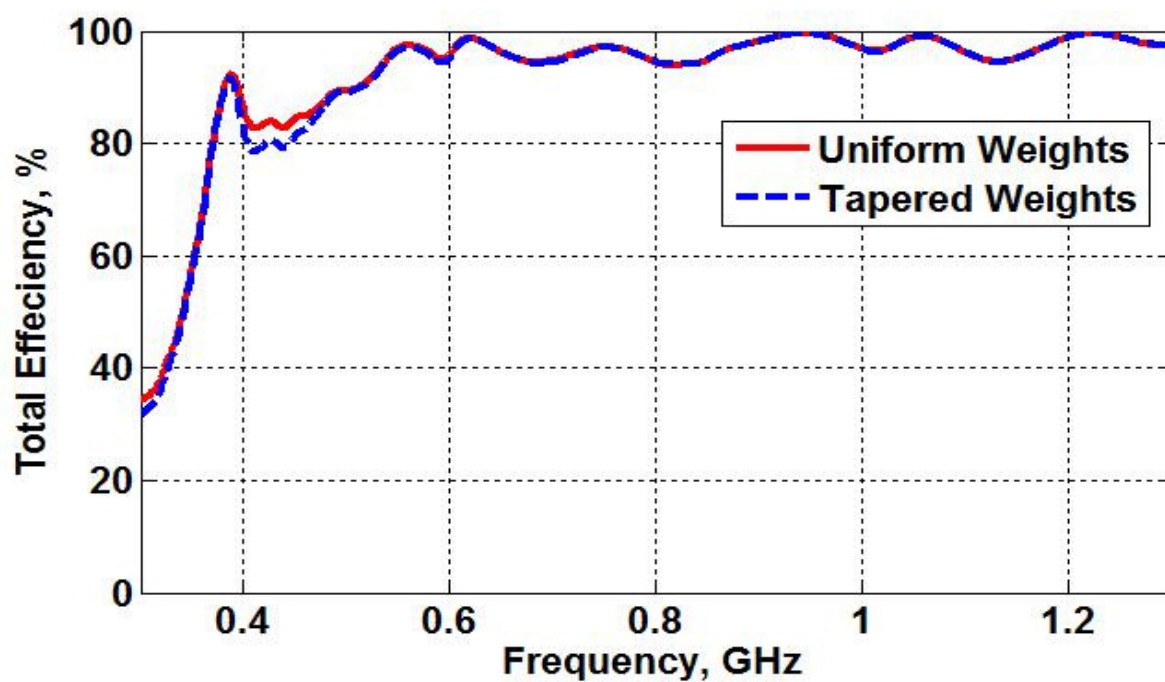


Figure 6.22: Total Efficiency for tapered spiral array with uniform and tapered weights

6.5 Chapter Summary

This chapter considered the impact of simplistic beamforming techniques on the performance of a random and tapered spiral arrays. This included mutual coupling compensation, scanning and beamforming.

Due to the complexity of the broadband antenna element structure, in addition to the complexity of the overall array, the mutual coupling compensation by means of voltage weights is limited, and a full compensation could not be achieved. The scanning of the two arrays has also been considered where a drop of directivity and an increase in the side lobe level is caused by the antenna element pattern loss at the scan angle in addition to a factor of $\cos\theta_{scan}$ effect. However, the tapered spiral geometry maintains its higher directivity and lower sidelobes compared to the random array. A better response to amplitude taper in reducing sidelobes is also observed in the case of the tapered spiral array. Due to the higher mutual coupling in the centre of the tapered spiral array, the total array efficiency drops as a result of the amplitude taper which applies more relative power to elements in the centre of array.

CHAPTER 7: Experimental Model

7.1 Introduction

The Geometry study in chapter 3 and 4 show the advantage of array element distribution in optimizing the performance of antenna arrays. The optimized geometries can be scaled to any number of elements and frequency band as shown in chapter 6. This allowed for a possible geometry comparison with smaller and therefore more computationally manageable size arrays. This also allows the possibility of a realistic experimental measurement with the objective of verifying the array geometry effect on the radiation pattern. It is emphasised that the aim of this experiment is to verify the geometry effect on the array radiation pattern and not its bandwidth.

The chosen optimized geometry, the number of elements and the operating frequency were chosen to allow for a reasonable far field measurement within the size constraint of the available anechoic chamber (a maximum range of 5 meters). The main cost and complexity lies in the power divider network and the associated cabling which in general increase for higher frequencies. Moreover, since radiation pattern measurement is the main interest for this experiment, the array is preferred to have low mutual coupling effect in order to avoid its effect on the radiation pattern. The large element separation implies a larger aperture size exerting an extra constraint with respect to far field measurements. From these constraints,

the chosen geometry configuration is a 32 element exponentially tapered golden angle spiral. This geometry is discussed in section 4.3.1 where the corresponding array obtains a first side lobe level of -22 dB. The chosen frequency is 5 GHz with an aperture diameter D_{ap} of 6.52λ or a far field distance $\frac{2D_{ap}^2}{\lambda}=5.1$ meters. The detail design and tradeoffs are discussed in the following sections

7.2 Element design

The antenna element of choice is a printed dipole with an adjustable integrated balun proposed in [53] where it has been redesigned here for the required 5 GHz operating frequency. This dipole antenna design is simple, and requires no additional balanced feed or external impedance matching to the feed point. The antenna has been reported in [53].

The antenna is fabricated on a dielectric substrate of dielectric constant of 2.33. The material is PTFE (RO5870 from Rogers Cooperation [54]) with copper on either side with a thickness of 0.381mm. The redesigned antenna is shown in figure 7.1 where the dipole is fabricated on one side while the balun is fabricated on the other. The antenna dimensions are shown in table 7.1. The dipole arms are short circuited with the ground plane and the antenna is fed through a hole in the ground plane with an SMA connector as shown in figure 7.1

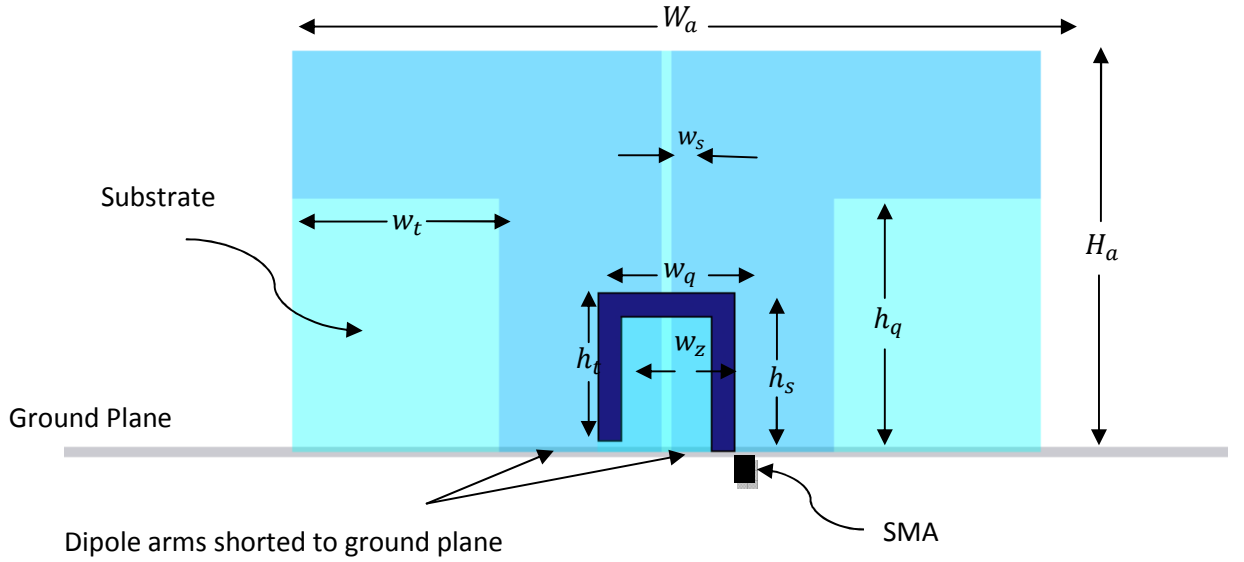


Figure 7.1: Printed dipole with integrated balun

Dimension	W_a	w_z	h_s	w_q	H_a	w_t	h_t	w_s	h_q
Value, (mm)	29	3.26	6.07	5.54	15	8	5.69	0.381	9.5

Table 7.1: Antenna dimensions

The integrated balun is designed to have an impedance of 50Ω to match the feed line and the antenna is simulated using CST microwave studio. The return loss is shown in figure 7.2 where it shows consistency with the characteristic of the return loss for the dipole antenna in [53].

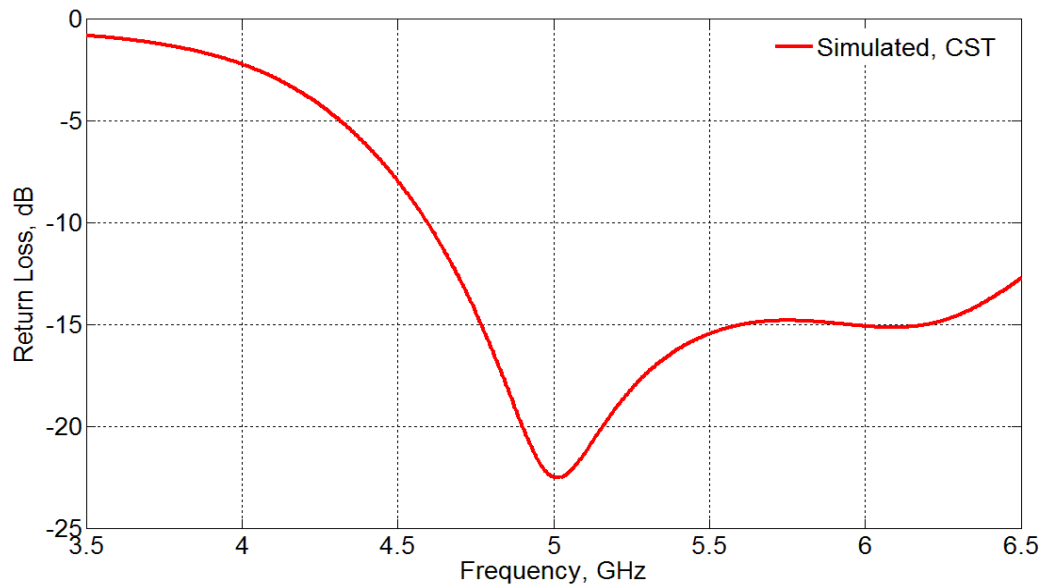


Figure 7.2: Simulated dipole element return loss

The antenna is resonant at 5 GHz with a return loss of -23dB.

7.3 Array design

The array is designed by distributing 32 dipole elements according to the golden angle spiral configuration with a golden ratio conjugate exponential tapering (See section 4.3.1). Initially, the array is designed with a large minimum separation to avoid mutual coupling and avoid any mismatch. The large minimum separation increases the size of the aperture beyond the far field of the available anechoic chamber. Therefore, the array size is gradually scaled down bringing elements closer together where the mutual coupling effect increasingly changes the impedance of each element as they get closer and subsequently increases the return loss.

The printed dipoles balun can be in principle adjusted to reduce the mismatch effect and improve the return loss. Due to the irregular geometry the coupling effect on each element performance varies from element to element, so that each

element will have to be designed individually. This additional complexity would considerably complicate the design. Accordingly, the design was modified to reduce the mutual coupling allowing the same element to be used throughout the array. A reasonable array size for far field measurements was obtained with a minimum separation of 0.77λ without a significant mutual coupling effect.

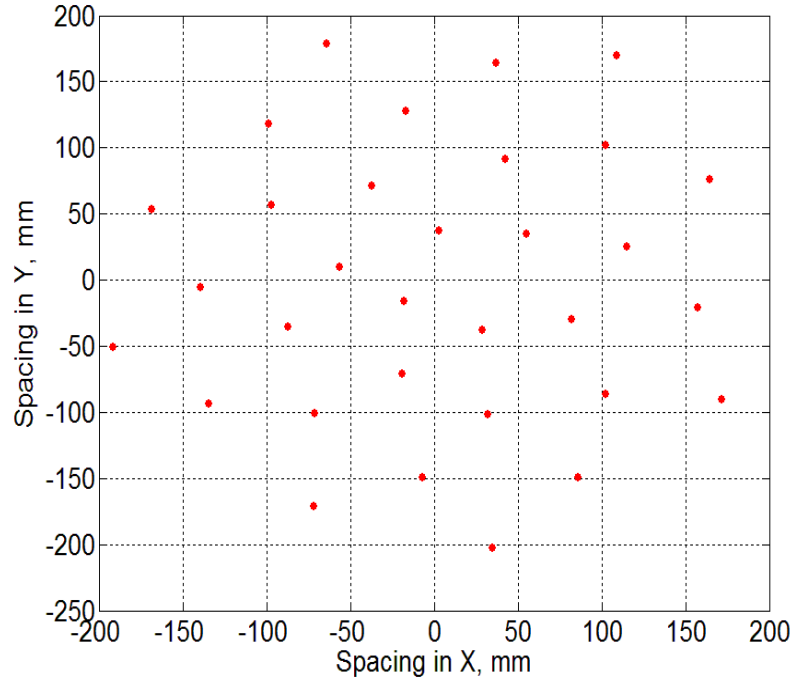


Figure 7.3: Array geometry

The array geometry is shown in figure 7.3. The array has 32 elements with a minimum separation of 0.77λ , a maximum separation of 1.16λ and an aperture diameter of 6.52λ . The minimum far field distance is defined at $2D_{ap}^2/\lambda$, where D_{ap} is the diameter of the array [32]. For the designed array the far filed distance is equal to 5.1 meters.

The array is simulated using CST microwave studio and the return loss for each element in the array is shown in figure 7.4. The return loss shows how some

elements matching are degraded due the mutual coupling effect. However, as mentioned earlier the design was intended to avoid significant mutual coupling effect. The minimum return loss on any one element is maintained below -10dB at 5GHz.

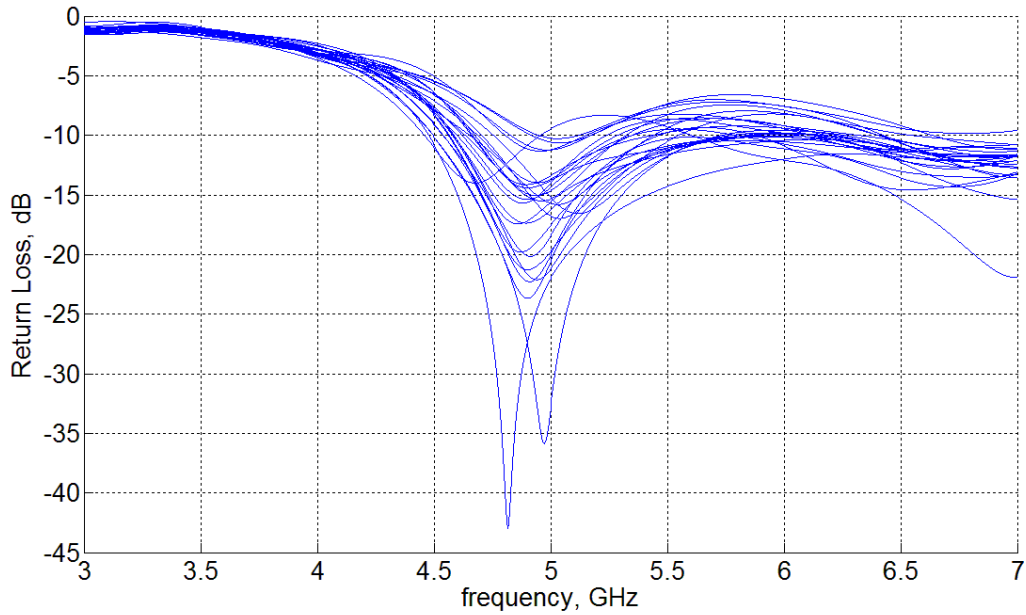


Figure 7.4: Simulated return loss for 32 element golden angle array, CST

7.4 Model Construction

The element is constructed to be soldered onto a supporting bracket holding the SMA connector which it can then be screwed onto a ground plane. Figure 7.5 shows the design structure, where the brackets provide support for the element and the soldering insures the short circuiting of the dipole arms while SMA feed can be soldered onto the balun feed from the opposite side. The elements are then screwed onto the ground plane in holes in the appropriate positions to achieve the required distribution. This is shown in figure 7.6.

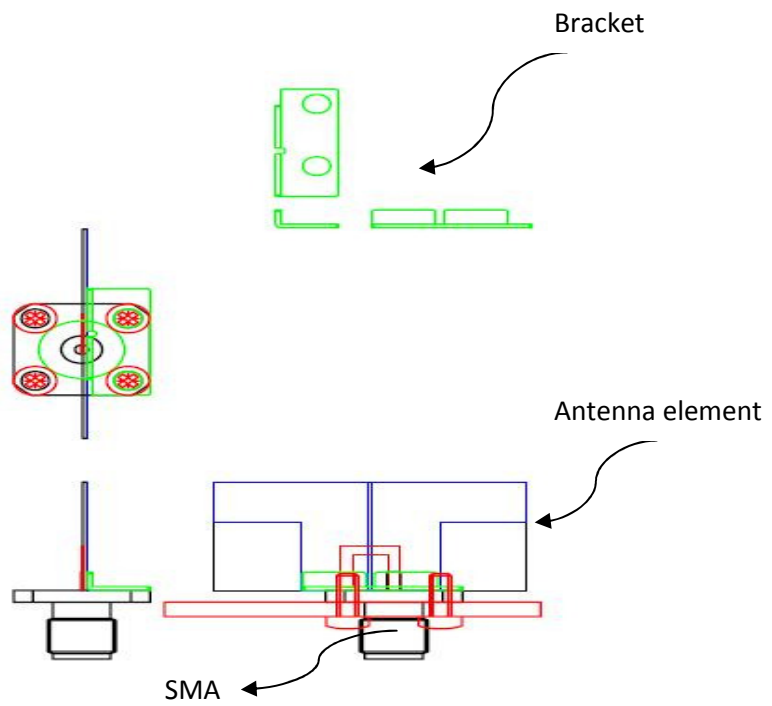


Figure 7.5: Dipole element mechanical structure

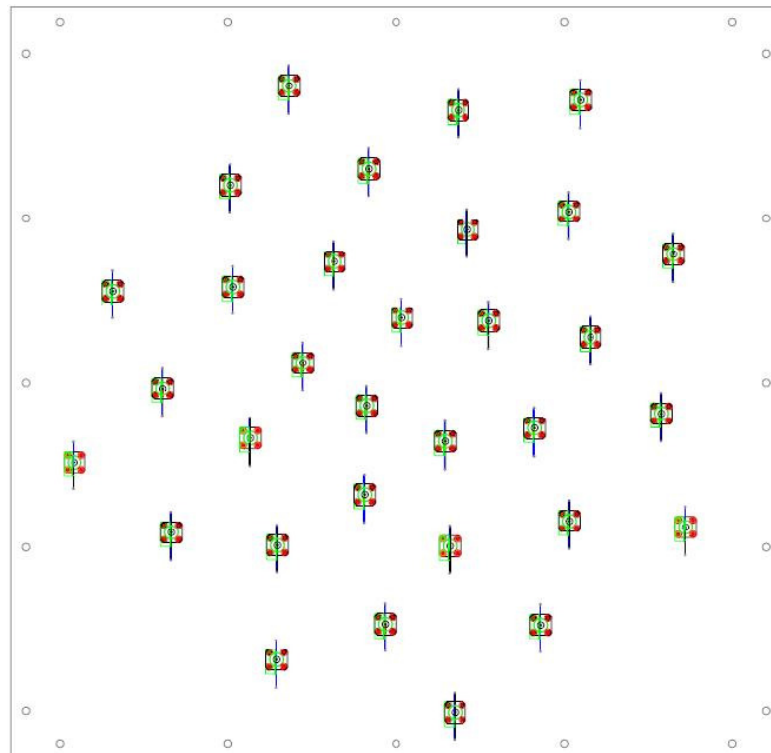


Figure 7.6: Elements on ground plane

A wooden backing structure, figure 7.7 is designed to support the ground plane and the feeding network. The feeding network consists of four 8 to 1 power splitter and a single 4 to 1 power splitters connected with semi-rigid phase matched cables.

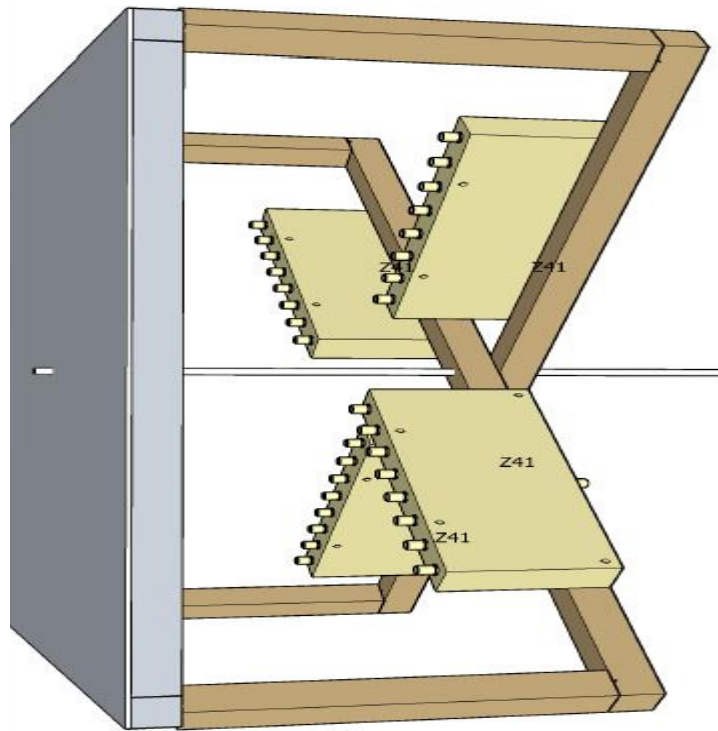


Figure 7.7: Array mechanical support structure

The cables are phased matched within a maximum of ± 3 degrees at 5 GHz with the power splitters having maximum frequency of 7.7 GHz.

7.5 Measurements

Initially, a single element is connected for return loss measurement. The comparison between the simulated and measured return loss has good agreement as shown in figure 7.8.

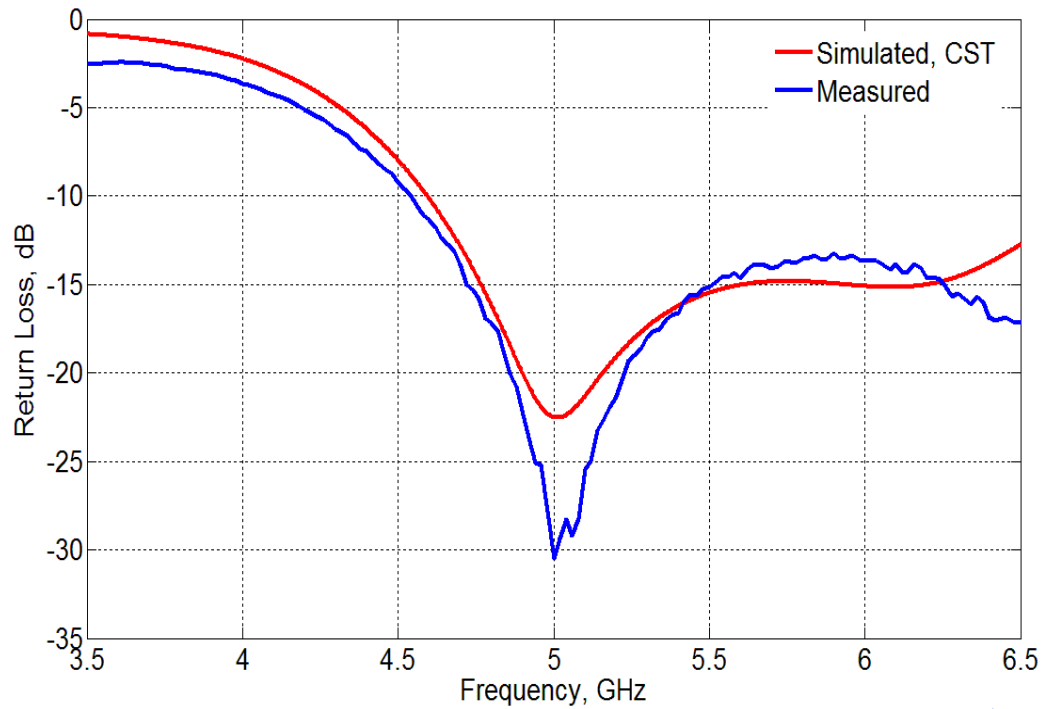


Figure 7.8: Simulated Vs measured return loss

The element is then fitted on a small ground plane and placed in the anechoic chamber for the H and E plane co-polar radiation pattern measurements in figure 7.9 and 7.10 respectively. The comparison shows a good agreement between simulation and measurement. The remaining elements were also measured for return loss and radiation patterns before being all fitted on the main ground plane.

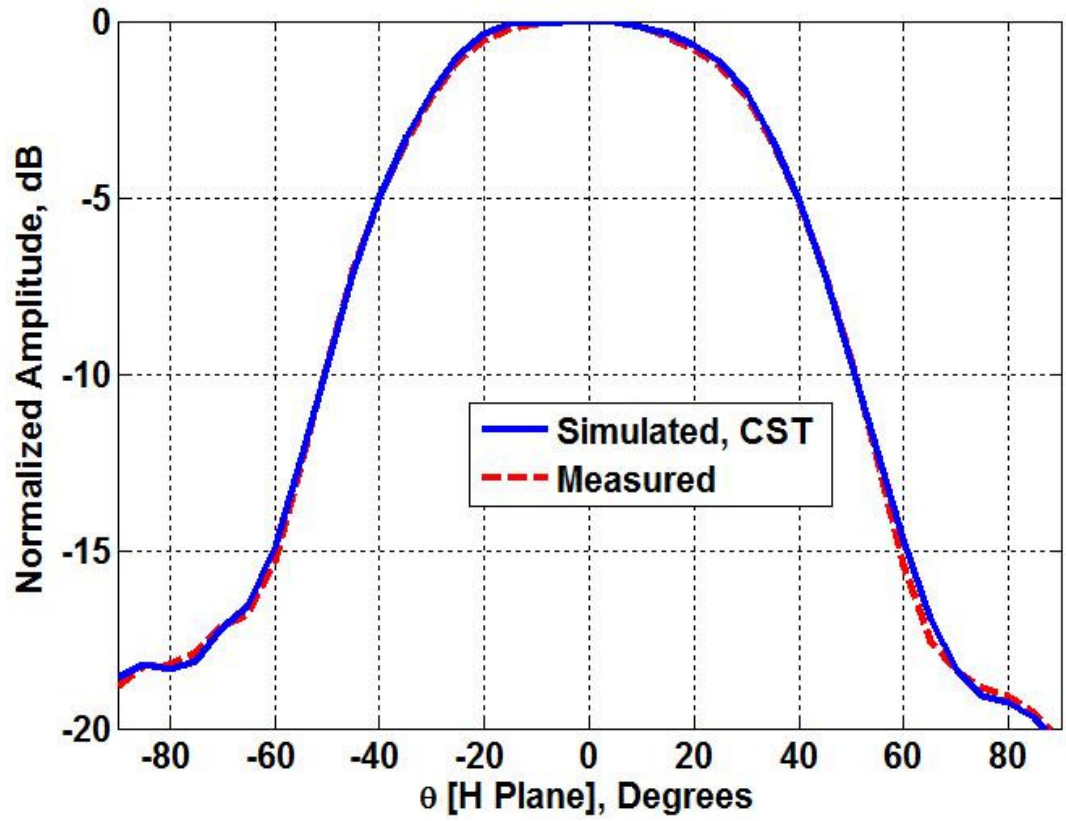


Figure 7.9: Simulated Vs measured H plane element Co-polar radiation pattern

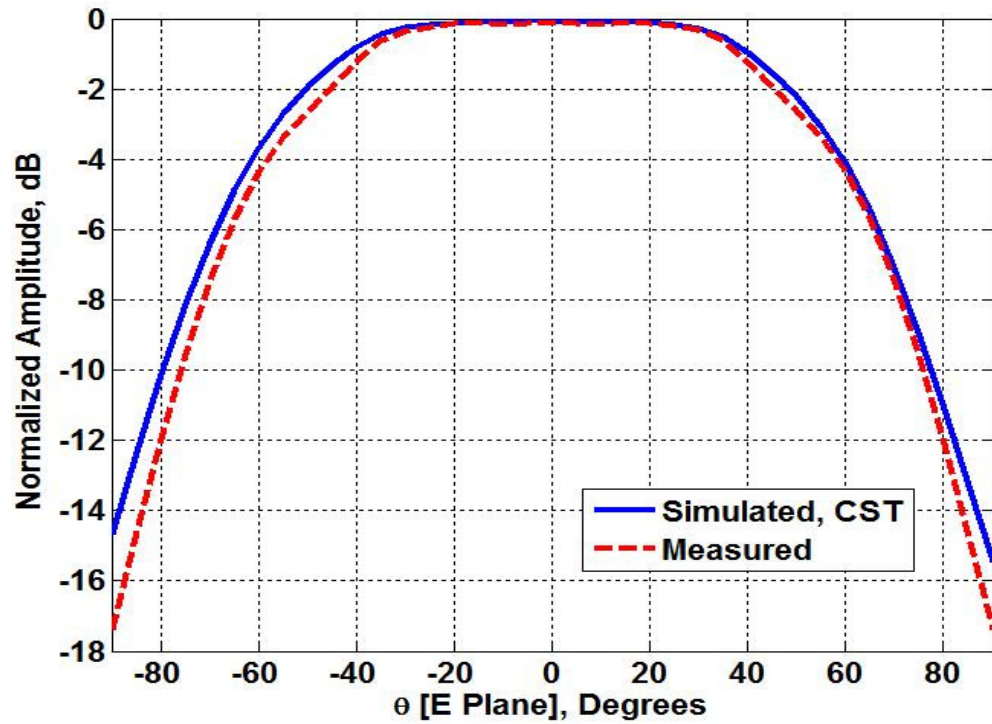


Figure 7.10: Simulated Vs measured E plane element Co-polar radiation pattern

The phase matched cable are then connected through the power splitters and to each element feed point. Although measured cables showed a ± 3 degrees variation in phase, the bending required for connections might increase the phase variations. The power splitters might also introduce an extra phase error. Therefore, the phase errors are measured between the array input and the 32 outputs of the feeding network. The measured phase errors have a maximum amplitude variation of 8% and a maximum phase variation of ± 4 degrees due to errors introduced by different cables and splitters.

The array is then mounted in the anechoic chamber in figure 7.11 for H and E plane co-polar radiation pattern measurements.

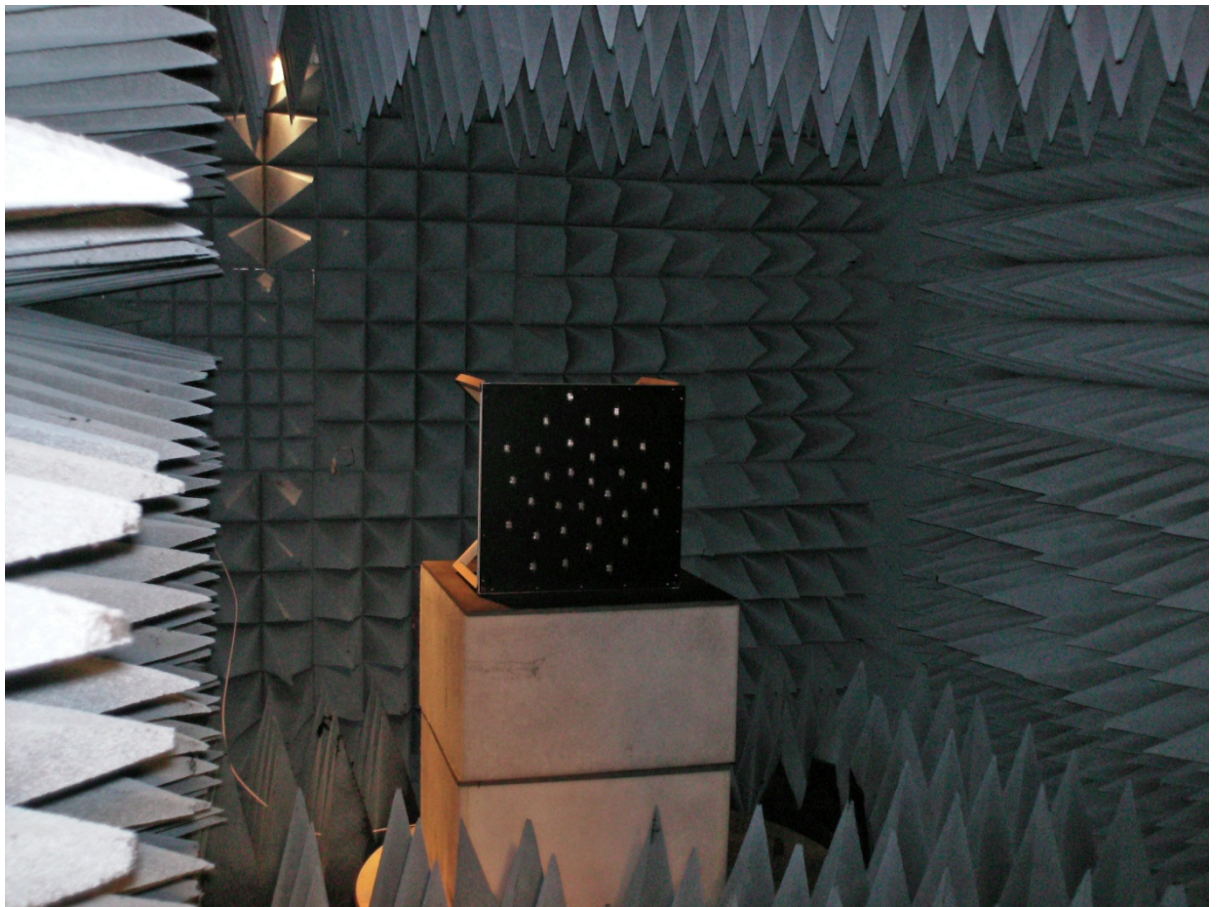


Figure 7.11: connected array in the anechoic chamber

Unfortunately, due to the extra size of the support structure the maximum measuring range was reduced to 4.5 meters which is slightly less than the minimum distance required for the far field of the aperture. The measured co-polar patterns are compared with simulations for both the H plane and the E plane shown in figures 7.12 and 7.13 respectively. Over most angular space, the measurements for both planes show a reasonable agreement with the simulation from CST except for side lobes near the main beam where a maximum error of 2dB is observed in the co-polar plane. The results are also compatible with the simulated results for the exponentially tapered golden ratio spiral discussed in section 4.3.1.

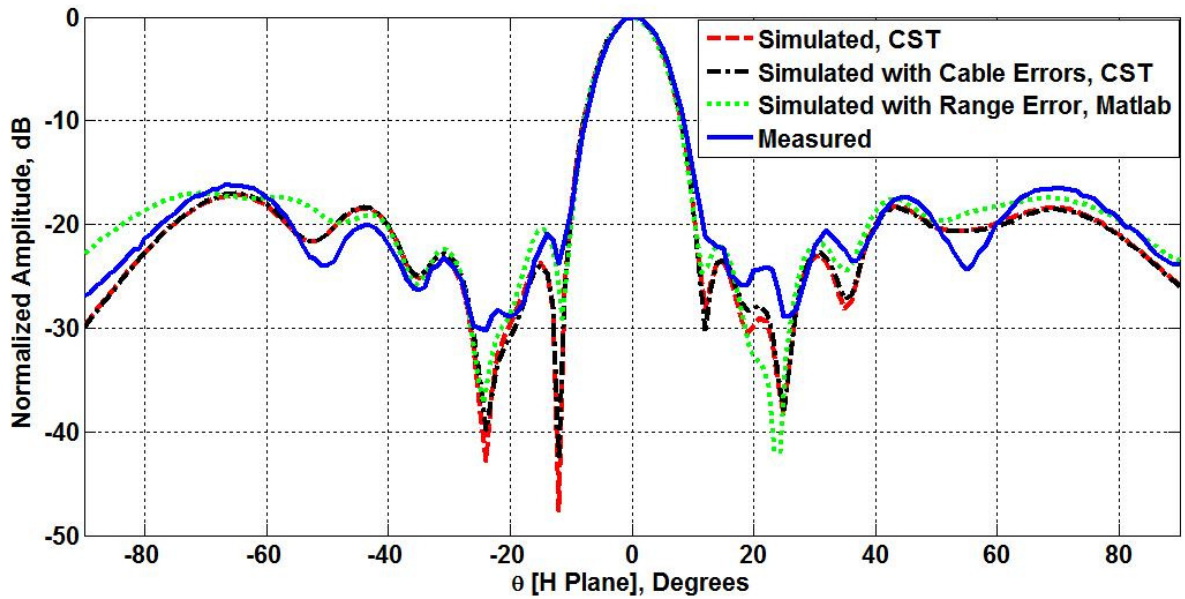


Figure 7.12: Simulated Vs measured H plane array Co-polar radiation patterns

The majority of the error between the simulated and measured patterns is due to the measurement range being slightly shorter than the minimum distance required for far field. In order to verify this, the array radiation pattern is simulated in Matlab with measured element pattern and at the array measurement range of 4.5

meters. The simulated pattern is included in the comparison where an improved agreement is observed. Other errors might include small variation in individual antenna elements due to soldering, in addition to other mechanical imperfections.

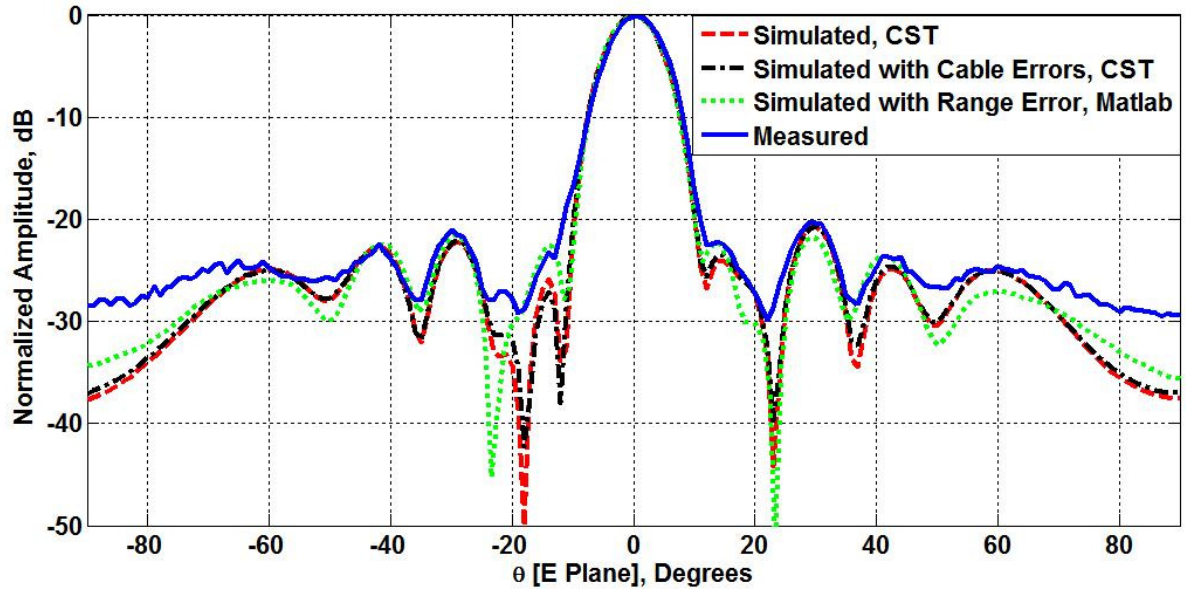


Figure 7.13: Simulated Vs measured array E Plane Co-polar radiation patterns

7.6 Chapter Summary

This chapter illustrates the design and radiation pattern measurement of a 32 element tapered spiral array. The design is implemented using a printed dipole antenna as the array element. The measurements show a reasonable agreement with the simulation where a low side lobe pattern has been achieved by the optimized distribution where the measurements show fair agreement with the simulations. The design demonstrates the advantage of the tapered spiral array geometry on the array system performance.

Chapter 8: On Large Scale Broadband Antenna Array Optimization

8.1 Introduction

From chapter 1, the main figure of merit for optimizing large scale broadband arrays for radio astronomy and other imaging applications, is the overall system sensitivity S , restated here:

$$S = \frac{\lambda^2 \eta_{total} D}{4\pi(\eta_{total} T_A + (1 - \eta_{total}) T_{amb} + T_{LNA})} \dots \dots \dots (8.1)$$

The aim is to meet the minimum sensitivity requirement over the band with the minimum complexity i.e. the minimum number of antenna elements, which requires optimizing the array directivity, sidelobes and efficiency over the band. The optimization can start initially by identifying the noise sources due to the environment and subsequently defining a minimum required directivity and sidelobe performance over the band. A reasonable aperture size and number of elements can then be selected where the element distribution is optimized to closely resemble the required directivity and side lobe profile over a similar

bandwidth. The aperture size and subsequently number of elements can then be scaled to meet the minimum requirement over the required band. The optimization process must keep in mind the minimum separation required by the antenna element in addition to its scan loss. The array total efficiency which depends on the antenna element as well as the resultant geometry must also be considered in the optimization process.

The above is demonstrated in the next two sections for an optimized Square Kilometre Array low frequency aperture array station configuration.

8.2 Square Kilometre Array low frequency aperture array SKA-AA_{low}.

The square kilometre array (SKA) is expected to be the most advanced multiband radio telescope ever built [1]. The specifications of the SKA have been evolving over the years [55]. One part of the SKA is the low frequency aperture array proposed to operate between 70-450 MHz [56]

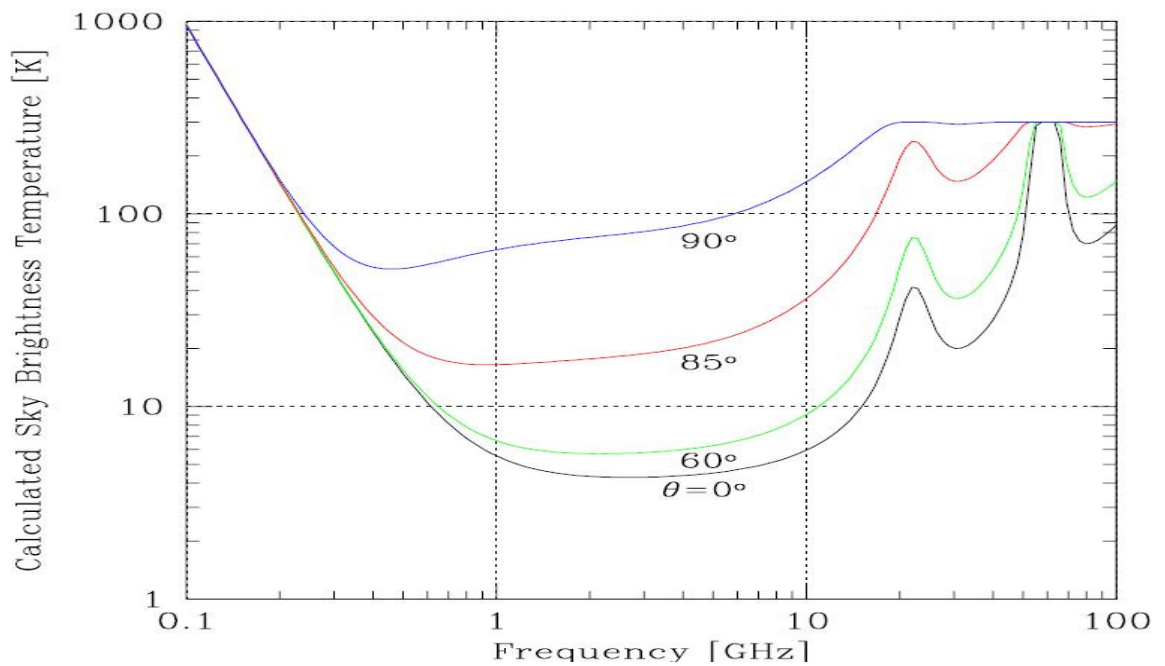


Figure 8.1: Brightness temperature profile for different scan angles [3]

From [55], provided a suitable low noise receiver is used, most of the antenna noise temperature is due to contribution of the sky brightness shown here in figure 8.1 where it becomes noticeably hotter below 1 GHz. Such a hot sky would demand a larger effective area in order to meet the minimum sensitivity of $4000 \text{ m}^2/\text{K}$ from the 250 stations [57].

Due to the high sky brightness temperature at the lowest frequency, an aperture distribution which achieves the maximum possible directivity at the lowest frequency might be an obvious choice. However, the directivity of such an aperture drops dramatically at higher frequencies as shown in chapter 4.2.1 for a large minimum separation random array. This might reduce the sensitivity below the minimum requirements at those frequencies which can only be retained by increasing the number of elements and the aperture size increasing the cost of the overall system. Therefore, an aperture distribution with a relatively high directivity at the lowest frequency and smoother directivity performance for higher frequencies, close to the sky temperature profile, is a more optimum choice. This can be best achieved by the random and the tapered spiral distributions discussed in chapter 5. The directivity performance and frequency band of the two distributions are scaled to the required minimum sensitivity assuming in total 250 aperture arrays. The total efficiency simulated in chapter 5 for each distribution has also been included in the calculation. The resultant sensitivities for the two distributions are shown in figure 8.2 with their required number of elements and the corresponding aperture diameters D_{ap} for each of the 250 stations. Inspection of figure 8.2 shows that the tapered spiral achieves a much flatter sensitivity response which allows the number of elements to be reduced. This results in 11100 elements per array. However, due to the inherent lower directivity of the

random array, 13450 elements are required to meet the minimum sensitivity at the lowest frequency. This also leads to the random array being overdesigned at higher frequencies. The result shows the advantage of the tapered spiral in meeting the minimum sensitivity over the band with fewer elements and subsequently aperture diameter. This shows how the element distribution can be utilized to reduce the complexity of the overall system and prevent over designing the array.

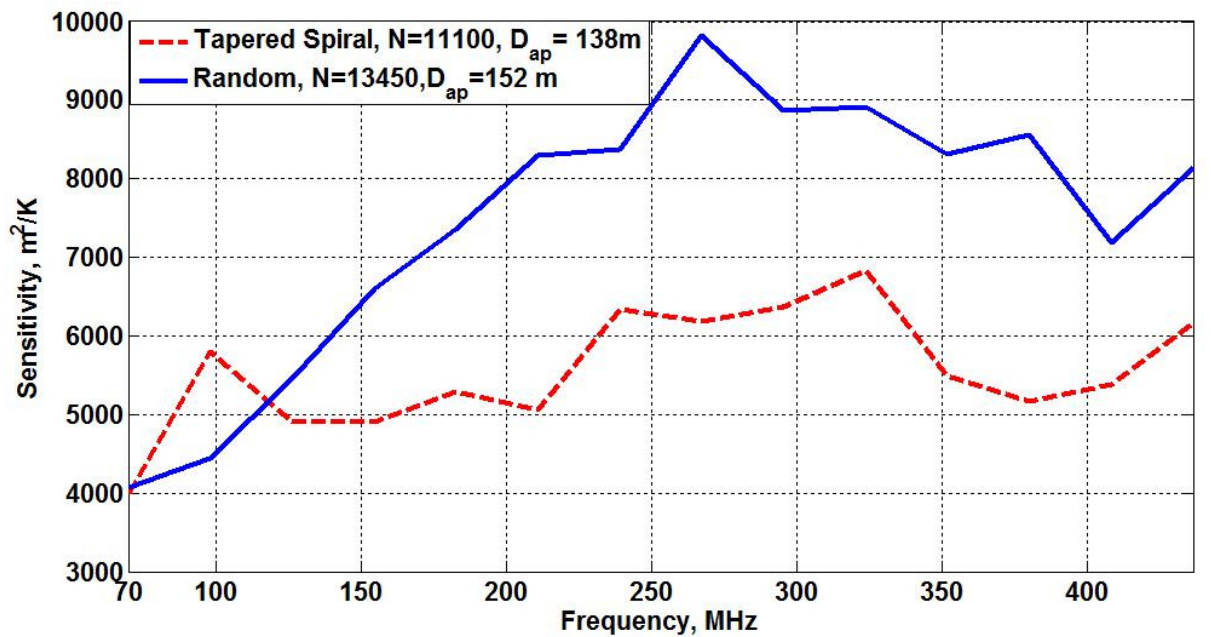


Figure 8.2: Overall SKA sensitivity for 250 stations of tapered spiral and random array configurations, showing the number of elements per station

8.3 Antenna Array Noise Temperature

The previous section considers a constant brightness temperature over angular space according to the model presented in [3]. While this is valid to first order, the sky is often non-uniform over angular space. Subsequently, the total antenna noise temperature becomes complex as the brightness profile is much more

angularly dependant, so that the noise temperature at any one frequency is more heavily dependent on the overall radiation pattern. This can be understood through equation 1.4 which is restated here:

$$T_A = \frac{\iint |F(\theta, \phi)|^2 \cdot T_{sky}(\theta, \phi) \cdot \sin\theta \cdot d\theta \cdot d\phi}{\iint |F(\theta, \phi)|^2 \cdot \sin\theta \cdot d\theta \cdot d\phi} \dots \dots \dots (8.2)$$

The above formula shows the effect of an angular dependent sky temperature on the antenna array noise temperature due to its radiation pattern. In order to illustrate the effect, the Haslam 408 MHz All sky survey data [58] is used for an observation scenario with the radiation patterns obtained from the random and the tapered spiral array distributions of 1000 elements. The Haslam data is a full sky temperature survey at 408 MHz. The observation is carried out by keeping main beam at boresight while the sky is being passed over the array over 24 hours. The antenna noise temperature is then calculated from equation 8.2 ensuring a relatively cold sky at the position of the main beam in order to demonstrate the impact of side lobe level on the antenna noise temperature.

The antenna noise temperature is calculated by substituting the radiation patterns of the two random and tapered spiral arrays in equation 8.2 for each observation. The resultant antenna temperature for the random and the tapered spiral array distribution is shown in figure 8.4. The result shows the advantage of low sidelobes achieved by the tapered spiral in reducing the antenna noise temperature over the band. The computation does not include any other losses and aims to demonstrate to advantage of lower side lobe level in reducing the overall antenna noise temperature.

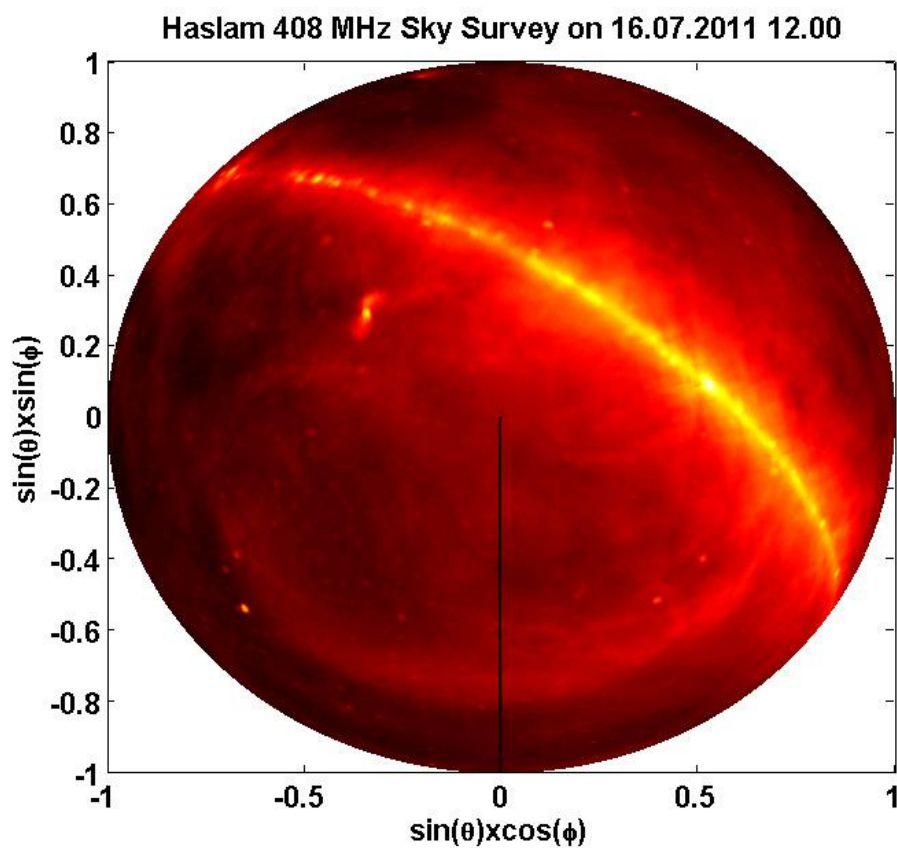


Figure 8.3 sky brightness at 408 MHz [58]

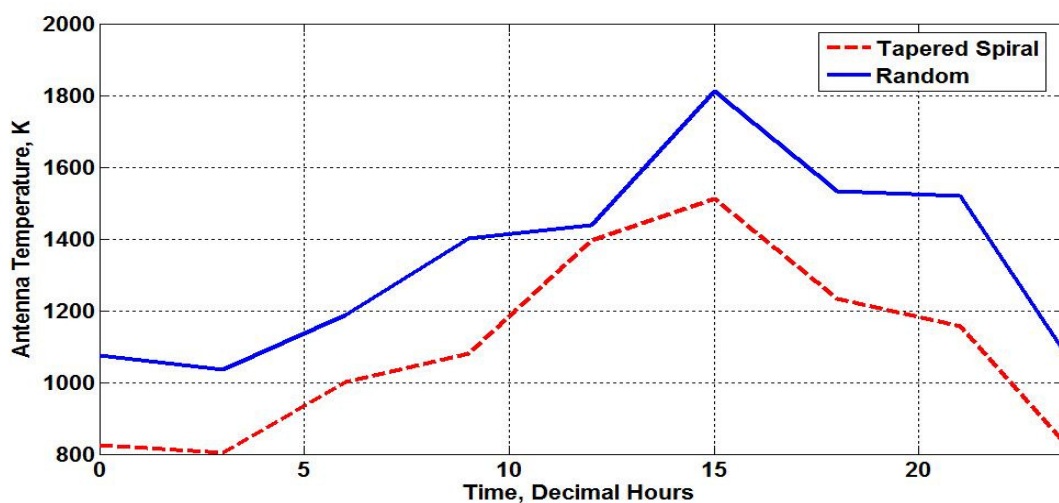


Figure 8.4 Antenna Array Temperature for Tapered Spiral and Random arrays for 24 hour observation at 408 MHz.

8.4 Chapter Summary

This chapter illustrates the large scale broadband optimization technique through a design example for the SKA low frequency aperture array. The result show the advantages of the antenna element distribution in reducing the system complexity by reducing the number of elements while maintaining the minimum requirement. The result show a potential reduction of 2350 elements per station or 587500 elements for the overall SKA by using the more effective tapered spiral distribution. It is worth noting that a square periodic array with half wavelength separation at the highest frequency of 450 MHz, would require a minimum of 140000 elements to meet the low frequency sensitivity requirements while the tapered spiral geometry can meet this minimum requirement with 11100 elements.

The advantage of low side lobes (provided by the distribution) of the tapered spiral array compared to a random array distribution, in reducing the noise temperature is also demonstrated using the Haslam 408 MHz sky survey.

Chapter 9 : Conclusion and Future Work

9.1 Conclusion

This thesis considered the design and optimization of large scale broadband antenna array systems. The research examines the advantages and limitation of the element distribution and its implications on the performance of other system parts. The study also illustrates a flexible optimization process where the array performance can be widely influenced using relatively simple techniques which require no iteration or search algorithms. The study then demonstrates how these techniques can be used to reduce the complexity and enhance the performance. This is achieved through a self built antenna array simulator and verified through full wave simulation in (CST microwave studio) in addition to array radiation pattern measurement of an experimental model.

The choice of optimized geometry can vary significantly depending on the application. However, from this study, three main design categories can be identified:

1. Dense arrays

A dense array with element separations less than one wavelength at the highest frequency in the band (ignoring any scan requirements) is well known and a common approach to designing antenna arrays. For broadband antenna array

applications, this leads to a very small element spacing in terms of wavelength at the lowest frequency. These types of well sampled arrays have the potential to achieve a high directivity particularly at the highest frequency in the band. Moreover, the well sampling insures low side lobe level over the entire band. Therefore, a dense array is an attractive option for applications where low side lobes are essential and/or when higher noise sources exist at high frequencies. The favourite geometries for this type of array are equally spaced square or triangular geometries, section 3.2. These periodic geometries allow for infinite array optimization design which can take into account the effect of mutual coupling which dominate the array environment due to the close separations between antenna elements. The array low frequency bandwidth is limited by the minimum separation which limits the maximum allowed physical element size and hence its low frequency bandwidth. On the other hand, the array high frequency bandwidth is limited by the formation of grating lobes taking into account the maximum scan angle requirement as shown in equation (6.4). However, the main disadvantage of such geometries is the large number of elements required, which leads to increased complexity and poor cost efficiency, particularly for larger bandwidths, where many elements become redundant at the low frequency due to oversampling.

2. Semi-sparse arrays

A semi-sparse array is defined here as an array where the minimum element separation is less than one wavelength at the lowest frequency of the band. This makes the element separations considerably larger than half wavelength at the highest frequency, depending on the bandwidth required. The slightly dense array can provide high and smooth directivity response at these making them suitable

for application if higher noise sources are present. For this type of arrays, an aperiodic geometry is required to avoid any grating lobes at higher frequencies due to the under-sampling. The under-sampling at higher frequencies causes high side lobes in the radiation pattern which can reduce the directivity dramatically. Nonetheless, the element distribution can be manipulated to reduce the effect of the under-sampling and provide a smoother directivity and side lobe performance over the band. Examples of these geometries are random, and tapered spiral array discusses in sections 3.2 and 3.3 respectively. The main advantage of a semi-sparse array is their potential in providing high directivity at low frequencies, from a relatively small number of elements, while maintaining a reasonable performance in terms of directivity and sidelobes at higher frequencies particularly with tapered geometries with relatively denser centre. In addition, the tapered geometries can provide a potential for a more effective beamforming than distributions with wider separation due to the better sampling. Due to the slightly dense distributions at low frequencies, the mutual coupling effect can be significant and cause a change in the impedance matching towards the centre of the array, reducing the overall array efficiency. This is reduced still further for the tapered geometries as seen in sections 5.2 and 5.2. In some applications, a low efficiency can be accepted, if for example, the antenna noise temperature is considerably larger than the ambient temperature as shown in section 8.2. The low frequency bandwidth for this array is limited by the mutual coupling effect and the maximum element physical size (which also constraints the minimum element separation), where the high frequency bandwidth is limited by the element high frequency bandwidth and the formation of much higher side lobe levels due to the severe under-sampling.

3. Sparse arrays

A sparse array is an array where the minimum element separation is larger than one wavelength at the lowest frequency. The same aperiodic geometries can be designed to have that minimum separation. This type of geometry design insures a low mutual coupling effect, which can provide more flexible element design. However, for aperiodic arrays, the directivity does not exceed $N \times D$ despite the antenna element distribution. Nonetheless, the tapered geometries can provide an advantage in terms of lower side lobes over the band.

9.2 Future Work

1. Array Geometry: The geometry study presented in this thesis illustrates the ability to achieve different broadband array performance tradeoffs by using simple optimization techniques. When a particular geometry is reached, further optimization might be possible by using a suitable search algorithm as presented in the literature, in order to further reduce the number of elements without infringing the minimum requirements.
2. Broadband Antenna Element: This thesis considered a tapered slot type broadband antenna as the array element. The geometry performance analysis with several different types of antennas including compact size antennas, would give a greater insight as to the potential difficulties mutual coupling causes. The use of say, two types of antennas interleaved, particularly in the tapered array geometries, may have benefits such as high frequency (and therefore smaller) antenna to be deployed in the more

dense centre of the array, and low band antenna to be positioned in the more sparse region of the array.

3. Electromagnetic modelling: This thesis relied on full wave simulation with using CST microwave studio to model the studied arrays. The Finite Integration Technique (FIT) implemented in CST microwave studio requires large computational resources putting a limitation on the maximum possible array size. It is useful to carry out the modelling with a more efficient software tool. The software might implement the fast Method of Moment MoM technique presented in [65]. The technique utilizes macro basis functions for fast computation of non-uniform arrays.
4. Beamforming: various beamforming techniques have been implemented in this thesis. This included mutual coupling compensation where voltage weights were applied to correct for the mutual coupling effect on the radiation pattern. This technique showed limited performance. Other methods such as the one presented in [40] where embedded radiation patterns were combined with the mutual coupling matrix to obtain a more optimum array radiation patterns, might provide a better mutual coupling compensation. This technique might also be useful for more optimum scanning and null steering.

PUBLICATIONS

- **Conference papers:**

- 1) "Cost performance optimization of large scale wideband arrays for radio telescope applications" El-makadema, A.; Brown, A.K. Loughborough Antennas and Propagation Conference, LAPC, March 17, 2008 - March 18, 2008
- 2) " Broadband Space tapered Golden Ratio Spiral Phased Arrays" El makadema, Ahmed Brown, A.K. Wide Field Astronomy & Technology Conference, Chateau de Limelette, Belgium, 4-6 November 2009,P 285-288

- **Journals**

- 1) A journal paper entitled " Analyses of phased aperture array geometries for low frequency radio astronomy" has been submitted to the journal of experimental astronomy and is currently awaiting reviewers comments

REFERENCES

- [1] www.skatelescope.org
- [2] Schilizzi R. T. , P. Alexander, J. M. Cordes, P. E. Dewdney, R. D. Ekers, A. J. Faulkner, B. M. Gaensler, P. J. Hall, J. L. Jonas, K. I. Kellermann, *Preliminary Specifications for the Square Kilometre Array*, 2007 www.skatelescope.org
- [3] Milligan, T. A. *Modern antenna design*, McGraw-Hill Inc, P 5-7, 1985
- [4] Medellin G.C, *Antenna noise temperature calculation* SKA memo 95, 2007
- [5] Allen B M. Ghavami, *Adaptive array systems: fundamentals and applications*, Wiley, 1st edition ,2005
- [6] Unz, H. *Linear Arrays with arbitrarily distributed elements*, 1952, IEEE Transactions on Antennas and Propagation, vol. 8, issue 2, pp. 222-223
- [7] Harrington, R., *Sidelobe reduction by non-uniform element spacing*, 1960 IEEE Transactions on Antennas and Propagation, vol. 9, issue 2, pp. 187-192
- [8] King, D., R. Packard, and R. Thomas, *Unequally-spaced, broad-band antenna arrays*. Transactions on Antennas and Propagation, IRE 1960. 8(4): p. 380-384.
- [9] Ishimaru, A., *Theory of unequally-spaced arrays*. IRE Transactions on Antennas and Propagation, , 1962. 10(6): p. 691-702.

-
- [10] Skolnik, M., G. Nemhauser, and J. Sherman, III, *Dynamic programming applied to unequally spaced arrays*. IEEE Transactions on Antennas and Propagation, 1964. 12(1): p. 35-43.
- [11] Lo, Y., *A mathematical theory of antenna arrays with randomly spaced elements*. IEEE Transactions on Antennas and Propagation, , 1964. 12(3): p. 257-268.
- [12] Skolnik, M., J. Sherman, III, and F. Ogg, Jr., *Statistically designed density-tapered arrays*. , IEEE Transactions on Antennas and Propagation, 1964. 12(4): p. 408-417.
- [13] Lo, Y. and S. Lee, *A study of space-tapered arrays*. IEEE Transactions on Antennas and Propagation,, 1966. 14(1): p. 22-30.
- [14] Steinberg, B., *Comparison between the peak sidelobe of the random array and algorithmically designed aperiodic arrays*. IEEE Transactions on Antennas and Propagation, 1973. 21(3): p. 366-370.
- [15] O'Neill, D.J. *Element placement in thinned arrays using genetic algorithms*, Oceans Engineering for Today's Technology and Tomorrow's Preservation, Proceedings. 1994.
- [16] Haupt, R.L., *Thinned arrays using genetic algorithms*, IEEE Transactions on Antennas and Propagation, 1994. 42(7): p. 993-999.
- [17] Leeper, D.G., *Isophoric arrays-massively thinned phased arrays with well-controlled sidelobes.*, IEEE Transactions on Antennas and Propagation, 1999. 47(12): p. 1825-1835.

-
- [18] Werner, D.H., R.L. Haupt, and P.L. Werner, *Fractal antenna engineering: the theory and design of fractal antenna arrays*. Antennas and Propagation Magazine, IEEE, 1999. 41(5): p. 37-58.
- [19] Petko, J.S. and D.H. Werner, *the Pareto Optimization of Ultrawideband Polyfractal Arrays*, IEEE Transactions on Antennas and Propagation on, 2008. 56(1): p. 97-107.
- [20] Boeringer, D.W., *Phased array including a logarithmic spiral lattice of uniformly spaced radiating and receiving elements*, U.S. Patent No. 6433745 B1, Silver Spring, MD, US, 13 Apr. 2002.
- [21] Maria Carolina Vigan, Giovanni Toso, Gerard Caille, Cyril Mangenot, Ioan E. Lager, *Sunflower Array Antenna with Adjustable Density Taper*, International Journal of Antennas and Propagation 2009Article ID 624035, 10 pages
- [22] Haupt, R.L., *Optimized Element Spacing for Low Sidelobe Concentric Ring Arrays*. IEEE Transactions on Antennas and Propagation on, 2008. **56**(1): p. 266-268.
- [23] Razavi A. and Forooraghi, K. *Thinned Array Using Pattern Search algorithms* Progress In Electromagnetics Research, PIER 78, 61–71, 2008
- [24] Spence, T.G. and Werner D.H., *Design of Broadband Planar Arrays Based on the Optimization of Aperiodic Tilings*, IEEE Transactions on Antennas and Propagation on, 2008. 56(1): p. 76-86.
- [25] Braun Robert, Cappellen Wim van, *Aperture Arrays for the SKA: Dense or Sparse?* SKA memo 87, 2003

-
- [26] Rumsey, V. H. *Frequency Independent Antennas*, IRE National Convention Record, Pt. 1, March 1957
- [27] Allen, B. M. Dohler, E. Okon, W. Malik, A. Brown, D. Edwards, *Ultra-Wideband: Antennas and Propagation for Communications, Radar and Imaging*, Editor and Contributor, Wiley & Sons, October 2006.
- [28] Elliott, R.S. *Antenna Theory and Design*, Prentice-Hall, 1981
- [29] Pozar, David M. D. Schaubert, *Microstrip antennas: the analysis and design of microstrip antennas and arrays*, IEEE Press, New York, 1996
- [30] Kun-Chou, L. and C. Tah-Hsiung, *A circuit model for mutual coupling analysis of a finite antenna array*, IEEE Transactions on Electromagnetic Compatibility, 1996. 38(3): p. 483-489.
- [31] Davidson, D. B. *Computational Electromagnetics for RF and Microwave Engineering*, Cambridge University Press, Cambridge, 2005.
- [32] Hansen, R. C *phased array antennas*, Academic Press, New York, 1964
- [33] Hansen, R. C *Microwave scanning antennas*, Volume 1, Academic Press, New York, 1964
- [34] Hansen, R. C *Microwave scanning antennas*, Volume 2, Academic Press, New York, 1966
- [35] Hansen, R. C *Microwave scanning antennas*, Volume 3, Academic Press, New York, 1966

-
- [36] Takubo, S., Y. Tajima, and Y. Yamada. *Radiation pattern synthesis of an unequally spaced array antenna*, Antennas and Propagation Society International Symposium, 2000. IEEE. 2000.
- [37] Han, R.-c., et al. *Pattern Synthesis of Sparse Phased Array Antenna Using Genetic Algorithms*, Environmental Electromagnetics, The 2006 4th Asia-Pacific Conference on, 2006.
- [38] Williams, M.I.Y., T.D. Abhayapala, and R.A. Kennedy. *Generalized Broadband Beamforming Using a Modal Decomposition*, IEEE International Conference on Speech and Signal Processing, 2006.
- [39] Gallaudet, T.C. and C.P. de Moustier, *On optimal shading for arrays of irregularly-spaced or noncoplanar elements*, IEEE Journal of Oceanic Engineering, 2000. 25(4): p. 553-567.
- [40] Goossens, R. and H. Rogier, *Optimal beam forming in the presence of mutual coupling*, Communications and Vehicular Technology, 2006.
- [41] Jwo-Shiun, S. and C. Guan-Yu, *The tapered slot antenna*, Microwave and Millimetre Wave Technology, 2004, ICMMT 4th International Conference on, Proceedings, 2004.
- [42] Hon Tat Hui, *Decoupling Methods for the Mutual Coupling Effect in Antenna Arrays: A Review*, Bentham Science Publishers, Volume 1, Number 2, June 2007, pp. 187-193(7).
- [43] Huapt, Randy L *Antenna Arrays: A Computational Approach*, Wiley & sons, 2010

-
- [44] Jian-Ming Jin, Douglas J. Riley, *Finite element analysis of antennas and arrays*, Wiley & sons, 2009
- [45] Bakshi, U.A., Bakshi, A.V., *Antennas and Wave Propagation*, Technical publications, 2009, P5-2
- [46] Oppermann, I. Linatti, J., *UWB theory and applications*, Wiley & Sons, 2004, p135
- [47] Thomas A. Milligan, *Modern antenna design*, Wiley-IEEE Press; 2 edition, 2005
- [48] Pozar, D.M., *The active element pattern*. Antennas and Propagation, IEEE Transactions on, 1994, p. 1176-1178.
- [49] Amitay, N., Galindo, V. C.P. Wu, *Theory and Analysis of Phased Array Antennas*, Wiley-Inter science, 1972
- [50] <http://mathworld.wolfram.com/Spiral.html>
- [51] Livio, M., *The golden ratio: the story of phi, the world's most astonishing number*. Broadway Books, 2003
- [52] Pozar, D.M., *Microwave Engineering, 3Rd Ed.*: Wiley India Pvt. Ltd 2009
- [53] Li, R.L., et al, *A broadband printed dipole and a printed array for base station applications*, Antennas and Propagation Society International Symposium, AP-S IEEE, 2008.
- [54] <http://www.rogerscorp.com/>
- [55] Lo, Y. T. S. Lee, W. *Antenna Handbook: Antenna theory*, Springer, 1993

-
- [56] Rosie Bolton, Andrew Faulkner, Paul Alexander, Steve Torchinsky, Arnold van Ardenne, Peter Wilkinson, Marco de Vos, Laurens Bakker, Simon Garrington, Georgina Harris, Tim Ikin, Mike Jones, Dion Kant, Danielle Kettle, Roshene McCool, Parbhu Patel and John Romein⁴, *SKADS Benchmark Scenario Design and Costing – 2 (The SKA Phase 2 AA Scenario)*, University of Cambridge University of Manchester, Obs. de Paris, ASTRON, University of Oxford, 2007
- [57] D. L. Jones , *SKA Memo 45 SKA Science Requirements: Version 2*, 2004
- [58] Haslam, C.G.T., Klein, U., Salter, C.J., et al.: *A 408 MHz all-sky continuum survey. I – Observations at southern declinations and for the North Polar region*. Astronomy & Astrophysics 100(2), 209-219 (1981)
- [59] M. T, MA, *Theory and applications of antenna arrays*, Wiley and Sons, 1974
- [60] Elliot, R. S., *Antenna theory and design*, Wiley and Sons, 1981
- [61] Rudge, A.W *Handbook of antenna design*, Volume 2: Peter Peregrinus, 1983
- [62] Brookner, E., *Practical Phased Array Antenna System*, Artech House, Inc, 1991
- [63] Lamont V. Blake, *Antennas*, Munro Pub Co, 2nd edition, 1991
- [64] Mailloux, Robert J. *Phased Array Antenna Handbook*, Second Edition Artech House, 2005
- [65] Gonzalez-Ovejero, D. and C. Craeye. *Fast computation of macro basis functions interactions in non uniform arrays*. IEEE Antennas and Propagation Society International Symposium, 2008.

-
- [66] Litva, J. Lo, Titus Kwok-Yeung *Digital beamforming in wireless communications*, Artech House, 1996
- [67] Haupt, R.L. *Thinned concentric ring arrays*, Antennas and Propagation Society International Symposium, 2008. AP-S 2008. IEEE. 2008.
- [68] Shiwen, Y., Zaiping N., and Feng, Y. *Mutual coupling compensation in small antenna arrays by the differential evolution algorithm*, Asia-Pacific Conference Proceedings. 2005.

BIBLIOGRAPHYS

- [1] Lee KC. *A simplified model for the mutual coupling effects of adaptive antenna arrays*, J Electromagnetic Waves Application 2004; 17(9): 1261-1268.
- [2] Ioannides P, Balanis CA. *Mutual coupling in adaptive circular arrays*. Proc IEEE Antennas Prop Soc Inter Symposium 2004. USA (2004); 1: 403-406.
- [3] Durrani S, Bialkowski ME. *Effect of mutual coupling on the interference rejection capabilities of linear and circular arrays in CDMA*. IEEE Trans Antennas Prop 2004; 52(4): 1130-1134.
- [4] Lee KC, Chu TH. *Mutual coupling mechanisms within arrays of nonlinear antennas*, IEEE Transactions on Electromagnetic Compatibility 2005; 47(4): 963-970.
- [5] Rogier H, Bonek E. *Analytical spherical-mode-based compensation of mutual coupling in uniform circular arrays for direction-of-arrival estimation*. Inter J Electron Commun 2006; 60(3): 179-189.
- [6] Jordan EC, *Electromagnetic Waves and Radiating Systems*, Prentice-Hall Inc, Englewood Cliffs, N. J. 1968.
- [7] Tai CT, *A study of the EMF method*, Journal of Applied Physics 1949; 717-23.
- [8] Harrington, *RF Field Computation by Moment Methods*. New York: IEEE Press 1993.

-
- [9] Bladel JV, *on the equivalent circuit of a receiving antenna*. IEEE on Antennas Propagation Magazine 2002; 44(1): 164-165.
- [10] Gupta IJ, Ksienski AA, *Effect of mutual coupling on the performance of adaptive arrays*, IEEE Trans on Antennas Propagation 1983; 31(9): 785-791.
- [11] Lo KW, Vu TB, *Simple s-parameter model for receiving antenna array*, Electronic Letters 1988; 24(20): 1264-1266.
- [12] Yeh CC, Leou ML, Ucci DR. *Bearing estimations with mutual coupling present*, IEEE Transactions on Antennas Propagation 1989; 37(10): 1332-1335.
- [13] Lee KC, Chu TH. A circuit model for mutual coupling analysis of a finite antenna array. IEEE Transactions on Electromagnetic Compatibility 1996; 38(8): 483-489.
- [14] Friel EM, Pasala KM, *Effects of mutual coupling on the performance of STAP antenna arrays*, IEEE Trans Aerospace Elect Sys 2000; 36(2): 518- 527.
- [15] Allen OE, Wasyliwskyj W, *Comparison of mutual coupling of blade antennas with predictions based on minimum-scattering antenna theory*, IEEE Trans Electromagnetic Compatibility 2000; 42(4): 326-329.
- [16] Leifer MC, *Mutual coupling compensation accuracy*, IEEE Proceedings on Antennas and Propagation Society International Symposium 2001. USA (2001); 3: 804-807.
- [17] Hui HT, Chan KY, Yung EKN, *Compensating for the mutual coupling effect in a normal-mode helical antenna array for adaptive nulling*, IEEE Trans Vehicular Technol 2003; 52(4): 743-751.

-
- [18] Hui HT. *A practical approach to compensate for the mutual coupling effect of an adaptive dipole array*. IEEE Transactions on Antennas and Propagation 2004; 52(5): 1262-1269.
- [19] Jarske, P. T. Saramaki, S. Mitra, and Y. Neuvo, "On the properties and design of nonuniformly spaced linear arrays," IEEE Trans. Acoust., Speech, Signal Processing, 1988. vol. ASSP-36, pp. 372–380
- [20] Streit, R. L. and Nuttall, A. H., *A general Chebyshev complex function approximation procedure and an application to beamforming*, J. Acoust. Soc. Amer., 1982. vol. 72, no. 1, pp. 181–189.
- [21] Jiao, Y. W. L. Wei, Huang, and H. Wu, *A new low sidelobe pattern synthesis technique for conformal arrays*, IEEE Trans. Antennas Propagat., 1993. vol. 41, no. 6, pp. 824–831.
- [22] Hui HT, Low HP, Zhang TT, Lu YL, *Receiving mutual impedance between two normal mode helical antennas (NMHAs)*, IEEE Antenna Prop Magazine 2006; 48(4): 92-96.
- [23] Zhang TT, Hui HT, Lu YL, *Compensation for the mutual coupling effect in the ESPRIT direction finding algorithm by using a more effective method*, IEEE Trans Antennas and Prop 2005; 53(4): 1552-1555.
- [24] Hui HT, *An effective compensation method for the mutual coupling effect in phased arrays for magnetic resonance imaging*, IEEE Trans Antennas Prop 2005; 53(10): 3576-3583.
- [25] Hui HT, Li BK, Crozier S, *A new decoupling method for quadrature coils in Magnetic resonance imaging*, IEEE Trans Biomed Eng 2006; 53(10): 2114- 2116.
-

-
- [26] McMahon, G. W. B. Hubley, and A. Mohammed, *Design of optimum directional arrays using linear programming techniques*, J. Acoust. Soc. Amer., pt. 2 1972., vol. 51, no. 1, pp. 304–309.
- [27] Ziehm, G., *Optimum directional pattern synthesis of circular arrays*, Radio Electron 1964. Eng., vol. 28, pp. 341–355.
- [28] Wang, H. S. C., *Interference rejection by amplitude shading of sonar transducer arrays*, J. Acoust. Soc. Amer, 1977. vol. 61, no. 5, pp. 1251–1259.
- [29] Dolph, C. L. *A current distribution for broadside arrays which optimizes the relationship between beamwidth and side-lobe level*, in Proc. IRE, vol. 34, June 1946, pp. 335–348.
- [30] Streit, R. L. *Sufficient conditions for the existence of optimum beam patterns for unequally spaced linear arrays with an example*, IEEE Trans. Antennas Propagation 1975. vol. AP-23, pp. 112–115.
- [31] Wilson, G. L. *Computer optimization of transducer array patterns*, J. Acoust. Soc. Amer, 1976. vol. 59, no. 1, pp. 195–203.
- [32] Bucci, O. M. G. Romito G., *Power synthesis of conformal arrays by a generalized projection method*, IEE Proc.-Microw. Antennas Propag, 1995. vol. 142, no. 6, pp. 467–471.
- [33] Lee, S. W. and Lo, Y. T., *on the pattern function of circular arc arrays*, IEEE Trans. Antennas Propagation., 1965. vol. AP-13, pp. 649–650.
- [34] Streit, R. L., *Optimized symmetric discrete line arrays*, IEEE Trans. Antennas Propagation., 1975 vol. AP-23, pp. 860–862.

-
- [35] Lewis, J. T. and Streit, R. L., *Real excitation coefficients suffice for sidelobe control in a linear array*, IEEE Trans. Antennas and Propagat., 1982. vol. AP-30, pp. 1262–1263.
- [36] Goto, N. and Tsunodo, Y., *Sidelobe reduction of circular arrays with a constant excitation amplitude*, IEEE Trans. Antennas Propagation., 1977 vol. AP-25, pp. 896–897.
- [37] Watanabe, F. N. Goto, Nagayama, A. and Yoshida, G., *A pattern synthesis of circular arrays by phase adjustment*, IEEE Trans. Antennas Propagation., 1980. vol. AP-28, pp. 857–863.
- [38] S. Prasad and R. Charan, *On the constrained synthesis of array patterns with applications to circular and arc arrays*, IEEE Trans. Antennas Propagation., 1984. vol. AP-32, pp. 725–730.
- [39] Schuman, H. K. *Conformal array synthesis*, in *Proc. IEEE Antennas and Propagation Soc. Int. Symp. 1994*, Seattle, WA, June 20–24, 1994, pp. 526–529.
- [40] Chakraborty, B. *Studies on a 120 deg. segmented circular array for multibeam multi-frequency bathymetric applications*, J. Sound and Vibration., 1995. vol. 179, no. 1, pp. 1–12.
- [41] de Moustier, C. P. *Signal processing for swath bathymetry and concurrent seafloor acoustic imaging*, Acoustic Signal Processing for Ocean Exploration, NATO ASI Series, J. M. F. Moura and I. M. G. Lourie, Eds. Boston, MA: Kluwer, 1993, pp. 329–354.

-
- [42] Sureau, J. and Keeping, K., *Sidelobe control in cylindrical arrays*, IEEE Trans. Antennas Propagation., 1982.vol. AP-30, pp. 1027–1031.
- [43] Harris, F. J., *On the use of windows for harmonic analysis with the discrete Fourier transform*, Proc. IEEE,. 1978. vol. 66, pp. 51–83.
- [44] Riblet, H. J. *A discussion of Dolph's paper*, Proc. IRE., 1947, vol. 35, pp. 489–492.
- [45] Duhamel, R. H. Optimum pattern for endfire arrays, in Proc. IRE, vol. 40, 1953, pp. 652–659.
- [46] Pritchard, R. L. Optimum directivity patterns for linear point arrays, J. Acoust. Soc. Amer., 1953. vol. 25, no. 5, pp. 879–891.
- [47] Taylor, T. T., *Design of line-source antennas for narrow beamwidth and low side lobes*, IRE Trans. Antennas Propagation., 1955. vol. AP-3, pp. 16–28.
- [48] Baklanov, Y. V., *Chebyshev distribution of currents for a plane array of radiators*, Radio Eng. and Electronic Phys., 1966. vol. 11, pp. 640–642.
- [49] F. Tseng and D. Cheng, *Optimum scannable planar arrays with an invariant sidelobe level*, Proc. IEEE., 1968. vol. 56, pp. 1771–1778.
- [50] Davids, N. Thurston, E. G., and Mueser, R. E., *The design of optimum directional acoustic arrays*, J. Acoust. Soc. Amer., 1952. vol. 24, pp. 50–56.
- [51] Gabriel'yan D. D., and Mishchenko, S. E. *Amplitude-phase synthesis of an acoustic antenna array on a circular cylinder*, Acoustic. Phys., 1995. vol. 41, no. 1, pp. 137–139.

-
- [52] Vaskelainen, L. I., *Iterative least squares synthesis methods for conformal array antennas with optimized polarization and frequency properties*, IEEE Trans. Antennas. Propagat., July 1997. vol. 45, pp. 1179–1185.
- [53] Welkowitz, W., *Directional circular arrays of point sources*, J. Acoust. Soc. Amer., 1955. vol. 28, no. 3, pp. 362–366.
- [54] W. R. Lepage, C. S. Roys, and S. Seely, *Radiation from circular current sheets*, in Proc. IRE, vol. 38, 1950, pp. 1069–1072.
- [55] James, C. M., *Polar patterns of phase-corrected circular arrays*, Proc IEE., 1965. vol. 112, no. 10, pp. 1839–1848.
- [56] McDonald, R. J., and Manning, R., *Motion-compensated beamforming algorithm for a circular transducer array*, U.S. Navy J. Underwater Acoustic., 1997. vol. 47, no. 2, pp. 905–920.
- [57] Tseng, C., and Griffiths, L. J., *A simple algorithm to achieve desired patterns for arbitrary arrays*, IEEE Trans. Signal Processing., 1992. vol. 40, pp. 2737–2746.
- [58] Wang, H. S. C., *Amplitude shading of sonar transducer arrays*, J. Acoust. Soc. Amer., 1975. vol. 57, no. 5, pp. 1076–1084.
- [59] Sullivan, E. J. *Amplitude shading of irregular acoustic arrays*, J. Acoust. Soc. Amer., 1978. vol. 63, no. 6, pp. 1873–1877.
- [60] Werner, D. H., and Kuhirun, W., *The peano-gosper fractal array*, IEEE Trans. Antennas Propag., 2003. vol. 51, no. 8, pp. 2063–2072.

-
- [61] Werner, D. H., and Kuhirun, W., *Fractile arrays: A new class of tiled arrays with fractal boundaries*, IEEE Trans. Antennas Propag., 2004. vol. 52, no. 8, pp. 2008–2018.
- [62] Bogard, J. N., Werner, D. H. and Werner, P. L. *A comparison of the peano gosper fractile array with the regular hexagonal array*, Microwave and. Opt. Technol., 2004. vol. 3, no. 6, pp. 524–526.
- [63] van der Maas, G. L. *A simplified calculation for Dolph–Tchebysheff arrays*, Jour. Appl. Phys., 1954. vol. 25, pp. 121–124.
- [64] Nuttall, A. H., *A two-parameter class of Bessel weightings with controllable sidelobe behavior for linear, planar-circular, and volumetric-spherical arrays; the ideal weighting-patterns pairs*, Naval Underwater Systems Center, Newport, New London, RI, CN, NUSC Technical Report., 1982.6761
- [65] Holm, S., Elgetun, B. and Dahl, G. *Properties of the beam pattern of weight- and layout-optimized sparse arrays*, IEEE Trans. U.F.F.C., 1997. vol. 44, pp. 983–991.
- [66] Lan, J. R. Jeffers, K. and Boucher, S. G., *Optimum unequally-spaced arrays and their amplitude shading*, in Proc. IEEE Ultras. Symp., vol. 2, Seattle, WA, 1995, pp. 965–969.
- [67] Erstad J. O. and Holm, S. *An approach to the design of sparse array systems*, in Proc. IEEE Ultras. Symp., vol. 3, Cannes, France, 1994, pp. 1507–1510.
- [69] Pierro V., Galdi V., Castaldi G., Pinto, I. M., and L. B. Felsen, L. B., *Radiation properties of planar antenna arrays based on certain categories of aperiodic tilings*, IEEE Trans. Antennas Propag., Feb. 2005. vol. 53, no. 2, pp. 635–644.